Ultrafast Molecular Dynamics at Surfaces

Ian Michael Lane
Downing College

Department of Chemistry
University of Cambridge

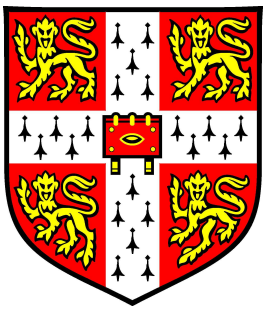

Submitted for the degree of Doctor of Philosophy

September 2006

Preface

This thesis is submitted in conformity with the requirements of the University of Cambridge for the degree of Doctor of Philosophy. The work described in this thesis is the original work of the author and includes nothing which is the outcome of work done in collaboration, unless otherwise stated. No part of this thesis has been, or is being, submitted at this or any other university for a degree or equivalent qualification. This manuscript does not exceed 60,000 words in length, as specified by the Degree Committee for Physics and Chemistry.

Ian M Lane, September 2006

Copyright © I.M. Lane 2006

Acknowledgements

I would like to thank my supervisor Professor Sir David King, who has provided the focus for my studies and always maintained great interest in its development. Particular thanks are due to Dr Heike Arnolds, who has been central to the work undertaken. Her approach and knowledge to both experiment and theory have been irreplaceable and she has always been happy to explain and develop her thoughts with me. I thank her for proof reading this thesis and for her much valued friendship during my time in Cambridge.

I would like to thank the King group for their support and conversation in the tea room, it is much appreciated. This includes the help given by Vannesa Zhang in my first year, who helped introduce me to the laboratory. Thanks go to Dr Zhi-Pan Liu for carrying out DFT calculations, they proved very useful for this work. I would like to acknowledge experimental funding from EPSRC.

I would like to thank my friends for all of the good times shared, and Jo for her patience while writing up. Finally, special thanks go to my family for all of their help and support over the years.

Abstract

The work presented in this thesis aims to increase our understanding of molecular dynamics at metal surfaces, with a focus on probing the time scales of fundamental processes and interactions that can determine reactivity. The technique of pump-probe Sum Frequency Generation (SFG) was used to follow molecular/vibrational surface dynamics on a femtosecond (10^{-15} s) time scale, by probing the intramolecular stretch of adsorbates.

Infrared (IR) pump pulses allow the investigation of vibrational dynamics; a complete mapping of coherent and incoherent vibrational relaxation times for a molecule on a metal surface, CO/Ir{111} are presented. This includes a definitive assignment of adsorbate inhomogeneity and a further step towards bond selective chemistry via vibrational ladder climbing. Included is the first detection of a mid-infrared photon echo from a metallic surface, setting a precedent for the ability to manipulate and rephase polarisation on a sub-picosecond time scale on surfaces.

Ultrafast visible heating pulses allow study of the molecular dynamics of CO, NO and CO+NO on the Ir{111} surface. It is observed that CO responds adiabatically to laser excitation, while NO exhibits non-adiabatic dynamics. This behaviour is driven by transient transfer of hot electrons into the NO $2\pi^*$d antibonding orbital, which over a period of 670 fs drives the NO to bend over and weaken the Ir-NO and N-O bonds. This response is similar in nature to the pathways for both desorption and dissociation. Addition of CO+NO to the surface yields an adsorbate profile significantly different to any observed previously. The time scale of which (~3 ps), represents the interaction between CO and NO, driven by the laser-induced bending of the NO. This interaction is deemed to be the primary step in the reaction to form CO_2.

Publications

[1] I. M. Lane, D. A. King, Z. P. Liu, H. Arnolds. Real-time observation of non-adiabatic surface dynamics: The first picosecond in the dissociation of NO on iridium, *Physical Review Letters*, 97(10): 186105, 2006.

[2] I. M. Lane, D. A. King, H. Arnolds. The determination of an inhomogeneous linewidth for a strongly coupled adsorbate system, *Accepted by Journal of Chemical Physics*, October 2006.

[3] I. M. Lane, D. A. King, Z. P. Liu, H. Arnolds. Ultrafast vibrational dynamics of NO and CO adsorbed on an iridium surface, *Submitted to Journal of Physical Chemistry C*, November 2006.

Contents

Chapter 1

Introduction

1.1 Surfaces

Chemical reactions at the interface between two different phases (heterogeneous) are critically important to many aspects of our daily life. In particular the gas/solid interface is central to many important chemical processes including semiconductor fabrication, fuel cell technology, automobile catalytic converters and the catalytic cracking of petrochemicals.

Typically heterogeneous catalysis occurs at high temperatures and pressures over a supported metal catalyst. This does however make it difficult to study the exact mechanism of the processes involved, leading to a trial and error approach of developing new catalysts. It is thus required to make the process of designing new catalysts more theoretically robust, based upon the acquisition of high quality, quantitative experimental data.

The surface science approach was introduced to study these systems using the central concepts of metal single crystals and Ultra High Vacuum (UHV) conditions. A single crystal allows the preparation of well defined surfaces with known structural features and adsorption sites. UHV prevents contamination of the sur-

face with atmospheric gases and allows for specific quantitative dosing of required adsorbates. At pressures $< 10^{-10}$ mbar, the time to contaminate a surface can be measured in hours, giving the experimentalist time to study a freshly cleaned surface [1].

The main surface science probe used in this thesis is Sum Frequency Generation (SFG), a laser spectroscopy that can be used at UHV, atmospheric or liquid interfaces. This adaptability is a huge positive for the development of SFG, as the surface science approach evolves to bridge the gap between UHV and "real" catalytic conditions under high pressure and temperature. However, the work presented herein does not make any impression on this pressure gap, nor does it even try to. Instead it aims to add a new dimension to the study of reactions at UHV surfaces by measuring the time scale of fundamental processes, such as vibrational decay, dissociation and reactions. This is achieved through the use of femtosecond laser pulses and pump-probe spectroscopy [2].

1.2 Laser Spectroscopy

Lasers have provided scientists with an excellent tool with which to study the physical world. Their high intensities allow the properties of materials to be manipulated, forcing them to behave in uncharacteristic or *non-linear* fashions. However, they also prove incredibly useful due to their ability to generate ultrafast laser pulses. These have been measured to be as short as 250 attoseconds (10^{-18} s) [3], the quickest man-made event. With such temporally short pulses it is possible to clock the progress of physical events like dissociation or reaction that happen on ultrafast time scales.

However, science did not just wait around for the invention of the laser before trying to unravel the time scales of natural events. One of the most famous exam-

ples comes from a landscape photographer called Eadweard Muybridge (1830-1904). The story goes that Leland Stanford, a railroad baron and later founder of the university wagered that a horse is not in contact with the ground in mid-gallop. To prove his theory, Stanford hired Muybridge, who used twelve cameras separated by 27 inches, triggered by pieces of string stretched across the horse's path. The negatives picturing the horse mid-gallop are presented in Figure 1.1. At the horse's speed this corresponds to taking a photograph every 0.04 s, with an exposure of 0.002 s. Muybridge showed that the horse was not in contact with the ground in mid-gallop and started motion photography as it is known today.

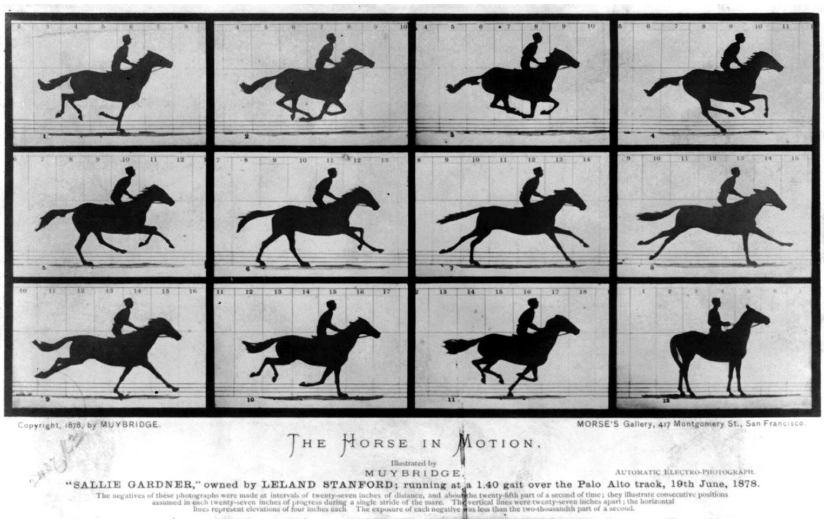

Figure 1.1: "The Horse in Motion" by Eadweard Muybridge."Sallie Gardner" owned by Leland Stanford; running at a 1:40 gait over the Palo Alto track on the 19th June 1878 [4].

While Muybridge's work was a form of time-resolved spectroscopy, modern experiments take a slightly different approach. To measure very fast phenomena (sub picosecond) with ultrafast laser pulses an experimental technique called pump-probe is used.

1.2.1 Pump-Probe

Pump-probe spectroscopy uses two laser pulses separated in time. The first 'pump' pulse initiates an event and sets time zero, the second 'probe' pulse can then measure the evolution of the system a set time delay after the pump. The time delay between pulses can be changed by letting the probe pulse travel a further distance to the sample, due to the constant speed of light it will arrive later than the pump. The pump pulses used in this thesis include mid-infrared and visible wavelengths. The infrared pump is used to investigate the dynamics of vibrational excitation and the visible pump is used to study processes such as heating, desorption, dissociation and reactions.

The probe used in these experiments is in fact two laser pulses, at mid-infrared and visible wavelengths. These pulses lead to a non-linear process called Sum Frequency Generation. The Sum Frequency (SF) process leads to the generation of visible light that can be easily detected with good sensitivity. As the incident mid-infrared pulse can be resonant with molecular bonds, the SFG light can give a vibrational spectrum of the system. By following the temporal evolution of this vibrational 'fingerprint' as a function of pump-probe delay, the perturbed system can be studied as a function of time after the pump pulse. A feature of SFG probe spectroscopy is that it is surface sensitive, proving ideal for studying molecular dynamics at surfaces.

1.2.2 Femtochemistry

The speed at which molecular bonds break and rearrange is rather fast. Atomic motion from a reaction centre is $\sim$1 kms^{-1}. Considering that average bond lengths are of the order of an Ångstrom, this gives $\sim$100 fs to identify intermediate structures. Hence, only with femtosecond time resolution can molecular reaction dy-

namics be frozen at particular stages on the potential energy surface [5].

The figure who lead the development of femtochemistry is Ahmed H. Zewail. He was awarded the Nobel prize for Chemistry in 1999 for "... showing that it is possible with rapid laser techniques to see how atoms in a molecule move during a chemical reaction" [6–8]. Research into the reaction dynamics of molecules adsorbed at surfaces has not achieved the level of sophistication as gas phase studies. This is largely due to the complexity introduced by a range of interactions between the solid interface and the reacting molecules. In particular, the effectiveness of metal surfaces as a rapid energy sink via electronic interactions, leads to very short excited state lifetimes.

Central to the study of chemical reaction dynamics is the Born-Oppenheimer potential energy surface (PES). However, several examples highlight that non-adiabatic coupling between nuclei and electrons does occur and have significant effects upon surface femtochemistry [9, 10].

1.2.3 Non-Linear Optics

The spectroscopic probe Sum Frequency Generation and other optical techniques discussed in this thesis are all examples of non-linear optical processes. In the following section I shall give a brief introduction to non-linear optics. For a full and more rigorous approach, I encourage the reader to consult other sources, including *Shen* and *Boyd* [11, 12].

Central to the following is the interaction between light and matter. For non-linear optics this can be refined further to describe the consequences of light changing the optical properties of a material. These changes can give rise to a wide range of optical effects that are not apparent in everyday life and only became easily observable with the invention of the LASER in the 1960s [13].

An electromagnetic wave consists of two orthogonal components, an electric

and magnetic field. It is the interaction of this electric field in particular that is of interest for non-linear optics. The polarisation $\mathbf{P}(t)$ induced in the electrons of a medium by a weak electric field $\mathbf{E}(t)$ is given by the following linear relationship:

$$\mathbf{P}(t) = \epsilon_0 \chi^{(1)} \mathbf{E}(t), \tag{1.1}$$

where $\chi^{(1)}$ is the linear susceptibility of the medium and ϵ_0 is the permittivity of free space. The induced polarisation in the material will be the same frequency as the incident electric field, hence the polarisation will generate a radiative field from the medium with the same frequency as the incident field. For light interacting with a surface, this would be the equivalent of reflection. However, this relationship breaks down at large electric field strengths ($\sim 10^9$ Vm^{-1}) and the polarisation can be expressed as a power series.

$$\begin{aligned} \mathbf{P}(t) &= \mathbf{P}^{(1)}(t) + \mathbf{P}^{(2)}(t) + \mathbf{P}^{(3)}(t) + \ldots \\ &= \epsilon_0 \chi^{(1)} \mathbf{E}(t) + \epsilon_0 \chi^{(2)} \mathbf{E}^2(t) + \epsilon_0 \chi^{(3)} \mathbf{E}^3(t) + \ldots \end{aligned} \tag{1.2}$$

where $\chi^{(2)}$ and $\chi^{(3)}$ are the second and third order non-linear susceptibilities, respectively. For many of the non-linear interactions described in this thesis, the most important term in expansion 1.2 is $\chi^{(2)}$, the second order non-linear susceptibility. $\chi^{(2)}$ is a measure of how much second order polarisation is generated and is a definitive property of the material. Later on in Chapter 4 the temporal profile of $\chi^{(2)}(t)$ shall be discussed, but for now we concern ourselves with its magnitude.

As the electric fields and polarisations given in equation 1.2 are vectors, the form of $\chi^{(1)}$ and $\chi^{(2)}$ must reflect the 3-D relationship between $\mathbf{E}(t)$ and $\mathbf{P}(t)$. The first order polarisation $\mathbf{P}^{(1)}$ generated in directions x, y or z is related to the electric field $\mathbf{E}$ in directions x, y or z by the following equations:

$$\mathbf{P}_x^{(1)} = \chi_{xx}^{(1)} \mathbf{E}_x + \chi_{xy}^{(1)} \mathbf{E}_y + \chi_{xz}^{(1)} \mathbf{E}_z \tag{1.3}$$

$$\mathbf{P}_y^{(1)} = \chi_{yx}^{(1)} \mathbf{E}_x + \chi_{yy}^{(1)} \mathbf{E}_y + \chi_{yz}^{(1)} \mathbf{E}_z \tag{1.4}$$

$$\mathbf{P}_z^{(1)} = \chi_{zx}^{(1)} \mathbf{E}_x + \chi_{zy}^{(1)} \mathbf{E}_y + \chi_{zz}^{(1)} \mathbf{E}_z. \tag{1.5}$$

The nine components of $\chi^{(1)}$ relate the electric field to the polarisation and $\chi^{(1)}$ is a second rank tensor. For SFG, where the polarisation generated depends upon the orientation of two electric fields $\mathbf{E}$ and $\mathbf{E}'$, $\chi^{(2)}$ is a third rank tensor and will have 27 components. If only a single component of the polarisation is being considered, its relationship to $\chi^{(2)}$ and the electric fields can be given by the general term $\mathbf{P}_i^{(2)} = \chi_{ijk}^{(2)}\mathbf{E}_j\mathbf{E}_k'$ where ijk can be x, y or z. For studies at surfaces it is common for the indices ijk to take values of s or p, where p refers to the electric field polarised perpendicular to the surface and s in the plane of the surface [14, 15].

There is an important symmetry consideration in $\chi^{(2)}$ processes: given $\mathbf{P}^{(2)} \propto \mathbf{E}^2$ then $\mathbf{P}^{(2)}(\mathbf{E}) = \mathbf{P}^{(2)}(-\mathbf{E})$. In a centrosymmetric medium, opposite directions are identical, so $\mathbf{P}^{(2)}(\mathbf{E}) = -\mathbf{P}^{(2)}(-\mathbf{E})$. These two conditions can only hold if the constant of proportionality, i.e. $\chi^{(2)}$, is zero. Thus only non-centrosymmetric media have a finite $\chi^{(2)}$. The most obvious examples of non-centrosymmetric media are surfaces and interfaces. Hence second order nonlinear processes such as SHG and SFG are *surface specific* and ideal for spectroscopic study of metal-adsorbate systems. Certain inorganic crystals also exhibit suitable symmetry to generate non-linear effects and are discussed in section 1.2.6 [14].

However, for an isotropic surface, many of the components of $\chi_{ijk}^{(2)}$ make no contribution. If the above symmetry criteria are rewritten for $\chi^{(2)}$ one gets:

$$\chi_{ijk}^{(2)} \equiv \chi_{\text{-}i\text{-}j\text{-}k}^{(2)} \tag{1.6}$$

and

$$\chi_{ijk}^{(2)} \equiv -\chi_{\text{-}i\text{-}j\text{-}k}^{(2)}. \tag{1.7}$$

These place constraints on the contributing components of $\chi_{ijk}^{(2)}$ for a surface. With the x and y axes in the plane of the surface, four examples serve to classify all the possible combinations [15, page 54]:

- zzz — reversing x or y axes has no effect — ✓

- xxx (and yyy) — reversing x axis (xxx →-x-x-x) implies $\chi^{(2)}_{\text{-}x\text{-}x\text{-}x} \equiv -\chi^{(2)}_{x\text{-}x\text{-}x} \equiv \chi^{(2)}_{xx\text{-}x} \equiv -\chi^{(2)}_{xxx}$ which does not satisfy both criteria, if $\chi^{(2)}$ is finite — ✗
- zxx (etc.) — reversing the x axis ($zxx \rightarrow z$-x-x) implies $\chi^{(2)}_{z\text{-}x\text{-}x} \equiv -\chi^{(2)}_{zx\text{-}x} \equiv \chi^{(2)}_{zxx}$ which has no overall sign change so does not violate the criteria — ✓
- zzx (etc.) — reversing x axis ($zzx \rightarrow zz$-x) implies $\chi^{(2)}_{zz\text{-}x} \equiv -\chi^{(2)}_{zzx}$ which has an overall change of sign and so does not satisfy both criteria — ✗

Given the x and y directions are equivalent, this leaves only 4 non-zero $\chi^{(2)}_{ijk}$ components for an isotropic surface:

$$\chi^{(2)}_{zxx}\left(\equiv \chi^{(2)}_{zyy}\right); \quad \chi^{(2)}_{xzx}\left(\equiv \chi^{(2)}_{yzy}\right); \quad \chi^{(2)}_{xxz}\left(\equiv \chi^{(2)}_{yyz}\right); \quad \chi^{(2)}_{zzz}.$$

With specific incident laser polarisations it is possible to probe particular susceptibilities. p-polarised light has electric field components along both the direction perpendicular to the surface (z) and one of the parallel directions (e.g. x), whilst s-polarised light has just one electric field component along the other parallel direction (e.g. y), see Figure 1.2.

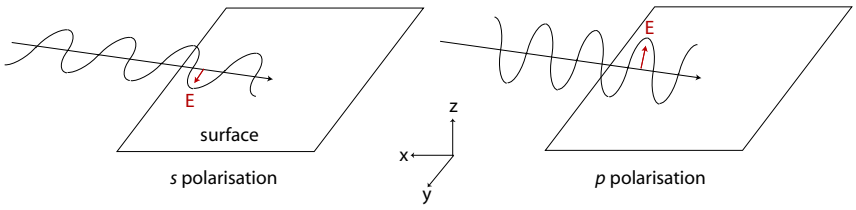

Figure 1.2: *s* and *p* polarisations of light incident on a surface [14].

Four combinations of incident and SF polarisations are available given the non-zero components of $\chi^{(2)}$ above, depending on which components of the **E** field are present in each direction, these are shown in Table 2.1. However, only two of these are usually seen for metal surfaces. The reflectivity of metal surfaces is high

for infrared light; for example the reflectivity of iridium at 5 μm is 96%. Only combinations with an IR field with some z component (i.e. p-polarised) contribute; the x and y components undergo a phase change upon reflection such that their intensities at the point of reflection are zero.

Polarisation Combination SF:VIS:IR	$\chi^{(2)}$ Components	Seen In Metals?
SSP	$\chi^{(2)}_{yyz}$	✓
SPS	$\chi^{(2)}_{yzy}$	✗
PSS	$\chi^{(2)}_{zyy}$	✗
PPP	$\chi^{(2)}_{zzz}, \chi^{(2)}_{xxz}$	✓
	$\chi^{(2)}_{zxx}, \chi^{(2)}_{xzx}$	✗

Table 1.1: Contributing polarisation combinations on metal surfaces [14].

At a molecular level, the non-linear response is given by the individual molecular hyperpolarisabilities, β. For an adsorbate system the total $\chi^{(2)}$ is given by the macroscopic average of β for the overlayer. In contrast to the surface bound Cartesian axis system (x, y, z), at an adsorbate level it is more convenient to use a molecular bound co-ordinate system (a, b, c), where c is the molecular axis and a is perpendicular to c [16]. Although an electric field in the surface co-ordinate system may be in a specific polarised direction (x, y, z), relative to the molecular based system, it could be resolved into components in all three molecular directions (a, b, c).

For orientation studies of adsorbed molecules, the involved media are described by macroscopic dielectric constants, which change abruptly at the surface. A non-linear polarisation sheet is embedded in a thin surface layer, which is characterised by specific dielectric properties. The choice of optical constants for the

surface layer are central to the success of the model and are given by the Fresnel matrix elements. It is therefore important to have data about the optical properties of the system and be able to quantify the β_{aac}/β_{ccc} hyperpolarisability ratio. This effectively tells you how easy it is to polarise the molecule in a direction perpendicular to the molecular axis. It is possible to determine the orientation of molecules adsorbed on surfaces by measuring the SF signal strength as a function of polarisation, as demonstrated for CO on Pd{111} [16]. Studies into the orientation of adsorbate systems are discussed further in section 3.3.2.

1.2.4 Second Harmonic Generation

The simplest non-linear optical effect is Second Harmonic Generation (SHG). This produces light at twice the frequency of the incident light, for example generating blue light (400 nm) from incident 800 nm.

If the electric field of the incident light is given by $\mathbf{E}(t) = \mathbf{E}\sin\omega t$, the second order polarisation $\mathbf{P^{(2)}}$ is given by:

$$\begin{aligned}\mathbf{P}^{(2)}(t) &= \chi^{(2)}\mathbf{E}^2(t) \\ &= \chi^{(2)}\mathbf{E}^2\sin^2\omega t,\end{aligned} \tag{1.8}$$

using the identity $\cos 2x = 1 - 2\sin^2 x$, equation 1.8 can be rewritten as:

$$\mathbf{P}^{(2)} = \frac{1}{2}\chi^{(2)}\mathbf{E}^2(1 - \cos 2\omega t). \tag{1.9}$$

The $\cos 2\omega t$ term corresponds to polarisation generated in the medium at twice the frequency of the incident wave [17]. In the context of wave/particle duality, this process can be thought of as taking two photons with frequency ω and merging them into one with frequency 2ω. SHG is commonly used in laser systems to generate more useful frequencies. An example of its use in the laser system described herein is the conversion of the output from a Nd:YAG laser from the

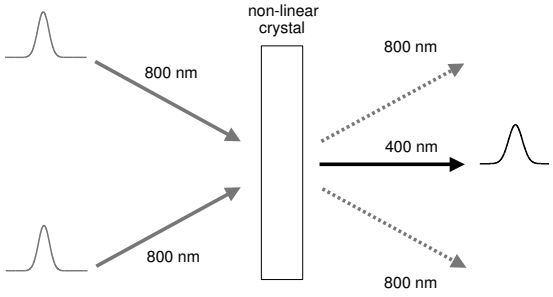

Figure 1.3: Second Harmonic generation in a non-collinear arrangement between two 800 nm laser pulses. In order for the electric fields to overlap, the pulses must arrive at the crystal at the same time. This provides a convenient way to temporarily align two laser pulses.

near infrared (1064 nm) to green light at 532 nm. Figure 1.3 shows the production of 400 nm blue SHG light from two 800 nm laser pulses crossed non-collinearly in a non-linear crystal.

The SHG direction of propagation is due to conservation of momentum, and shall be discussed in section 1.2.6. SHG can be used as a spectroscopic probe in its own right, one of the latest examples has been to study the diffusion of oxygen across a vicinal Pt{111} surface [18, 19]. The SHG signal proved to be sensitive to the oxygen coverage at step-sites, enabling the diffusion between steps and terraces to be observed after excitation with a femtosecond laser pulse.

1.2.5 Sum and Difference Frequency Generation

Non-linear processes can also be expanded to mix two photons of differing frequency, ω_1 and ω_2. At this point we shall change slightly our approach to representing the electric field: To avoid trigonometric manipulations $\mathbf{E}(t)$ can be represented as a complex exponential instead of a sine or cosine function, with the two

being related by the *Euler formula* $e^{i\theta} = \cos\theta + i\sin\theta$ [20]. By using a complex exponential, an electric field can be given as:

$$\mathbf{E}(t) = \mathbf{E}e^{-i\omega t} = \mathbf{E}\cos\omega t - i\mathbf{E}\sin\omega t. \tag{1.10}$$

Using this relationship it can be seen that the total electric field is given by:

$$\mathbf{E}(t) = \mathbf{E}e^{-i\omega t} + \mathbf{E}^* e^{i\omega t}, \tag{1.11}$$

where $\mathbf{E}^* e^{i\omega t}$ is the complex conjugate, which can also be denoted by (c.c.). This is found by replacing any i where it appears in a complex number with $-i$, so that $(c.c.) = \mathbf{E}\cos\omega t + i\mathbf{E}\sin\omega t$. With two electric fields incident upon the surface with frequencies ω_1 and ω_2, the total electric field can be given by:

$$\mathbf{E}(t) = \mathbf{E}_1 e^{-i\omega_1 t} + \mathbf{E}_2 e^{-i\omega_2 t} + (c.c.). \tag{1.12}$$

The combined electric field $\mathbf{E}(t)$ can now be substituted into equation 1.2 to generate a term for the total second order polarisation $\mathbf{P}^{(2)}(t)$.

$$\begin{aligned}
\mathbf{P}^{(2)}(t) &= \chi^{(2)}(\mathbf{E}_1 e^{-i\omega_1 t} + \mathbf{E}_2 e^{-i\omega_2 t} + (c.c.))^2 \\
&= \chi^{(2)}{\mathbf{E}_1}^2 e^{-2i\omega_1 t} + (c.c.) && (1.13)\\
&\quad + \chi^{(2)}{\mathbf{E}_2}^2 e^{-2i\omega_2 t} + (c.c.) && (1.14)\\
&\quad + 2\chi^{(2)}\mathbf{E}_1\mathbf{E}_2 e^{-i(\omega_1+\omega_2)t} + (c.c.) \qquad \text{[SFG]} && (1.15)\\
&\quad + 2\chi^{(2)}\mathbf{E}_1\mathbf{E}_2^* e^{-i(\omega_1-\omega_2)t} + (c.c.) \qquad \text{[DFG]} && (1.16)\\
&\quad + 2\chi^{(2)}\mathbf{E}_1\mathbf{E}_1^* + 2\chi^{(2)}\mathbf{E}_2\mathbf{E}_2^*.
\end{aligned}$$

The two terms 1.13 and 1.14 give the polarisation generated at the individual second harmonic frequencies $2\omega_1$ and $2\omega_2$, respectively. However, the terms 1.15 and 1.16 will have polarisation components at frequencies $(\omega_1+\omega_2)$ and $(\omega_1-\omega_2)$, called Sum and Difference Frequency Generation respectively.

Sum Frequency Generation (SFG) is the main spectroscopic technique employed in this work, and can be thought of as additively mixing two photons of frequency ω_1 and ω_2 to make a photon of frequency ω_{SF}. The application of SFG as a surface sensitive vibrational probe is explained in section 1.3.2.

Difference Frequency Generation (DFG) is another important non-linear technique, where for every photon created at ω_{DF}, one at ω_1 will be destroyed and one at ω_2 created ($\omega_{DF} = \omega_1 - \omega_2$). This is used to good effect to generate mid-infrared laser pulses by a process called Optical Parametric Amplification (OPA), which is described in section 2.2.3. DFG can also be used as a spectroscopic technique, an example of which is a study carried out by Tadjedinne *et al.* into the adsorption of CN on Au [21].

1.2.6 Phase Matching:

Conservation of Momentum and Energy

The generation of SHG, SFG and DFG light is highly directional. The direction of propagation for a laser beam is given by the wave vector **k**, which has the magnitude $|k| = 2\pi/\lambda$. **k** is the optical equivalent of Newtonian momentum and the addition and subtraction of wave vectors can be thought of completely analogously to calculating collision trajectories for billiard balls. This means that for a non-linear process, momentum and energy must be conserved and hence $\Delta\mathbf{k} = 0$. Therefore for SFG between an infrared and visible field the following relationships must be true:

$$\begin{aligned} \mathbf{k}_{\mathrm{SF}} &= \mathbf{k}_{\mathrm{IR}} + \mathbf{k}_{\mathrm{VIS}} \\ \frac{n(\omega_{SF})\omega_{SF}}{c} &= \frac{n(\omega_{IR})\omega_{IR}}{c} + \frac{n(\omega_{VIS})\omega_{VIS}}{c}, \end{aligned} \tag{1.17}$$

where $n(\omega_i)$ is the refractive index of the medium at the frequency ω_i. Unfortunately, equation 1.17 cannot be fulfilled in most materials because the refractive

index increases with frequency [22]. This can be bypassed by picking a material in which the SF light is produced with an orthogonal polarisation to the incident beams. For a birefringent crystal, the refractive indices are different for the two polarisation directions, *s* and *p*. Phase matching can then be achieved by rotating the angle of the non-linear crystal with respect to the beams.

1.3 Vibrational Spectroscopy at Surfaces

Vibrational spectroscopy probes the frequency at which molecular bonds vibrate. It is a powerful and non-invasive technique that allows the molecular environment and bonding structure to be examined. For example, changing a molecular bond by altering its electronic structure will change the characteristic frequency at which the bond vibrates.

For a molecule to be infrared active, it must have a permanent dipole moment and the molecular displacement concerned must change that dipole moment. In addition, the surface selection rule states that only molecules with a component of the dipole moment perpendicular to the surface will have large measurable infrared intensities, see Figure 1.4. This selection rule means that molecules with a dipole moment pointing in a direction parallel to a surface, are not visible using IR spectroscopy. A consequence of this is that the polarisation of the IR field must be perpendicular to the metal surface (*p* polarised), to allow the IR field to interact with the dipole moment of the molecule.

1.3.1 Reflection Adsorption Infrared Spectroscopy

The simplest approach to vibrational spectroscopy at surfaces is RAIRS. Here IR photons are incident upon the surface and where the energy of the photons coincides with a characteristic vibrational transition, the molecule will absorb a

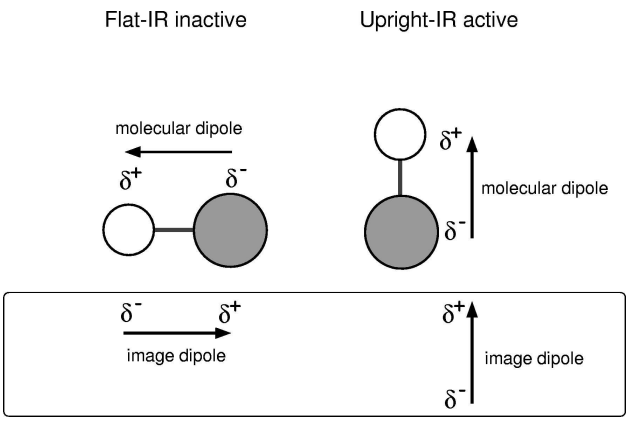

Figure 1.4: Schematic of IR surface selection rule for adsorbates on metal surfaces. When the molecule lies flat, the image dipole cancels with the molecular dipole, leaving no permanent dipole at the surface for the IR field to interact with.

photon. Upon absorption of the IR photon a first order polarisation is generated ($\mathbf{P}^{(1)}$), when this polarisation decays via non-radiative channels to the metal, a dip will be observed in the reflected IR spectrum. Unfortunately, as RAIRS is not inherently surface sensitive like SFG, a signal is detected from the bulk as well as the surface region. For the development of ultrafast RAIRS the cost of very sensitive detectors in the infrared region becomes prohibitively expensive.

1.3.2 Femtosecond Sum Frequency Generation

Central to SFG is the non-zero second order non-linear susceptibility $\chi^{(2)}$ at the surface, this makes it an ideal probe to study molecules at interfaces. Due to its surface selectivity and good molecular specificity, the main application of SFG is to monitor the intramolecular stretch of molecules on surfaces. Over the last decade, SFG has been extended to use broadband femtosecond IR laser pulses [23]. These pulses have a wide range of frequencies as a natural consequence of their ultrashort duration, due to the inverse Fourier relationship between frequency

and time, see section 2.2.1. The most useful consequence of this is that there is no need to scan the frequency of the IR light, and more importantly proves ideal for time-resolved studies of molecular dynamics.

To use SFG as a vibrational probe, two photons are incident upon the surface, a resonant mid-infrared and a non-resonant visible photon. This leads to generation of SF light in the visible region in a direction distinct from the reflected fields. Hence, detection of SF light is possible using relatively cheap and very sensitive iCCD detectors (Intensified Charge Coupled Device) and small changes can be studied with zero background.

Figure 1.5 shows the SFG process from a molecular perspective. From this

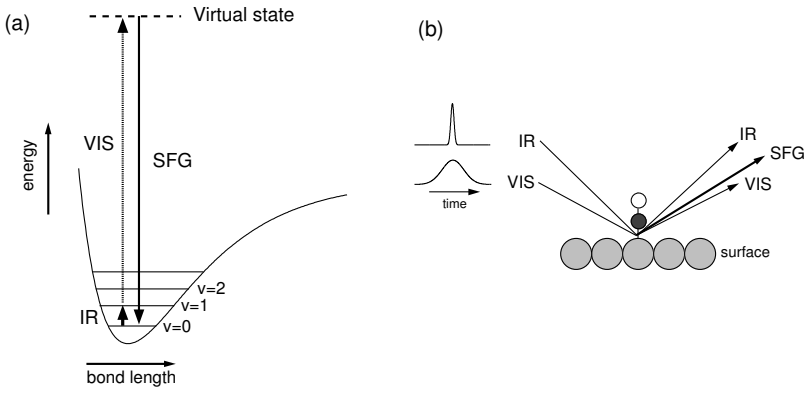

Figure 1.5: (a) Schematic illustrating the molecular picture of vibrational SFG at surfaces. A resonant infrared photon interacts with the molecular dipole leading to a vibrational transition from $v = 0$ to $v = 1$. At this point the molecule also absorbs a non-resonant visible pulse, which leads to up-conversion to a virtual state. Subsequent decay to $v = 0$ leads to emission of a photon at the sum frequency of the visible and resonant infrared photons. (b) Diagram of optical layout for a broadband frequency resolved SFG experiment at a surface. The sum frequency light generated from the narrowband visible and broadband infrared fields is propagated in a direction given by $\mathbf{k}_{SFG} = \mathbf{k}_{IR} + \mathbf{k}_{VIS}$.

point of view, the SF process can be thought of as a two photon excitation, in an analogous manner to other spectroscopic probes like Resonance Enhanced Multiphoton Ionisation (REMPI). The resonant IR photon induces a transition from the vibrational ground state $v = 0$ into the excited state $v = 1$, in a similar way to RAIRS. From here, absorption of the visible photon leads to a Raman transition to a virtual state. It is the decay from this state to $v = 0$, that emits the SF light in the visible. It is also possible to scan the frequency of the visible upconversion pulse until it is resonant with an electronic transition. This technique can therefore be used to probe the electronic structure of an adsorbate [24].

Most of the experiments described herein require a frequency resolved SF probe. To achieve this resolution and maintain temporal resolution with a femtosecond pump pulse, the IR polarisation is up-converted with a narrow band visible beam. Armed with an ultrafast frequency resolved probe, a femtosecond pump pulse can be added to perturb the system. Changing the delay between pump and probe pulses allows the time scale of the system's response to be unwrapped. This pump pulse can be an IR pulse, if vibrational dynamics are to be probed, or a visible pump to probe nuclear dynamics of diffusion [25], desorption [26–28], dissociation or reactions.

1.3.3 SFG Spectra of Metal Adsorbate Systems

For a metal-adsorbate system both the molecule and surface will give a SF signal. The total second order susceptibility $\chi^{(2)}$ is a combination of non-resonant and resonant contributions:

$$\chi^{(2)} = \chi^{(2)}_{NR} + \chi^{(2)}_{RES}, \tag{1.18}$$

where $\chi^{(2)}_{NR}$ and $\chi^{(2)}_{RES}$ are the non-resonant and resonant second order susceptibilities from the surface and adsorbate respectively. The intensity of the SF signal is

then proportional to the square of $\chi^{(2)}$:

$$I_{SF} \propto |\chi^{(2)}_{NR}|^2 + |\chi^{(2)}_{RES}|^2 + 2|\chi^{(2)}_{NR}||\chi^{(2)}_{RES}| \cos \Delta\phi, \tag{1.19}$$

where $\Delta\phi$ is the phase relationship between the resonant and non-resonant signals. The origin of the non-resonant signal is depicted in Figure 1.6. Each infrared photon in a broadband laser pulse can make an infrared transition to a virtual vibrational state, followed by a visible transition to a virtual electronic state. As neither of these transitions match a resonance within the molecule or metal surface, the magnitude of this signal is small relative to the resonant adsorbate stretch.

Shen derived an expression for $\chi^{(2)}_{RES}$ for molecular co-ordinates l, m and n, using a coupled wave approach and perturbation theory ([11, page 171], [29] with adaptations from [30])

$$\begin{aligned} \left(\chi^{(2)}_{RES}\right)_{lmn} &= \frac{NA_nM_{lm}\Delta\rho}{\hbar\left(\omega_{IR} - \omega_{\mathrm{v}} + i\Gamma_{\mathrm{v}}\right)}; \\ A_n &= \langle g | e\hat{r}_n | v \rangle, \\ M_{lm} &= \sum_s \left[\frac{\langle v | e\hat{r}_m | s \rangle \langle s | e\hat{r}_l | g \rangle}{\hbar\left(\omega_{SF} - \omega_{s\to g} + i\Gamma_{s\to g}\right)} - \frac{\langle v | e\hat{r}_l | s \rangle \langle s | e\hat{r}_m | g \rangle}{\hbar\left(\omega_{VIS} - \omega_{s\to g} + i\Gamma_{s\to g}\right)} \right] \end{aligned} \tag{1.20}$$

where A_n and M_{lm} are the IR and Raman transition moments, $e\hat{r}$ is the dipole operator, v, s and g refer to the vibrational, virtual (intermediate) and ground states, $\Delta\rho$ is the population difference between $\langle g |$ and $\langle v |$, ω_v and Γ_v are the vibrational resonance frequency and half-width, and N is the density of surface molecules. This means that the second order resonant susceptibility is proportional to the probability of an IR transition, A_n, *and* a Raman transition, M_{lm}, with an overall (square rooted) Lorentzian profile.

Hence the resonant polarisation in the frequency domain, $\mathcal{P}^{(2)}_{RES}$, for one dominant transition can be expressed as

$$\mathcal{P}^{(2)}_{RES}\left(\omega_{SF}\right) \propto A_nM_{lm}\left(\omega_{SF}\right) \frac{E_{IR}E_{VIS}}{\omega_{IR} - \omega_{\mathrm{v}} + i\Gamma_{\mathrm{v}}}, \tag{1.21}$$

and the total susceptibility from equation 1.18, can be written as

$$\chi^{(2)} = A_0 e^{i\phi} + \sum_n \frac{A_n}{\omega_{IR} - \omega_n + i\Gamma_n} \tag{1.22}$$

where A_0 and ϕ are the magnitude and phase of the non-resonant contribution, and A_n, ω_n, Γ_n are the amplitude, frequency and half-width of the resonance. To account for the finite width and Gaussian shape of the visible upconversion pulse, a Voigt function instead of a Lorentzian is used to describe the resonance.

The phase difference between the non-resonant and resonant signals dictates the shape of the resultant spectra, and can lead to large peak asymmetries. A range of different modelled SFG spectra are plotted as a function of the phase difference in Figure 1.7. The changes can be even more pronounced for systems where the non-resonant signal is of similar magnitude to the resonant. Under these conditions the resonant signal may occur as a dip in a broad background.

It can also be seen from equation 1.19 that the non-resonant signal enhances the resonant signal via the final cross term. The non-resonant signal is about two orders of magnitude larger on iridium than other metals studied in Cambridge, such as ruthenium. This gives enhanced SF signals and improved experimental capabilities that were not possible in earlier experimental studies.

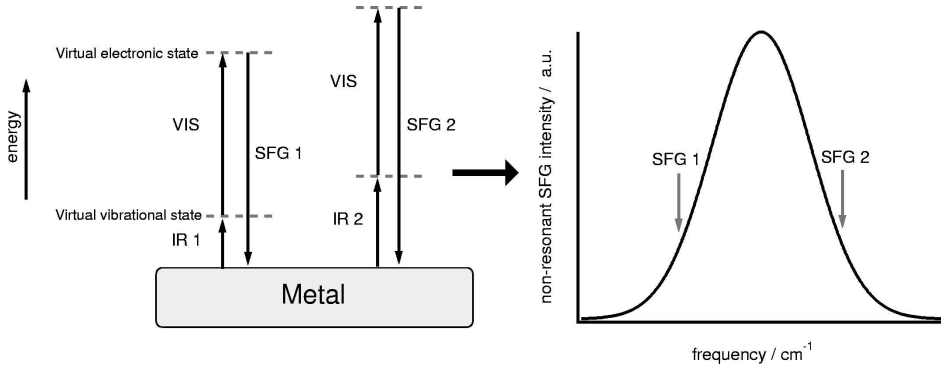

Figure 1.6: Origin of non-resonant SFG signal.

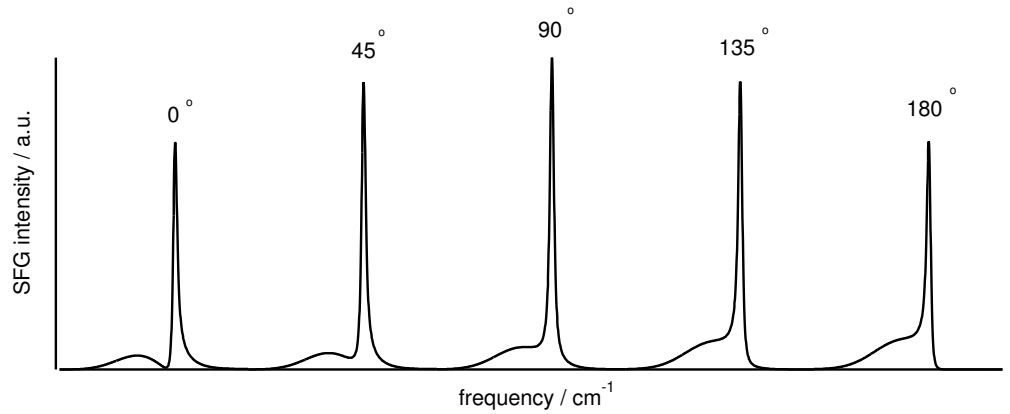

Figure 1.7: Schematic showing the different peak shapes for SFG spectra from an adsorbate/metal system due to varying phase difference between the resonant and non-resonant signals. The spectra show the variation in phase difference for five constant values of the non-resonant phase (0-180°). The peak asymmetries are due to interference between the resonant and non-resonant signals.

1.3.4 Previous Work

Cambridge

Over the last 10 years a wide range of experiments have been carried out in the Cambridge surface science femtosecond laser laboratory. The first of these used a mass spectrometer for time of flight measurements, to monitor the products of laser induced desorption from the Pt{111} surface. The desorption of multilayer benzene with an 800 nm laser pulse and the oxidation of CO by O_2 with a 400 nm laser pulse were studied and the results published in the following [31–33].

Later experiments have focussed on studying molecules when they are on the surface, as only a limited amount of information can be extracted when they have left. This has been achieved through the development of Sum Frequency spectroscopy. Since the implementation of SFG, studies have been carried out

on the Ru{10$\bar{1}$0} and Ir{111} surfaces. The adsorption characteristics and desorption mechanism of CO on Ru{10$\bar{1}$0} were studied and provided an excellent *proof of concept* for the application of SFG to study UHV surface systems in Cambridge [27, 34].

Since then work has focussed on studying the iridium {111} surface with SFG, as part of a wider multidisciplinary project into NO reduction on iridium/gold catalysts. The adsorption of CO and NO on Ir{111} was studied, including the observation of vibrational *hotbands* for CO [35]. In addition, the adsorption of CO and NO on bimetallic Au/Ir{111} surfaces was carried out, providing information on the mechanism of gold growth and the decomposition of NO on Au/Ir{111} systems [36].

Elsewhere

The work presented herein focuses on the molecular, vibrational and reaction dynamics of adsorbates, with a particular focus on non-adiabatic processes. The implications of previous experiments shall be discussed where relevant in the following chapters, but shall be briefly summarised here.

Excellent reviews of femtochemistry at metal surfaces and non-adiabatic reaction dynamics are presented by Frischkorn [37] and Matsumoto [38]. A significant part of surface femtochemistry has focused on the desorption of diatomic molecules such as NO, CO, or O_2. Pioneered by Ho and co-workers [39] the CO oxidation reaction ($1/2O_2$ + CO $\rightarrow$ CO_2) on Pt{111} has served as a prototype for molecular formation/association reactions. In this reaction, the dissociation of molecular oxygen leads to the formation of CO_2 in a similar manner to the reaction under thermal (equilibrium) conditions.

In contrast, for CO oxidation on Ru{0001}, Ertl [26] used two pulse correlation measurements to show that hot electron-mediated activation of coadsorbed

atomic oxygen can induce a chemical reaction that is not accessible under equilibrium conditions. This means that the reaction path for CO oxidation on Ru is switched on only by femtosecond laser excitation. During the past few years, the associative formation and desorption of molecular hydrogen ($H + H \rightarrow H_2$) on Ru by excitation of the chemisorbed atomic species has also been demonstrated [40].

Direct excitation of the adsorbate-surface bond has been demonstrated by Petek *et al.* for Cs/Cu{111}, using time-resolved two-photon photoemission spectroscopy [41]. Promotion of a single electron into the antibonding Cs 6s resonance by a femtosecond-laser pulse launches a vibrational wave packet motion of the Cs atom away from the surface. These experiments have been extended by Watanabe *et al.* [42] to include coherent phonon excitation of alkali metals (Cs, K) on Pt{111} at higher fluences. The amplitude of the adsorbate-surface stretch vibration can be controlled to a degree by sequential excitation [43]. Although there are many problems with developing these experiments further, they do show a pathway to control surface femtochemistry by inducing vibrational coherent wave packet motion [37].

Recent progress in the generation of ultrashort XUV-pulses by means of high harmonic generation provides a means to monitor the dynamics of surface chemical reactions. This enables time-resolved photoemission spectroscopy to measure the laser-induced changes of an adsorbate-surface bond with sub-100 femtosecond time-resolution [44].

The dynamics of desorption and latterly diffusion [25] have been studied using femtosecond 800 nm pump-SFG probe experiments for CO on platinum [28, 45], copper [46, 47] and ruthenium surfaces [26]. Vibrational dynamics have been probed using a picosecond IR pump laser pulse and a time-resolved RAIRS probe to study CO/Pt{111} [48]. This was followed by picosecond IR pump-SF probe experiments to study CO/Cu{100} [49] and CH_3S on Ag{111} [50]. No studies into

vibrational dynamics have been conducted on metal surfaces using femtosecond laser pulses, which is an interesting gap, considering vibrational lifetimes on metal surfaces are of the order of a picosecond.

Other pump-SFG probe studies have included the melting and recrystallisation of D_2O on CO/Pt{111} with a picosecond 800 nm pump [51], the electronic excitation of CO/Ni{111}/NiO{111} systems with a picosecond UV pump [52] and conformational studies of formate on Ni{111}/NiO{111} with a picosecond near infrared pump [53]. However, these experiments mainly follow thermal equilibrium processes following a laser induced temperature change and hence do not qualify as non-adiabatic processes. More recent SFG studies at surfaces have looked at trying to probe the dynamics and transfer mechanisms for biologically important surfaces, such as phospholipid membranes [54–56].

1.4 Thesis Outline

Chapter 2 shall introduce the equipment and techniques required to carry out the experiments presented in Chapters 3, 4 and 5. This shall cover the basic principles behind the generation and amplification of the femtosecond laser pulses required for sum frequency spectroscopy and an overview of the surface science approach in UHV.

Chapter 3 focuses primarily on the response of adsorbate molecules (CO and NO on Ir{111}) to ultrafast laser heating with a visible (800 nm) pump pulse. The intramolecular stretch of the adsorbate is then followed on a sub-picosecond time scale using SFG. Chapter 4 looks at the vibrational dynamics of the intramolecular adsorbate bond. Information can be retrieved from the IR spectra, free induction decay and photon echo experiments. Pump-probe spectroscopy can also be applied using a mid-infrared pump pulse. Chapter 5 uses the information gathered

in Chapter 3 to look at the reaction dynamics between CO and NO coadsorbed on the iridium surface. Chapter 6 sums up my contribution to the field of surface reaction dynamics and provides an outlook for further work.

Chapter 2

Experimental

2.1 A UHV Femtosecond SFG Spectrometer

To conduct state of the art time-resolved spectroscopy on well defined surface systems, a high quality femtosecond laser and Ultra High Vacuum (UHV) system are required. Upon acquiring these basic parts, they need to be integrated to produce a working and reliable spectrometer [14]. Unfortunately, it is not always a marriage made in heaven, as the UHV requirement for extended high temperature bakeouts is not an ideal environment for a complicated laser system. In the following chapter I shall cover the layout in more detail and explain a little about the workings of the important components and processes. I shall then move on to explain how the UHV-SFG spectrometer is used to collect SF spectra of metal adsorbate systems.

Briefly, a pair of femtosecond laser pulses (mid IR and visible) are focused on to the surface of a liquid nitrogen cooled sample mounted in a UHV chamber. The SF light generated from the surface is collected from the chamber and dispersed/imaged using a spectrograph and CCD (a very sensitive visible camera). The SF light gives a vibrational spectrum of the species present at the surface of the sample. In more complex experiments, a third pulse may be added to conduct

pump-probe spectroscopy.

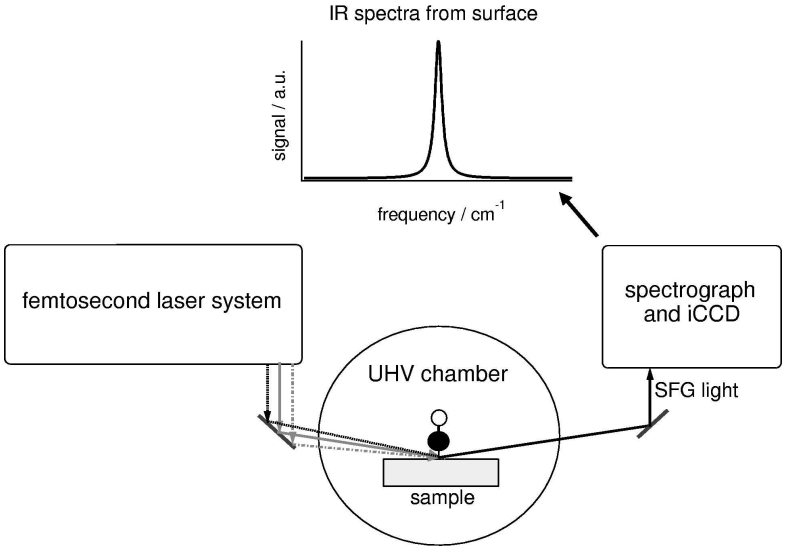

Figure 2.1: Schematic showing the main components of a UHV-SFG spectrometer and its use to produce vibrational spectra of adsorbates at surfaces.

2.2 Laser System

Femtosecond pulses are generated by a Spectra Physics *Tsunami* Ti:sapphire oscillator. The *Tsunami* is pumped by a 10-W argon ion laser and generates 90 fs pulses, centred at 800 nm at 82 MHz. The output direct from the exit of the *Tsunami* (~10 nJ per pulse) is not capable of producing the intensities needed to generate mid-infrared light. Therefore, upon leaving the oscillator, pulses are amplified by a Spectra Physics *TSA* regenerative amplifier, pumped by a 10-Hz Nd:YAG laser. The amplifier has an output of ~7 mJ with a pulse duration of ~150 fs.

The output from the amplifier is split into three separate beam paths:

1. 2.5 mJ is used to pump a TOPAS Optical Parametric Amplifier for the gen-

eration of mid-infrared light for the SF probe (3-10 μm,10 μJ, 240 fs.)

2. 2 mJ is sent via a pulse shaper for 800 nm probe up-conversion.

3. 2.5 mJ is directed down the pump path. This can be used unchanged at 800 nm or used to pump a second OPA to produce a tuneable near/mid-infrared pump.

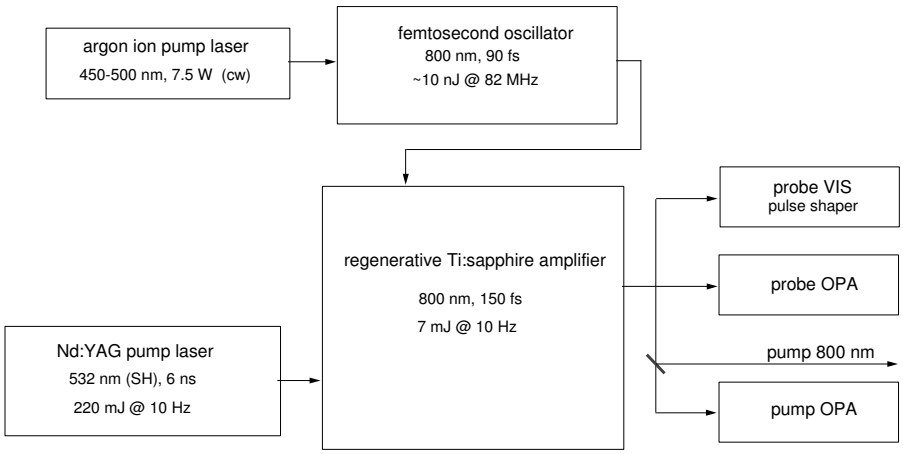

Figure 2.2: Schematic of the main components of the laser system.

2.2.1 Generating Femtosecond Pulses

In order to make a temporally short laser pulse, you need to take advantage of the inverse Fourier relationship between frequency and time. This essentially says that if you want something short in the time domain, it must be composed of many frequency components. Put more relevantly, to make an ultrashort laser pulse, it must consist of a wide range of frequencies. This goes against the classic idea that all laser pulses are monochromatic, but it does have its advantages.

To make a laser cavity that can accommodate a range of laser frequencies, a lasing medium is needed that has wide absorption and emission spectra. However, this is only half the story. If all the different frequency modes do not have a common phase relationship, then destructive interference will dominate. The challenge is to make sure all the laser modes present are in phase at some point in the cavity. This process is called *mode locking* and is depicted schematically in Figure 2.3 [57, 58].

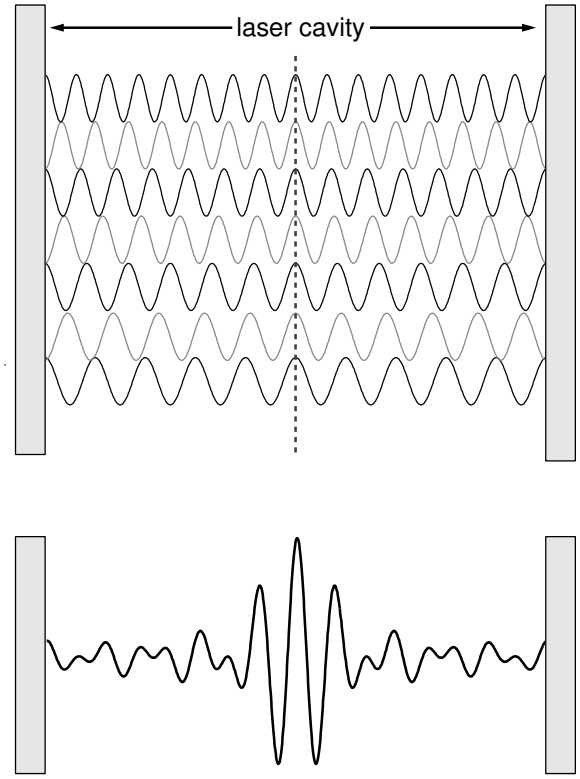

Figure 2.3: Schematic of short laser pulse generation. Using a wide bandwidth lasing medium mode locking of different frequency modes leads to constructive interference and a short laser pulse.

2.2.2 Amplification of Femtosecond Pulses

The amplification of nJ femtosecond pulses to the mJ level is not trivial. Simple amplification by a Nd:YAG laser in a medium such as Ti:sapphire would generate large intensities, leading to unwanted non-linear optical effects and crystal damage. Hence, a process called *chirped pulse amplification* is used, where the fs pulse is stretched out in time, amplified and then re-compressed, thus reducing the intensities during amplification, see Figure 2.4.

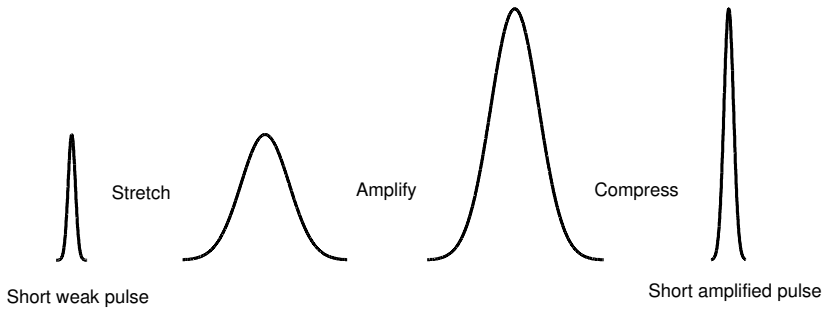

Figure 2.4: Chirped pulse amplification, the peak widths correspond to temporal pulse lengths.

The fs pulse is temporally stretched by diffracting it off a grating, splitting it into its spectral components and then making the higher frequency end of the spectrum travel a longer path than the lower frequency part. When the pulse is recombined it is temporally longer (~200 ps) with a variation of frequencies during the duration of the pulse, also known as a *chirp*.

The amplification of the temporally stretched pulse consists of two stages, a regenerative amplifier and a double-pass. The regenerative stage takes a seed pulse from the stretcher and amplifies it by passing it a finite number of times through a saturated Ti:sapphire crystal in a cavity, pumped by a Nd:YAG laser. The alignment of seed and pump beams into the cavity has a considerable effect

on the quality and stability of the amplifier output. The ejection of the amplified pulse from the cavity is carried out by a Pockel's cell, which is triggered at a user-defined delay relative to the Q-switching in the Nd:YAG pump laser. The pulse is kept in the cavity until after the maximum to ensure maximum stability. The quality of the amplifier output is primarily checked by monitoring a photo-diode situated behind the cavity mirror (Figure 2.5), and also by FROG (section 2.4.1). The double-pass amplification stage is simpler and aligned purely to maximise energy output. After amplification the pulse is re-compressed in time by the reverse of the earlier process, to yield an intense fs laser pulse.

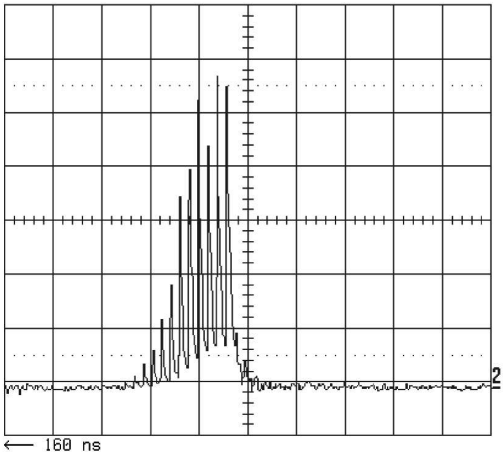

Figure 2.5: Cavity trace of regenerative amplifier. Each peak refers to a round trip of the cavity and amplification of the pulse in the pumped Ti:sapphire crystal. The *x* axis corresponds to 50 ns per square and the *y* axis to 100 mV per square.

2.2.3 Generation of Mid-IR Pulses

The generation of mid-infrared light (3-10 μm) is carried out in a two stage commercial unit, using Optical Parametric Amplification (OPA) in a Beta Barium Borate (BBO) crystal, followed by difference frequency generation in a silver gallium

sulphide ($AgGaS_2$) crystal. Parametric amplification generates and amplifies two beams called the idler ω_i and signal ω_s, which are related to the pump beam ω_p by the following coupled difference frequency relationship:

$$\omega_i = \omega_p - \omega_s$$

$$\omega_s = \omega_p - \omega_i.$$

This means that over five passes of the BBO crystal, the signal and idler will mutually seed amplification of themselves from the pump beam. The process is initiated by generating a weak broadband light source by a process called *superfluorescence* [11]. It is from this continuum that the signal frequency is taken and used to initially generate the idler. The signal frequency picked is determined by phase matching criteria and can be changed by moving the angle of the BBO crystal.

For an 800 nm pump beam this process can generate signal and idler frequencies in the near-infrared. A simple difference frequency process is then carried out to generate mid-infrared that is tuneable between 3-11 μm. For example, to produce light at 5000 nm (2000 cm^{-1}), the following signal and idler wavelengths are produced:

$$\begin{aligned} \frac{1}{800\,\text{nm}} &= \frac{1}{1380\,\text{nm}} + \frac{1}{1900\,\text{nm}} \\ \omega_p &= \omega_s + \omega_i. \end{aligned}$$

The phase matching angle in the $AgGaS_2$ crystal is then set to give the difference frequency between the signal and idler, to give light at 5000 nm:

$$\begin{aligned} \frac{1}{1380\,\text{nm}} - \frac{1}{1900\,\text{nm}} &= \frac{1}{5000\,\text{nm}} \\ \omega_s - \omega_i &= \omega_{IR}. \end{aligned}$$

At 5000 nm, the TOPAS has an output of ~10 μJ, with a pulse length of ~240 fs and frequency bandwidth of ~150 cm^{-1}.

2.2.4 Pulse Shaper

The pulse shaper converts a broadband femtosecond 800 nm pulse into a narrowband picosecond pulse, which is needed for frequency resolution in the SF probe. The pulse shaper consists of a grating, lens, slit and mirror, see Figure 2.6. The broadband pulse is spectrally dispersed off the grating and focused by the lens onto the mirror. At this point, the slit selects only a small part of the spectrum, which is then reflected back by the mirror slightly below the incident plane. Upon incidence on the grating a second time, the pulse is reconstructed and a picosecond pulse produced due to the reduced bandwidth.

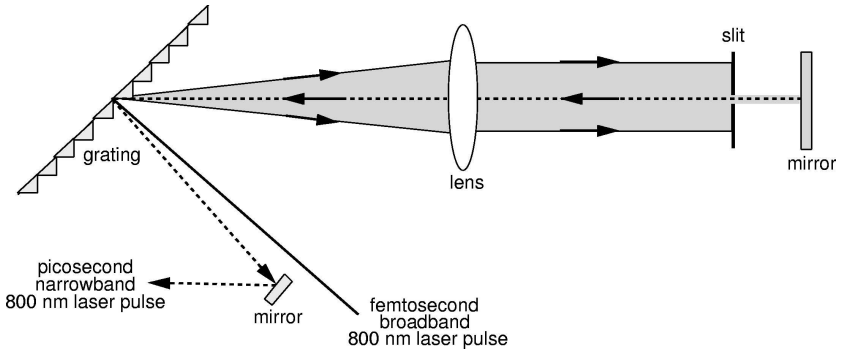

Figure 2.6: Schematic diagram of the 800 nm pulse shaper, which is used to convert femtosecond broadband pulses into picosecond narrowband pulses for frequency resolved SFG up-conversion. Solid lines represent the incoming path and dashed lines are the outgoing path. In reality, the outgoing path returns directly underneath the incoming one, but is shown offset for clarity.

A feature of this arrangement is that removing the slit will produce femtosecond broadband pulses, essentially not changing the input pulse. This is important to help alignment and for carrying out SFG experiments in the time domain, such as free induction decays, see Chapter 4.

2.3 UHV Chamber

The UHV chamber (Vacuum Generators) has two experimental levels. The upper level has a quadrupole mass spectrometer, LEED optics, argon ion sputter gun and gas doser. The lower level is the main optical experimental platform, with an IR transparent MgF_2 optical window (transmittance 0.12-7.0 μm), K/Cs getter source, a commercial metal evaporator (Omicron) and electron gun/hemisperical analyser for Auger spectroscopy.

The chamber has a base pressure of $5{\cdot}10^{-11}$ mbar (measured with a Varian ion gauge) and is pumped by a rotary roughing pump, oil diffusion pump, Varian Diode ion pump and a titanium sublimation pump. After venting, the chamber is baked for about 48 hours to ensure UHV conditions. The sample manipulator is a rotatable *xyz* translation stage, differentially pumped by the roughing pump.

2.3.1 Surface Science Techniques

Auger Electron Spectroscopy (AES)

AES is a widely used surface science technique that allows a quantitative analysis of the elemental distribution at a surface. An incident electron (several keV) causes photoemission of a core electron from an atom, this inner shell electron hole is then quickly filled (within 10^{-16} to 10^{-12} s) by an electron from a lower binding energy. The energy made available by this down electron can be transferred to another electron, an Auger electron. The kinetic energy of the Auger electrons are characteristic of the binding energies of electrons in the atom and are hence specific to different elements. AES can be used to probe the structure and growth mechanism of bi-metallic surfaces as well as being a useful probe for analyzing surface cleanliness. Auger spectra are plotted as the derivative of the number of electrons N(E) against energy, as it allows easier detection of small

peaks on a large background [1].

Low Energy Electron Diffraction (LEED)

LEED is a tool for determining the structure of a surface, electrons with a kinetic energy of 20-1000 eV are elastically back scattered from the surface to give a diffraction pattern on a phosphor screen. This diffraction pattern is dependent upon the de Broglie wavelength of the incident electrons matching the atomic spacings present at the surface. The powerful structure determination capabilities of LEED are not especially applied on this experimental apparatus, instead it is mainly used to confirm good order at the surface.

Temperature Programmed Desorption (TPD)

TPD is a relatively simple technique, but surprisingly powerful in its capabilities. It is carried out by applying a temperature ramp to the sample and then following the rate of desorption with a quadrupole mass spectrometer as a function of temperature. The analysis of a set of TPD spectra can yield information regarding the nature and strength of lateral adsorbate interactions, the activation energy for desorption and the relative surface coverage. The use of TPD is also a quick and easy way to establish cleanliness of the surface [1].

2.3.2 Single Crystal Surface

The surface studied in all experiments described in this thesis is the {111} single crystal facet of iridium. The structure of the {111} facet is presented in Figure 2.7, it has the highest surface atom density and lowest energy for a face centred cubic (fcc) metal. The crystal (8 mm $\times$ 5 mm $\times$ 1 mm) was purchased from Metal Crystals and Oxides and cut within an accuracy of $\pm\,0.5^{\circ}$.

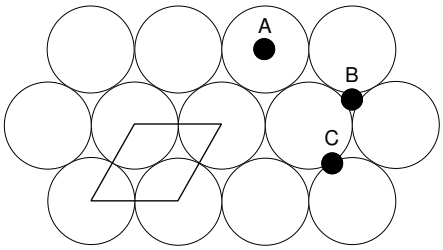

Figure 2.7: Structure of {111} single crystal facet for a fcc metal. Highlighted is the (1×1) unit cell and the different adsorption sites (A) atop, (B) hollow and (C) bridge.

Mounting

The crystal temperature can be varied from 100 K to 1500 K. Cooling is carried out via a stainless steel cold finger, which is connected to a small liquid nitrogen reservoir at the top of the sample manipulator. The crystal temperature can be increased by resistive heating, as the electrically insulated sample is connected to a 30 A power supply. The temperature can be controlled and programmed to follow set heating and cooling ramps through the use of a Eurotherm temperature control unit. The sensor for this is a chromel-alumel thermo-couple, spot welded to the back face of the crystal. The crystal is mounted onto a pair of tungsten heating wires, with the aid of a thin piece of tantalum foil that covers the back face of the crystal (Figure 2.8). The copper block that is fixed directly onto the cold finger is electrically insulated from the sample mount by two indium coated sapphire disks. These allow excellent heat transfer away from the crystal, but are also electrical insulators.

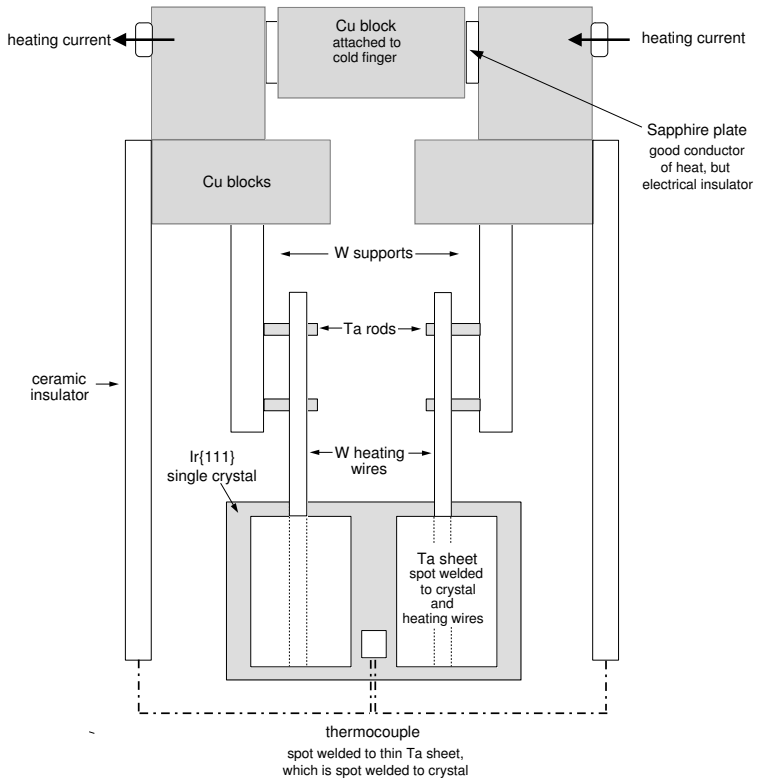

Figure 2.8: Diagram of sample mounting to heating wires and cold finger, showing the back face of the Ir{111} crystal.

Cleaning and Characterisation

The Ir{111} crystal was cleaned by repeated cycles of argon ion bombardment, oxidation (10^{-7} mbar) at 800 K and annealing at 1500 K. This was carried out until impurities (mainly carbon) were reduced, according to Auger spectroscopy, see Figure 2.9. The long range surface order of the single crystal was checked with low energy electron diffraction (LEED). The quality of LEED images from the crystal was not excellent, but compared well with other Ir{111} LEED results in the literature [59]. Figure 2.10 is a (1×1) LEED pattern from the clean Ir{111} surface at 100 K and Figure 2.11 shows a (2×2) overlayer LEED pattern for the oxygen covered Ir{111} surface.

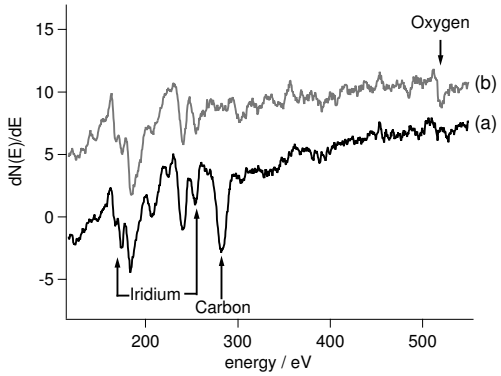

Figure 2.9: Auger electron spectrum of Ir{111} crystal before (a) and after (b) oxygen treatment. The oxygen can be simply removed by heating to 1500 K.

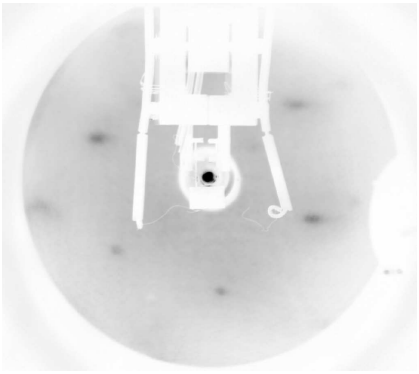

Figure 2.10: (1×1) hexagonal LEED pattern from clean Ir{111} surface, contrast inverted.

A (2×2) LEED pattern can originate from either a p(2×2) surface structure (0.25 ML) or three domains of a (1×2) structure rotated 120° (0.5 ML). The oxygen surface coverage has been determined from XPS to be 0.5 ML [60,61], leading to the assignment of the (1×2) 0.5 ML oxygen surface structure on Ir{111}.

Once the crystal was bulk clean, a short exposure to oxygen (10^{-7} mbar) at 1400 K was sufficient for day-to-day cleaning. The main day-to-day indicator for surface cleanliness was oxygen temperature programmed desorption (TPD)

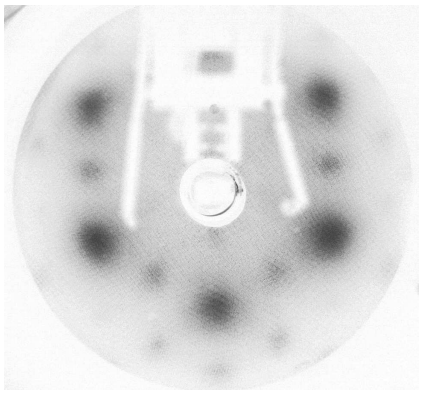

Figure 2.11: (2×2) overlayer LEED pattern from saturation O_2 coverage on Ir{111}. The background has been reduced to highlight the overlayer spots.

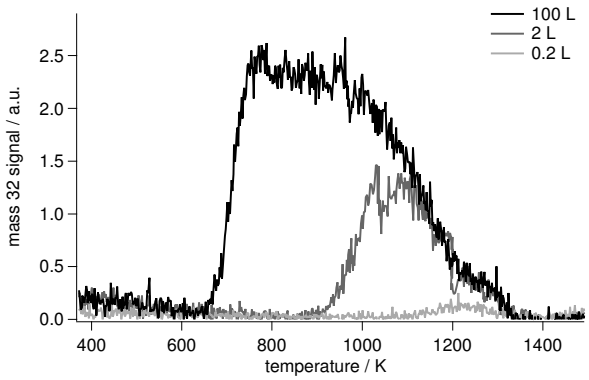

Figure 2.12: Oxygen TPDs from a clean Ir{111} surface.

spectra from the surface.

Figure 2.12 shows three different oxygen TPD traces for low to high doses (0.2-100 L) of oxygen onto the Ir{111} surface at 100 K. The shape and magnitude of these traces proved to be very sensitive to a dirty surface, allowing quick and effective sample characterisation.

2.4 Alignment

Without doubt, the greatest and most difficult challenge in maintaining the effectiveness of a UHV-SFG spectrometer is the maintenance of good laser stability and beam overlap on the sample. Over the period of my experiments, the stability has improved greatly from a few hours to nearly 48 hrs in some instances. Although the lasers do still need extensive realignment on occasions, day-to-day stability and reproducibility has been greatly improved by a policy of non-interventionism with respect to laser adjustment during the course of a day's experiments. Day-to-day alignment is a compromise between maintaining current performance and striving for *best ever* performance, hence achieving improved reproducibility between data sets on consecutive days.

2.4.1 Lasers

The *Tsunami* oscillator requires little daily alignment and provides excellent stability, given stable mounting and temperature conditions. The spectrum of the oscillator is monitored in real time with a commercial spectral analyser, which uses a rotating diffraction grating and photodiode.

Alignment of the regenerative amplifier is less of a given and can occupy many hours given the chance. Provided the stretcher and compressor paths are correctly aligned, the main task is to ensure that the pump and seed beams overlap in the cavity. The Nd:YAG pump beam has a tendency to drift during the day, hence requiring an extended warming up period of several hours, to avoid later readjustment. The OPAs performance is largely dependent upon good regen stability and compressor grating position. Input alignment is checked through external and internal input irises. The stability and magnitude of output energy for all beams is monitored with a pyroelectric energy meter.

Pulse Characterisation

It is important that the spectral and temporal profile of the laser pulses is monitored on a day-to-day basis. A good knowledge of the laser pulse characteristics is vital for the analysis of SFG spectral data and the correct alignment of optics in the laser system. Several different techniques are available to do this, the main ones applied on a day-to day basis include FROG analysis and *in situ* cross-correlation from the iridium surface.

Frequency Resolved Optical Gating (FROG) is a powerful pulse analysis technique that can measure the temporal and spectral width, spatial chirp and pulse front tilt. Further information about this technique can be found in [62]. A commercial FROG called GRENOUILLE is used to characterise the femtosecond 800 nm output from the *Tsumani* and regenerative amplifier. This is a very useful unit because it provides a live visual FROG trace, which plots the frequency of the pulse against time. The real-time feedback is required for aligning the regenerative amplifier and the temporal pulse width is set as a benchmark for the measurement of other laser pulses in the system via cross-correlation.

With the spectral and temporal width of the femtosecond 800 nm laser pulse known, it can be cross-correlated with the femtosecond infrared pulse. The beams are focussed onto the Ir{111} surface and scanned past each other in time. The resulting SFG intensity (I_{SFG}) is then plotted against the pulse delay τ:

$$I_{SFG}(\tau) = \int_{-\infty}^{\infty} E_{IR} E_{VIS}(t-\tau)\, dt. \tag{2.1}$$

The cross-correlation is deconvoluted with the width of the femtosecond 800 nm to give the temporal width of the infrared pulse. Figure 2.13 is a cross-correlation of a femtosecond 800 nm and infrared laser pulse. The 800 nm pulse length was measured to be 139 fs using FROG, deconvoluting the cross-correlation gives an infrared pulse width of 191 fs. A second cross-correlation is then carried

out between the femtosecond infrared and picosecond narrowband 800 nm up-conversion pulse.

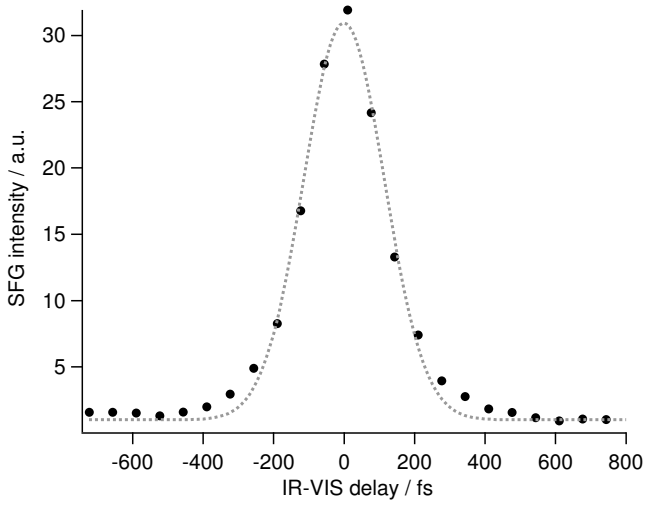

Figure 2.13: Cross-correlation of femtosecond IR and femtosecond 800 nm pulse. The 800 nm pulse width was taken from a FROG measurement to be 139 fs. Deconvoluting the cross-correlation then gives an IR pulse width of 191 fs.

2.4.2 Spatial and Temporal Beam Alignment in UHV

Upon generation of the required pulses needed for the experiment, the beams are delivered to a custom built UHV chamber mounted laser table, see Figure 2.14. It is from here that the final stage of alignment is carried out, the overlapping of two or three laser beams in space (within $\sim$ 300 μm) and time (within $\sim$ 100 fs).

Either of the femtosecond broadband infrared pulses IR1 or IR2 can be used as a SF IR probe or IR pump, with slightly more energy available down the IR2 path due to a more recent professional alignment and installation. The energy of the 800 nm pump is controlled through the use of a half-wave plate (hwp) and polariser cube. The hwp changes the relative ratio of the s and p polarisation in the beam, and then the polariser cube allows transmission of only s or p exclusively.

This allows the energy and polarisation of the pump beam to be varied, while keeping the other parameters constant.

The VIS probe path (800 nm) is attenuated with a neutral density filter when using the femtosecond broadband pulse, or the filter is replaced with a borosilicate glass plate for the frequency resolved, narrowband up-conversion pulse. This is to ensure the correct path lengths and hence time delays between pulses.

All beams are focussed onto the sample by a CaF_2 lens (25 cm focal length) through a MgF_2 chamber window. However, before trying to align the beams directly *in-situ*, they are overlapped outside the chamber down a dummy alignment path. This has a sample position that is equivalent in distance to that in the UHV chamber. Spatial alignment is carried out by focussing the beams through a 300 μm pinhole and using an energy meter.

Temporal alignment is carried out by replacing the pinhole for a non-linear crystal and observing either the second harmonic or sum frequency light generated in the crystal. To generate SF light at 689 nm from 5000 nm IR and 800 nm VIS pulses, a Lithium Iodate ($LiIO_3$) crystal is used (transmission 0.31-5.5 μm). To observe the second harmonic (SH) from two 800 nm pulses at 0.4 μm, a Beta Barium Borate (BBO) crystal is used (transmission 0.21-2.1 μm). It is also possible to observe five-wave mixing (5WM) processes in non-linear crystals, including the infrared-infrared-visible SFG process (IIV SFG), giving orange light at 606 nm (5000 nm IR and 800 nm VIS). To ensure the pulses arrive together in time, the delay stages situated on the main laser table are adjusted to either shorten or lengthen the beam paths. Due to the constant speed of light, lengthening the beam path makes the pulse arrive later in time.

Producing SFG light down the dummy alignment path also gives the direction that the SF or SH light will take upon leaving the surface, $\mathbf{k}_{SF} = \mathbf{k}_{IR} + \mathbf{k}_{VIS}$ and $\mathbf{k}_{SH} = \mathbf{k}_{VIS} + \mathbf{k}_{VIS}$. Hence a HeNe laser is used to trace this path into the UHV

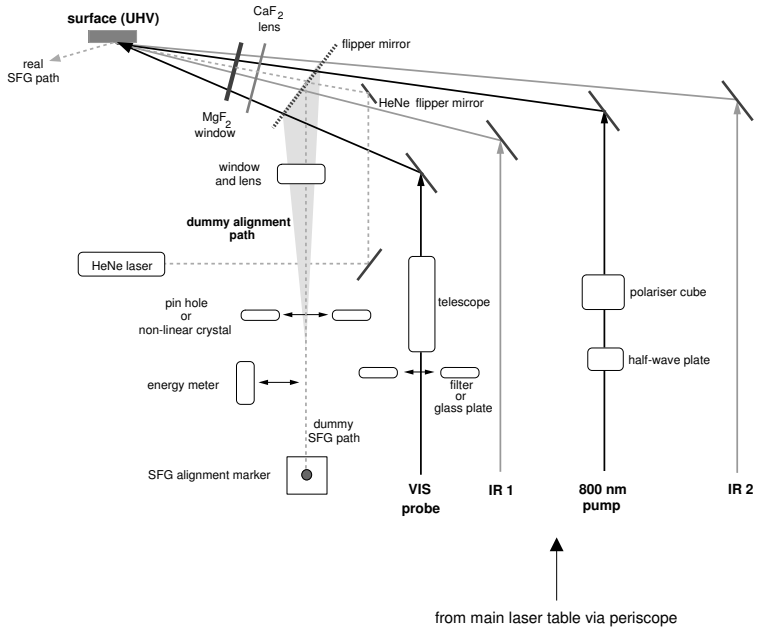

Figure 2.14: Diagram showing the layout of the chamber mounted laser table and beam delivery to sample. Highlighted is the 'dummy' alignment path, which is accessible by a flipper mirror positioned in front of the chamber entrance. The representation of beam delivery angles is not to scale, for reasons of pictorial clarity. IR1 enters the chamber at 65° to the surface normal, VIS probe and 800 nm pump beams at 60°(vertically offset), and IR2 at 63°. The distance from chamber window to sample is 23 cm.

chamber and out towards the spectrograph. This allows the route of the SF light from the surface into the spectrograph to be initially aligned.

At this point the beams are allowed into the chamber and the observation of a non-linear signal from the surface is attempted. The interaction, be it SFG, SHG or a 5WM process is dependent upon the experiment being carried out and the laser pulses involved. The specific details of which, and the alignment procedure

for such experiments is explained in Chapters 3, 4 and 5.

I shall continue with the two beam alignment of a frequency resolved SF probe. The non-resonant signal from the Ir{111} surface is strongly enhanced by evaporating either a monolayer of Cs or K onto the surface [63], this process is central to the alignment process and allows detection of most non-linear (3WM or 5WM) processes from the surface. Initially the VIS probe beam is a femtosecond pulse, with the slit removed from the pulse shaper.

Spatial and temporal overlap of the beams is then carried out on the Cs/Ir{111} surface, by monitoring the SFG light, which has been dispersed by a spectrograph and detected in a gated Intensified Charge Coupled Device (iCCD). The output path from the surface into the slit of the spectrograph is also aligned further at this stage. This path consists of two turning mirrors, a lens and low pass filter to remove scattered 800 nm light, see Figure 2.15.

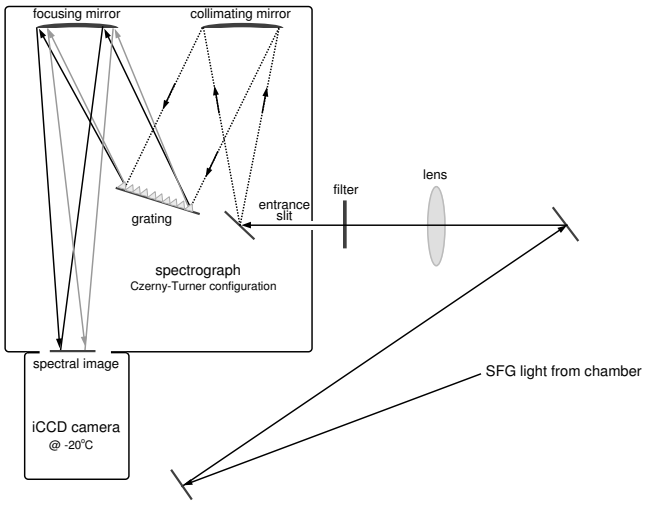

Figure 2.15: Schematic of SFG output from chamber and focusing into the spectrograph, where the SF light is dispersed and imaged on an iCCD camera.

The spectrograph is an Acton SpectraPro 300i, which has an internal path length of 0.3 m, and a choice of low or high resolution gratings (600 and 1800 grooves per mm respectively.) The dispersion produced from the spectrograph is wavelength dependent, but at 691 nm it is equivalent to 0.56 cm^{-1}/pixel on the iCCD for the high resolution grating.

After maximising the signal with a femtosecond VIS pulse, the slit is added to the pulse shaper and the final spatial alignment is made with a picosecond VIS pulse. A spectrum of the Cs/Ir{111} surface is then collected, and a specific horizontal track number of pixels selected on the iCCD to reduce noise. The Cs/Ir{111} spectrum is very important as it reflects the bandwidth of the IR probe pulse and is used in fitting the background non-resonant contribution to SFG spectra of adsorbate/metal systems.

At the end of alignment, which is carried out at a sample temperature of 100 K, the Cs is heated off, requiring a temperature in excess of 1200 K. The Ir{111} crystal is then cleaned in oxygen for a few minutes (5-10 min, $2 \cdot 10^{-7}$ mbar, 1400 K). Upon cooling back to 100 K, the crystal and spectrometer are ready for dosing adsorbates onto the clean surface and collecting SFG spectra. Typical accumulation times for CO/Ir{111} and NO/Ir{111} are 1k and 2k shots respectively (@ 10 Hz).

Chapter 3

Molecular Dynamics

3.1 Introduction

Our ability to tailor surface chemistry towards making or breaking a specific chemical bond during catalysis is substantially improved by a better understanding of the dynamics of molecular motion and reaction. The time scale for a reaction to proceed and rearrange from reactants to products is of the order of a few hundred femtoseconds. While direct detection of nuclear dynamics is now possible with recent development of ultrafast electron diffraction [64], ultrafast vibrational spectroscopy can provide a powerful tool for probing adsorbate dynamics. This investigation aims to try and expand the understanding of the excited state dynamics of two catalytically relevant adsorbates - carbon monoxide and nitric oxide.

3.1.1 Non-adiabatic Dynamics at Surfaces

Central to non-adiabatic dynamics is the concept of separable electronic and nuclear motion, the Born-Oppenheimer approximation. This has proven to be rather naïve, as the incidence of highly vibrationally excited NO upon a surface has been shown to cause emission of hot electrons from the surface [10].

Femtosecond laser spectroscopy has been central in unravelling non-adiabatic vibrational dynamics, since an intense femtosecond pump pulse leaves metal electrons and phonons out of equilibrium for up to a few picoseconds. This means that electron or phonon driven processes can be distinguished by monitoring the coupling times with which the internal stretching mode of an adsorbate responds to ultrafast heating [26–28, 45]. The mechanism of these processes is mediated via coupling with low frequency modes, such as the frustrated translation or rotation.

Time-resolved experiments of this type have been carried out for CO on platinum [28, 45], copper [46, 47] and ruthenium surfaces [26, 27]. At low excitation densities the C-O stretch is found to couple to the frustrated translation. While at higher fluences and under desorption conditions, additional coupling to the frustrated rotation is attributed. The latest application of this approach was used to describe the dynamics of CO diffusion from step to terrace sites on a Pt{531} surface [25].

3.1.2 Femtosecond Heating of Metal Surfaces

Upon excitation with a femtosecond laser pulse the energy is initially transferred to the metal electrons, due to their small heat capacity. Direct excitation of the adsorbate is negligible and hence ignored in the following treatment. The electrons can reach temperatures in excess of 2000 K before relaxing by heat diffusion into the bulk and coupling to the lattice (phonon excitation). This can lead to the electrons and phonons being out of equilibrium for up to a few picoseconds, depending upon the metal properties and laser fluence. The temporal profile of the electron and lattice temperatures (T_{el} and T_{lat}) are modelled using the two-temperature model (Appendix A) and are presented in Figure 3.1. Both the hot electrons and excited phonons can transfer their energy to the adsorbate, on quite different time scales. A classic example of these different pathways is the phonon

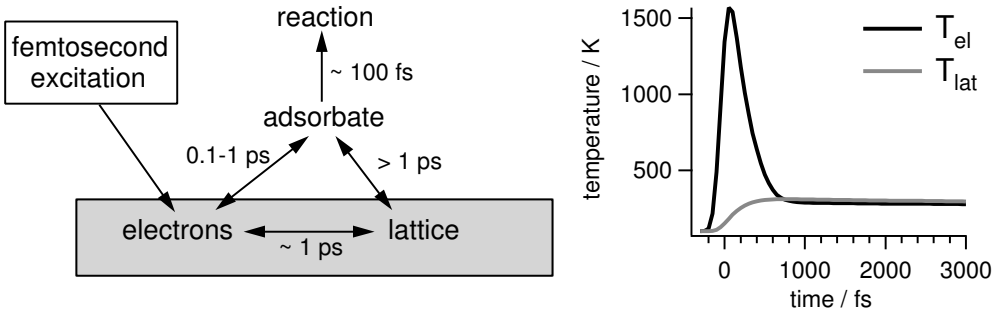

Figure 3.1: Schematic of energy transfer time scales between metal electrons, lattice and adsorbate upon heating with an 800 nm femtosecond laser pulse. The graph to the right hand side shows electron (T_{el}) and lattice (T_{lat}) temperatures, calculated using the two temperature model (see Appendix A). Absorbed fluence is 19 Jm^{-2}.

driven desorption of CO by femtosecond laser pulses, versus the electron driven oxidation of CO on ruthenium [26, 65]. In the present visible pump-SFG study, CO/Ir{111} couples exclusively to phonons, while NO/Ir{111} in addition couples to the electrons via transient population of the NO $2\pi^*$d antibonding orbital by hot metal electrons.

3.1.3 DIMET and Electronic Friction

For an electron mediated process there are two possible ways to treat the mechanism, either the DIMET formalism or the electronic friction model [66, 67]. The DIMET approach (Desorption Induced by Multiple Electronic Transitions), involves the excitation of an electron to a repulsive adsorbate potential energy surface. After a certain excited state lifetime the electron returns via a Frank-Condon transition to the now vibrationally excited ground electronic state. With the intensities generated by femtosecond laser pulses, repeated cycles can equip the

adsorbate with sufficient vibrational energy with which to react or desorb.

The friction model is based upon the tunnelling of electrons from the hot Fermi-Dirac distribution of metal electrons into the $2\pi^*$d orbital of the adsorbate. It is this time-dependent current flowing between the metal and adsorbate that allows for energy transfer, while still on the electronic ground state of the adsorbate [25]. The pathway responsible for this energy transfer is the same as the mechanism for adsorbate vibrational relaxation. For CO and NO adsorbed on a metal surface the $2\pi^*$ molecular orbital broadens into a resonance, which is partially occupied by metal electrons via back-donation. As the molecular bond length changes during the period of a vibration, the centre of this resonance shifts up and down, leading to fluctuating charge transfer (non-adiabatic electron-hole pair creation) and therefore vibrational relaxation [68].

The friction model allows for desktop calculation of adsorbate/hot electron effects, whereas the DIMET formalism requires rather more sophisticated trajectory calculations of the attractive and repulsive potential energy surfaces involved.

3.1.4 Surface Science of NO and CO on Ir{111}

The adsorption of NO on metal surfaces is of considerable scientific and technological interest. Although CO has done a sterling job as surface science's foremost probe, the surface chemistry of NO currently holds more interest for the scientific community. A particular example of this is the very important catalytic reduction of NO_x species to N_2 and O_2 in the modern day three way exhaust catalyst [69,70].

The dissociation energy of NO in the gas phase is 630 kJmol^{-1}, much lower than CO (1076 kJmol^{-1}), which is largely due to an extra electron populating the NO $2\pi^*$ antibonding orbital. This helps to generate a much greater range of molecular and dissociative adsorption on metal surfaces when compared to CO [71]. It is therefore of little surprise that NO undergoes both molecular and

dissociative adsorption on Ir{111}.

CO adsorption on Ir{111} has been investigated by SFG, RAIRS and LEED [35, 59, 72]. Only atop sites are occupied, with a locally accessible saturation coverage of 0.58 ML, giving a $(2\sqrt{3}\times 2\sqrt{3})$R30° structure, see Chapter 4. At 0.58 ML a single peak is observed in both SFG and RAIRS at 2080 cm^{-1}, relatively close to the gas phase value of 2143 cm^{-1}.

The vibrational properties of NO on Ir{111} have been studied by EELS [73, 74]. At low coverages, only atop sites at a frequency of 1860 cm^{-1} are detected, while at the saturation coverage of 0.5 ML p(2 × 2) [75], half the molecules reside in bridge or hollow sites with two characteristic frequencies around 1440 cm^{-1} and 1550 cm^{-1}. On heating a saturated layer, the bridge/hollow sites initially desorb and the atop molecules desorb as well as dissociate.

3.2 Experimental

For these experiments the CO/Ir{111} or NO/Ir{111} system is perturbed by a visible femtosecond pump pulse and then probed at a given delay by a frequency resolved SFG probe. All the laser pulses (pump/probe-IR/probe-vis) originate from the output of the regeneratively amplified Ti:sapphire system, delivering 140 fs pulses at 7 mJ of energy per pulse, see Chapter 2. 2.5 mJ of this is used to pump an OPA to generate the mid-IR probe pulse and 2 mJ is passed through a pulse-shaper to produce narrow-band visible pulses for SFG upconversion. The remaining 2.5 mJ is used to generate the pump pulse.

Most of the work is carried out with a variable energy/polarisation pump pulse at 800 nm, direct from the output of the regenerative amplifier. Pump fluence is changed by adjusting a half wave plate and polarisation cube and measured using a pyroelectric energy meter. To generate pump pulses of lower photon energy, either

the 800 nm is frequency doubled in a BBO non-linear crystal, or the 800 nm is used to pump a second OPA and either the signal or idler output can be used as a pump pulse. The IR beam enters the chamber at 65° to the surface normal, the 800 nm upconversion beam and the pump beam at 60°. The 800 nm pump beam spot is about three times larger than the visible probe pulse, ensuring that only the central region of the pump spot is probed.

Due to the severely reduced signal from bridge and hollow sites for SFG, the lower frequency species are not detected and only the atop molecules are probed [76]. All the results presented here were conducted on saturated NO (0.5 ML) and CO (0.58 ML) layers to ensure long-term stability during pump-probe experiments. Gases were dosed via background dosing at 100 K and then flashed to 250 K, to ensure good surface order. Saturation dosage for NO and CO was 20 and 10 L respectively. All experiments were carried out at 100 K.

3.2.1 Novel Alignment Procedure for 800 nm Pump Pulse

Spatial and temporal overlap of the pump and probe pulses is achieved by monitoring the non-resonant SF probe signal from a caesium multilayer, see [63]. The first stage consists of a coarse alignment between the pump and probe 800 nm beams, by monitoring the second harmonic signal from Cs/Ir at 400 nm. The spectrograph input mirrors are then realigned for the probe SF path. At this point it was discovered that for pump pulses in excess of 10 Jm^{-2}, the Cs/Ir signal is significantly reduced by up to 40 %.

Figure 3.2 shows the reduction in Cs/Ir SF signal as a function of 800 nm pump-SF probe delay. Displayed in the inset are the corresponding metal electron and lattice temperatures (T_{el} and T_{lat}), calculated using the two-temperature model, see Appendix A. The probe is a femtosecond IR and VIS pulse pair, as no frequency resolution is needed to probe the non-resonant Cs/Ir signal. Although it

is not clear what mechanism is exactly responsible for reducing the SF intensity, its temporal profile closely follows the hot electron temperature. The grey line in Figure 3.2 is the scaled electron temperature convoluted with the 200 fs temporal pulse width of the fs SFG probe pair.

After the Cs/Ir signal was maximally reduced with the fs SFG probe pair (spatial and temporal alignment), the slit was inserted into the pulse shaper and final spatial alignment carried out. The overlap achieved using this minimisation routine proved to be excellent and lasted for many hours and sometimes days.

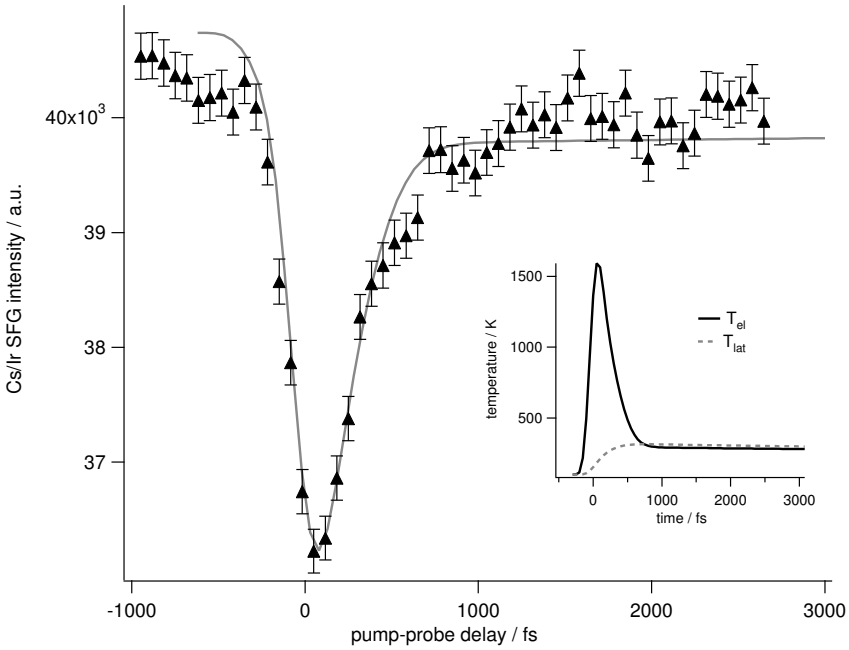

Figure 3.2: Non-resonant Cs/Ir SFG intensity as a function of 800 nm pump-probe delay. The pump fluence was 20 Jm^{-2}. The temporal profile of the grey line is modelled by convoluting the electron temperature with the 200 fs pulse width of the SFG probe pair. The inset gives the corresponding electron and lattice temperatures (T_{el} and T_{lat}) calculated using the two-temperature model.

3.2.2 Fitting Spectra

The non-resonant Cs/Ir{111} signal in the N-O infrared region shows absorption lines from water in the air. One of these is fairly close to the NO resonance, and partly overlaps it when the NO peak is red-shifted during pump-probe spectroscopy. In order to account for atmospheric absorption in this region of the mid-IR, the spectra are divided by the nonresonant Cs/Ir{111} spectrum. This allows the simulation of constant IR intensity over the whole frequency range.

The measured SF signal is proportional to $|\chi^{(2)}|^2$, the second order non-linear susceptibility. $\chi^{(2)}$ is composed of a non-resonant $\chi^{(2)}_{NR}$ and resonant $\chi^{(2)}_{RES}$ contribution. The resonant contribution is given by a Voigt function, to allow for the spectral width of the visible upconversion pulse. The non-resonant contribution for NO was a spectrally flat background (due to previous background division) and for CO a Cs/Ir{111} SF spectra was used. The spectral width of the visible upconversion pulse (which is needed for the Voigt fitting) was measured by cross-correlation with the femtosecond infrared pulse on a Cs/Ir{111} surface.

3.3 Results

3.3.1 SFG of CO and NO on Ir{111}

Figure 3.3 shows the SF spectra of 0.5 ML NO/Ir{111} and 0.58 ML CO/Ir{111} at 100 K. Both spectra are plotted on a common y-axis, hence showing the larger SF signal of CO on surfaces compared to NO. This makes collecting quality NO SF spectra a more time intensive process, and hence more open to long term fluctuations in laser stability and surface contamination. The difference in signal size is due to the larger dynamic dipole moment (IR cross section) of CO over NO. Although NO does have a larger hyperpolarisability (Raman cross section), it seems

to play less of a part in determining SF signal size. In fact the difference in signal size can be larger than displayed, the largest CO signal measured exceeded a count per shot, nearly three times that plotted. The grey dashed lines in Figure 3.3 are the Cs/Ir{111} SF spectra at the same probe wavelengths, showing the envelope of the IR-probe pulses. The atmospheric absorption lines in the NO background can be clearly seen in comparison to the CO background, hence the need to divide the NO spectra by the background, as described in section 3.2.2. Upon fitting both CO and NO SF spectra, typical peak widths as defined by the full width at half maximum (FWHM) are 5-8 cm^{-1}.

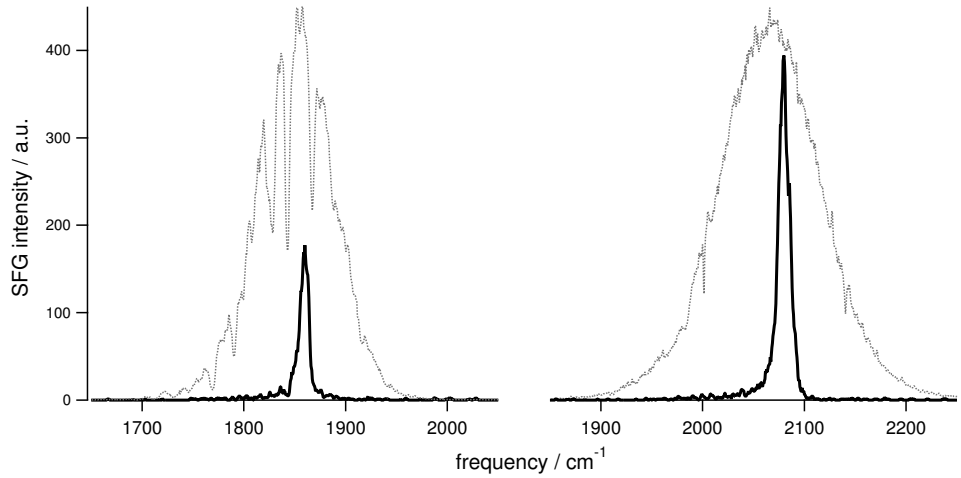

Figure 3.3: 0.5 ML NO and 0.58 ML CO SF spectra accumulated over 1000 laser shots. Grey dashed lines are normalised Cs/Ir{111} SFG spectra at OPA wavelengths of 5350 nm and 4700 nm respectively. The envelope of the IR-probe pulse is given by these spectra.

Static Temperature Dependence

The first experiment carried out was to see how the CO and NO SF peaks changed upon slow static heating, using the heating wires attached to the back of the crystal. The respective changes in peak centre frequency and width are shown in Figure 3.4. The CO spectra were acquired at fixed temperatures during sequential heating steps, while the NO spectra were recorded during an 8 $Kmin^{-1}$ ramp of the sample from 100 K to 290 K and back down. The frequency shows a strong red shift of -5 and -10 cm^{-1} for CO and NO respectively from 100 K to 290 K, while the peak widths increase for both molecules by just under 4 cm^{-1}. Up to 300 K the changes are observed to be reversible, showing no signs of hysteresis.

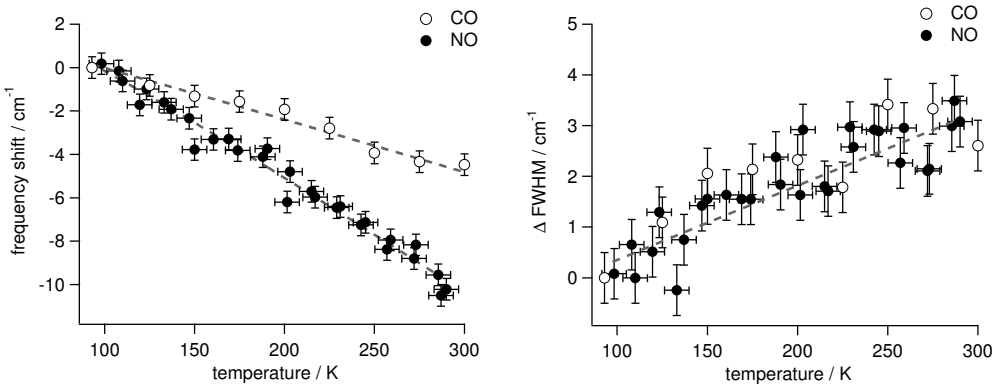

Figure 3.4: Static temperature dependence of the frequency and linewidth of CO and NO. The dashed lines correspond to linear fits for the frequency and linewidth. The gradients are used later in section 3.4 to fit the temporally resolved data.

The red shift can be explained by coupling of the intramolecular stretching mode to the frustrated translation or rotation [77]. Values for the low frequency modes of CO/Ir{111} and NO/Ir{111} are not known, but are largely dependent on bonding site and less on the specific transition metal. Typical frequencies for the frustrated translation and rotation are of the order of 50-100 cm^{-1} and

400-500 cm^{-1}, respectively. Considering that the thermal energy at 300 K is equivalent to an energy of 210 cm^{-1}, this makes population of the frustrated translation relatively easy at low temperatures. On Rh{111}, atop bonded NO in a p(2×2) layer has a frustrated translational frequency of 59 cm^{-1}, while CO has a frequency of 44 cm^{-1} in the ($\sqrt{3} \times \sqrt{3}$) structure [78].

3.3.2 Time Resolved Spectroscopy

The results presented in the following section are from vis-pump SFG-probe experiments. The data is initially plotted as a function of pump-probe delay (τ) to produce a series of pump-probe transients, these plot an experimental observation versus pump-probe delay and each data point corresponds to an individual spectrum at fixed delay. The shape and size of the pump probe transients gives powerful information about how the molecules at the surface respond to ultrafast heating with a femtosecond pump pulse. Figure 3.5 shows the changes to the N-O and C-O stretch frequency and linewidth as a function of pump-probe delay time for an 800 nm pump pulse. The shape of the transients are very different for CO and NO. CO shows a slow and gradual return to normal, over a time scale of ~100 ps. The maximum observed effects are a frequency shift to the red by ~4 cm^{-1} and the FWHM increasing by ~3 cm^{-1}. NO shows a very fast change within ±2 ps of zero time delay and a slower recovery on a time scale of tens of picoseconds. The frequency shifts to the red by ~12 cm^{-1} and the FWHM increases by nearly 14 cm^{-1}. The two time scales which NO exhibits are similar to the distinct electron and lattice temperatures observed after femtosecond laser heating.

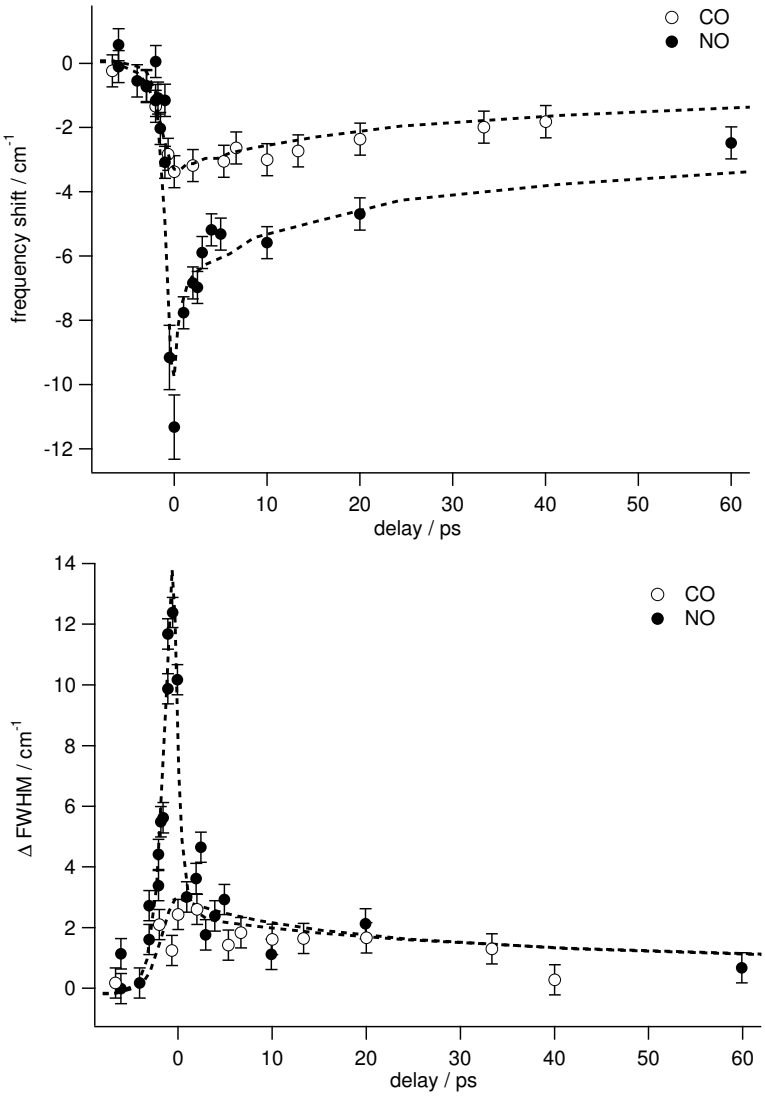

Figure 3.5: Time dependent changes in the frequency and FWHM of 0.5 ML NO/Ir{111} and 0.58 ML CO/Ir{111} as a function of pump-probe delay. Pump pulse is at 800 nm with an absorbed fluence of 12 Jm^{-2}. The dashed lines are given by the model described in section 3.4.

Fluence Dependence

The temporal profile of the CO transients is found to show no real fluence dependence, with all the transients sharing the same curved profile that follows the

lattice temperature. However, the temporal profile of the NO transients does show a strong fluence dependence. Figure 3.6 demonstrates that the magnitude of the fast change increases strongly with pump fluence. At low fluence, the N-O frequency follows the phonon temperature, while at higher fluences, pronounced perturbation of the N-O is observed on a time scale similar to the hot metal electron temperature. Following the observation of a strong fluence dependence for

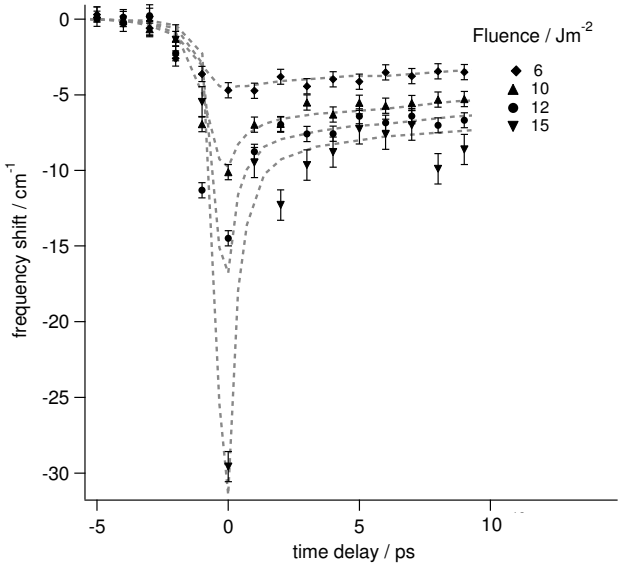

Figure 3.6: Fluence dependent pump-probe transients of 0.5 ML NO/Ir{111}. The frequency shift of the N-O bond is plotted for 6,10,12 and 15 Jm^{-2} absorbed fluence. At 15 Jm^{-2} desorption is observed and the coverage is kept constant with a backing pressure of $2{\cdot}10^{-7}$ mbar.

NO, a more exhaustive fluence study was carried out. Two pump probe delays were picked that identify the fluence dependent behaviour of the two different time scales observed in the NO transients. The fast change around zero delay is defined as electronic, and the slow decay of tens of picoseconds is defined as the thermal time scale. A time delay of zero picoseconds was assigned to the electronic component and a delay of + 15 ps as representative of the thermal component. The

corresponding changes in frequency and linewidth, as a function of pump fluence for both CO and NO are shown in Figures 3.7 and 3.8. The non-linearity for NO of the electronic component compared to the thermal region can be clearly seen in Figure 3.7, showing a distinct increase in slope above an absorbed fluence of 10 Jm^{-2}. This becomes particularly clear when compared to the linear profiles for both electronic and thermal components for CO in Figure 3.8.

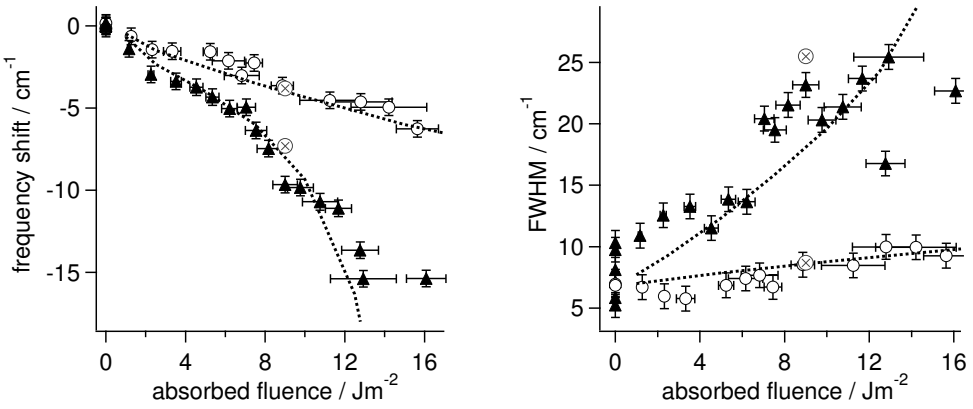

Figure 3.7: Fluence dependence of frequency shift and linewidth at t = 0 (filled triangles) and t = 15 ps (open circles) for NO/Ir{111}. Dashed lines are given by model in section 3.4. Large crossed symbols are data recorded at 9 Jm^{-2} with an 1396 nm pump beam.

Pump Wavelength and Polarisation Dependence

The photon energy of the pump beam was varied and pump-probe spectra recorded, pump photon energies of 0.77, 0.89 and 3.1 eV were used. These refer to the s-polarised signal beam at 1590 and 1396 nm and the p-polarised second harmonic of the 800 nm, respectively. These alternate pump beams were generated using various non-linear processes either in the OPA or on the laser table with a

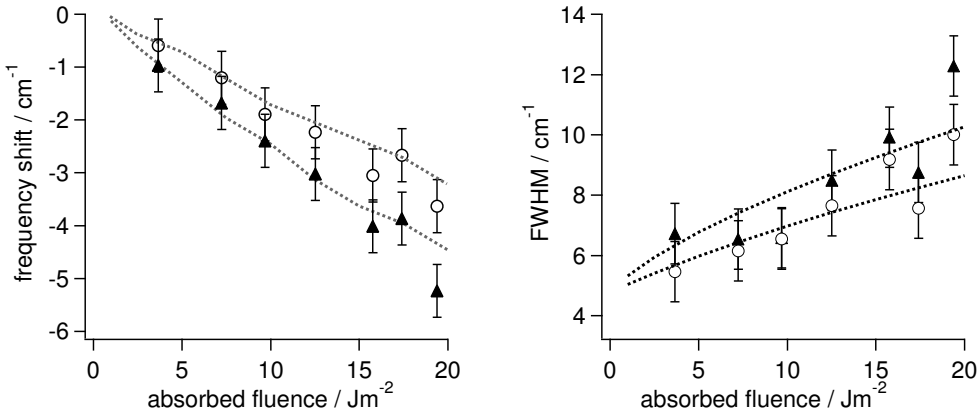

Figure 3.8: Fluence dependence of frequency shift and linewidth at t = 0 (filled triangles) and t = 15 ps (open circles) for CO/Ir{111}. Dashed lines are given by model described in section 3.4.

BBO crystal, hence all had different beam sizes and divergences. The different polarisations also affect the reflectivity, it is ~0.5 for s-polarised light as opposed to 0.9 for p-polarised (wavelength dependent). Taking these factors into account, no quantitative difference to the 1.55 eV pump data was observed, within the uncertainty of the pump fluence. Data points for 1396 nm pump are included in the fluence dependence shown in Figure 3.7.

As a final experiment, an s-polarised 800 nm pump pulse was used, this showed no observable difference to a p-polarised pump of similar absorbed fluence. The experiments presented in section 3.3.2 suggest that the observation of fast transient effects is only dependent upon the absorbed intensity of the pump pulse and not on its polarisation or photon energy.

Probe Polarisation Dependence

It is possible to determine the orientation of molecules adsorbed on surfaces by measuring the SF signal strength as a function of polarisation, as demonstrated for CO on Pd{111} [16]. This is achieved by measuring the SF intensity ratio I_{SSP}/I_{PPP}, as discussed in section 1.2.3. The subscripts refer to the polarisation of the electric fields of the SFG, visible and IR fields, relative to the surface (either *s* or *p*.) For a standard SFG experiment on metal surfaces, a PPP polarisation configuration is used to maximise the SFG signal. For an SSP configuration an *s*-polarised visible upconversion pulse is used and only the *s*-polarised SFG is measured.

P-polarised light has an electric field component perpendicular to the surface (z) and in one of the surface plane directions (eg. x), while *s*-polarised light has an electric field component in only one direction (eg. y). Hence, for the polarisation combination PPP, the χ_{zzz} and χ_{xxz} elements of the nonlinear susceptibility tensor will contribute to the measured SFG signal, as discussed in section 1.2.3. In the SSP configuration, only the χ_{yyz} component will contribute to the SFG signal. Therefore the observation of an SSP SFG signal means that the molecule generates polarisation in a direction parallel to the surface, suggesting it is tilted.

For molecules like NO ($C_{\infty v}$ symmetry), the ratio I_{SSP}/I_{PPP} depends on the orientation of the adsorbate relative to the surface, the optical properties of the NO layer given by the Fresnel matrix elements, and the molecular hyperpolarisability ratio β_{aac}/β_{ccc}. This means that if β_{aac} is not negligible, the observation of an SSP signal does not necessarily mean that the molecule is tilted.

The SFG intensity ratio I_{SSP}/I_{PPP} for NO on Ir{111}is approximately 0.03, independent of the surface temperature between 100 K to 300 K. Although the SSP signal is expected to be low, the extremely small magnitude of the SSP signal makes it far too difficult to distinguish a reliable change in the I_{SSP}/I_{PPP} ratio for

pump-probe experiments.

A meaningful evaluation of the data is hampered by uncertainty in both the optical properties and β_{aac}/β_{ccc}. Firstly, the reflectivity of the interface can change by a few percent as a result of the pump beam [79], which in turn modifies I_{SSP}/I_{PPP}. Pump-probe reflectivity data would be needed to quantify this effect. Secondly, the hyperpolarisability ratio β_{aac}/β_{ccc} will increase if the $2\pi^*$ occupation increases [80], as moving electron density away from the central bond axis leads to a more spherical polarisability and hence larger β_{aac}. These factors significantly reduce the ability to determine geometrical changes from the polarisation dependence.

3.4 Modelling and Theory

The new model introduced herein is based on the electronic friction framework and naturally incorporates the temporal and fluence dependent changes observed. For CO and NO on transition metals, the bonding is dominated by mixed adsorbate-metal states with 5σd and $2\pi^*$d character. The central premise of this modelling is that hot electrons generated from a femtosecond laser pulse can lead to a transient increase in the occupation of the $2\pi^*$d orbital, and hence change the electronic structure and geometry of the adsorbate.

The increased backdonation caused by femtosecond laser excitation was first described by Brandbyge *et al.* in terms of electronic friction [66]. They proposed that direct energy transfer between the metal electrons and adsorbate motion occurs via charge transfer to the adsorbate $2\pi^*$d resonance. In traditional metal nitrosyl chemistry this charge transfer leads to a bent MNO group [81] and pronounced red-shift of the N-O frequency [82]. The addition of an extra electron into the $2\pi^*$ orbital reduces the N-O frequency by 500 cm^{-1}. For nitrosyl complexes of the

form $\{ML_5NO\}^n$, where n is the number d electrons, the MNO group is linear when $n \leqslant 6$ and bent when $n \geqslant 7$ [83].

On a transition metal surface, bending NO from an atop site involves a change from upright bonding, where the dominant participant orbitals are the metal d_{z^2} and NO 5σ, to a bent configuration with additional NO $2\pi^*$ character. This increases the backdonation from the metal to the adsorbate and hence causes a red shift of the internal adsorbate stretch.

The pertinent point for the differing behaviour of the NO/Ir{111} and CO/Ir{111} systems, is the height of the adsorbate $2\pi^*$d anti-bonding orbital above the Fermi level. For CO the $2\pi^*$d anti-bonding orbital is ~3 eV above the Fermi level and relatively inaccessible to hot electrons, whereas the NO $2\pi^*$d anti-bonding orbital is only 1.5 eV above E_F, and hence accessible to hot electrons. Figure 3.9 shows a schematic diagram of a hot Fermi-Dirac distribution n_f and its overlap with a Gaussian adsorbate orbital Π_{ads}. The overlap integral depends strongly on the electron temperature and the position of the adsorbate level, hence the strong fluence dependence observed. The $2\pi^*$d$\rightarrow E_F$ separation for NO has been measured by inverse photoemission on a number of transition metal surfaces [84–86] and predicted by theory for the Ir{111} surface [87]. To model the pump-probe spectra the overlap between the metal hot Fermi distribution and the adsorbate $2\pi^*$d is used to predict the frequency shift.

The details of the full modelling are as follows. The adsorbate frequency shift is composed of two components: A thermal component ν_{lat}, which derives from electrons and lattice being in equilibrium and an electronic component ν_{el}, which derives from the thermalised hot electrons:

$$\nu(t) = \nu_{lat}(t) + \nu_{el}(t). \tag{3.1}$$

The thermal component ν_{lat} is calculated using the statically measured linear tem-

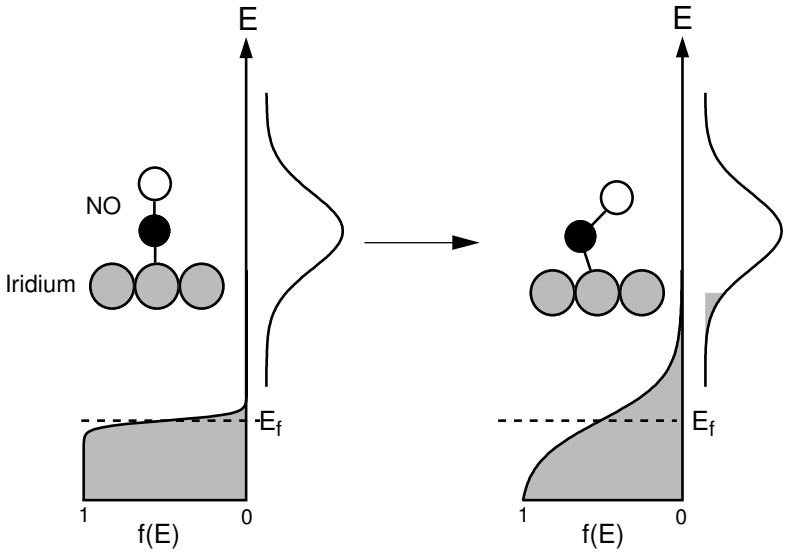

Figure 3.9: A schematic diagram showing the thermalised hot Fermi-Dirac electron distribution after excitation with a femtosecond optical pulse. The greater density of hot electrons can populate the adsorbate $2\pi^*$d, causing bending of the NO molecule.

perature dependence (see Figure 3.4) with gradient ξ and frequency ω_0 at 100 K:

$$\nu_{lat}(t) = \omega_0 - (T_{lat}(t) - 100\,\mathrm{K}) \cdot \xi. \tag{3.2}$$

The electronic contribution is driven by the magnitude of overlap between the Fermi distribution and the adsorbate orbital, A(T_{el}). This overlap increases with electron temperature as shown in Figure 3.9 and the adsorbate frequency responds to this within a time τ_{el}. This is the time it takes for the NO to bend in response to increased population of the $2\pi^*$d orbital. τ_{el} can be thought of as the non-adiabaticity of the system. The faster the response time, the greater the degree of non-adiabaticity.

$$\frac{d\nu_{el}(t)}{dt} = -A(T_{el}) + \frac{1}{\tau_{el}} \cdot \nu_{el}(t) \tag{3.3}$$

$$A(T_{el}) = \beta \cdot \int_{-\infty}^{\infty} n_f(\epsilon, T_{el}) \Pi_{ads}(\epsilon)\, d\epsilon, \tag{3.4}$$

where β converts the degree of overlap into a frequency shift. This conversion factor depends on how many electrons are available ($N(E_f) \sim 1$ e$^-$/atom/eV) [88], the time scale of electron arrival ($t_r \sim 10^{-13}$ s) and the relationship between $2\pi^*$d occupancy and wavenumber ($\varpi \sim 500$ cm^{-1}/e$^-$) [82].

$$\beta = \frac{N(E_f)\varpi}{t_r} = 5 \cdot 10^{18} \text{ cm}^{-1}\text{s}^{-1}, \tag{3.5}$$

where $\epsilon = E - E_f$ is the energy with respect to the Fermi energy E_f and the adsorbate orbital is taken as a Gaussian centred at ϵ_a with a width Γ. The parameters varied are the FWHM of the $2\pi^*$d orbital, β and τ_{el}.

Together with the frequency changes, the instantaneous linewidth changes are also modelled using the sum of a thermal component Γ_{lat} and an electronic component Γ_{el}. Γ_{lat} is taken from the extrapolated static temperature dependence of the linewidth as measured in Figure 3.4. Γ_{el} is an empirical term that couples the instantaneous linewidth change to the difference between electron and lattice temperature $T_{el} - T_{lat}$, with the same time constant τ_{el} and a linear gradient. Unfortunately there is no a-priori way to quantitatively predict the electronic component of the linewidth, but the observed increase does fit qualitatively within the electronic friction framework. Tully *et al.* explain the short vibrational lifetime of the internal bond of the adsorbate by charge transfer during an oscillation of the N-O bond. Bending of NO moves the molecule's centre of mass closer to the surface, thereby increasing this contribution [68].

The instantaneous frequency $\nu(t)$ and width $\Gamma(t)$ are then used as an input to the optical Bloch equations, which turn the instantaneous changes into the corresponding observed spectra, see Appendix A for details [27]. This calculation takes into account the fact that fast changes in frequency or linewidth are averaged out via upconversion over the entire free induction decay of the molecule (~2 ps). The shape and size of the modelled transients, as a function of electron coupling time τ_{el} and the height of the $2\pi^*$d orbital above the Fermi level are presented in

Figure 3.10. It can be clearly seen in Figure 3.10 part (a), that as the coupling time τ_{el} is reduced below the T_2 time of 1.5 ps, the magnitude of the frequency shift is reduced. The CO transients can be fitted using only the thermal component $\nu_{lat}(t)$ from equation 3.1. This means that the C-O stretch is only perturbed by coupling to the frustrated translation, which is thermally populated via the lattice phonons. However, the NO transients also require an electronic component due to

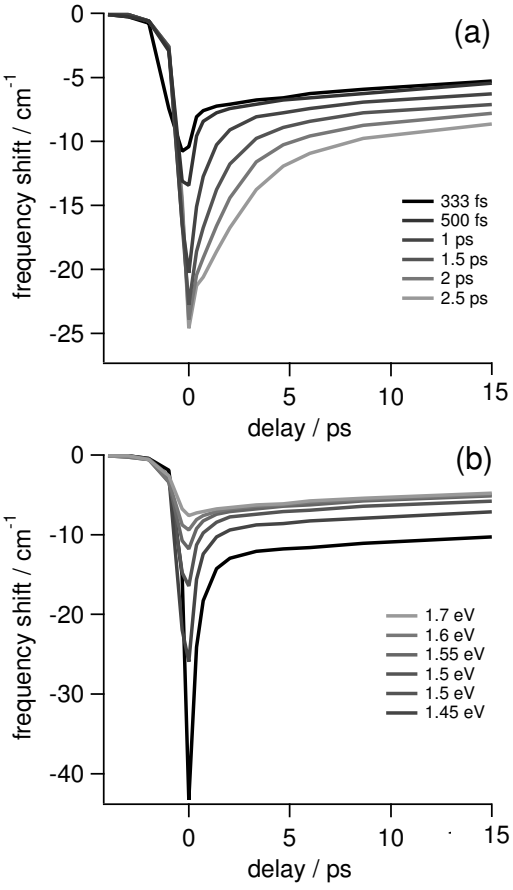

Figure 3.10: Plot showing calculated frequency shifts as a function of model parameters. (a) Electron coupling time from 330 fs to 2.5 ps. (b) Height of NO $2\pi^*$d orbital above Fermi level, 1.45 eV to 1.7 eV. The orbital width Γ = 0.7 eV, adsorbed fluence = 12 Jm^{-2} and T_2 = 1.5 ps were kept constant.

thermally induced electron excitation into an orbital 1.5 eV above the Fermi level with a FWHM of 0.7 eV. β was kept constant at a value of $8 \cdot 10^{16}\,\mathrm{cm^{-1}s^{-1}}$. The coupling time of the N-O stretch to this process was 670 fs.

3.4.1 DFT

Density Functional Theory (DFT) calculations were carried out on my behalf by Dr Zhipan Liu[1], to investigate the properties of bent NO adsorbed on Ir{111}. DFT is a quantum mechanical method used to investigate the electronic structure of many-body systems. The technique can calculate the energy and electronic structure of any arrangement of atoms from first principles, providing information about the physical and chemical properties of representative model systems. At this point the quantum mechanical information provided by DFT can be interpreted to try and provide insight into the dynamics observed in experiment. A full explanation of DFT is far beyond the scope of this thesis, however technical details of the calculations are provided for reference.

Total energy calculations using the DFT-slab approach with GGA-PW91 functional were performed. The program used was CASTEP. The Ir{111} surface was modelled by a four-layer slab with top layer relaxed. x and y are coordinates within the surface layer. To mimic the effect a bending of the Ir-N-O group would have on the N-O stretch frequency, the y coordinate of the oxygen atom is fixed at various positions, while all other parameters are allowed to relax. The energy of this bent NO with respect to the relaxed state (NO upright) is calculated, as well as the optimised Ir-N-O angle and the frequency of the NO group (Figure 3.11).

The equilibrated adsorption state of atop NO in a p(2x2) layer at saturation coverage (0.5 ML) has an Ir-N-O angle of 178°, an NO distance of 1.176 Å and a

[1]Shanghai Key Laboratory of Molecular Catalysis and Innovative Materials, Department of Chemistry, Fudan University, Shanghai, 200433, People's Republic of China

stretching frequency of 1915 cm^{-1}. At an Ir-N-O angle of 162°, the N-O distance increases to 1.180 Å, the frequency drops by 54 cm^{-1} to 1861 cm^{-1} and the total energy of the system increases by $\Delta E = 0.12$ eV.

As the molecule bends, the N atom shifts away from the atop position, so the N-Ir bond lengthens at the same time as the N-O bond, as shown in Figure 3.11. Bending therefore weakens both bonds. At the largest angle, the calculated N-O frequency has dropped by 54 cm^{-1}. This fits very well with the larger shifts observed experimentally, given that the SFG process integrates fast changes over the inverse linewidth, thus reducing the magnitude of fast changes in frequency and linewidth [89].

In addition to the geometry and frequency changes associated with bending, a calculation was also performed to see how the occupancy of the NO $2\pi^*$d changed upon bending. The NO $2\pi^*$d orbital gained nearly 0.03 e^- upon bending to the largest angle, confirming the link between NO $2\pi^*$d occupancy and the Ir-N-O angle. This value compares to an electron occupancy change of 0.02 e^-, as taken from nitrosyl chemistry.

3.5 Discussion

The discussion shall be split into four main sections. Section 3.5.1 shall give a brief overview of the experimental results and explain the basic concepts of the modelling applied. Section 3.5.2 shall address whether the pump-probe transients could have been fitted using existing models, and why it was felt that these were unsatisfactory. Section 3.5.3 shall look at whether nascent electrons could play a role in the observed effects, and finally section 3.5.4 shall look at the implications of these experiments and discuss what can be learned about surface dynamics.

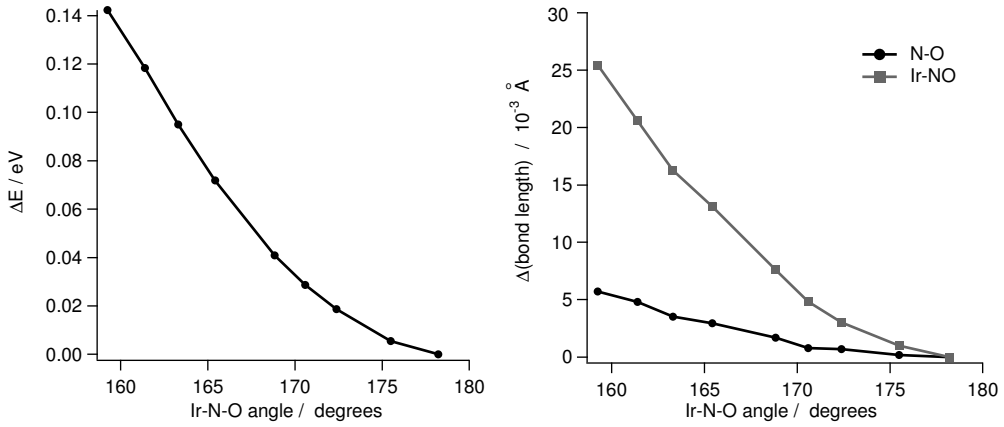

Figure 3.11: Change in energy and Ir-NO and N-O bond lengths as a function of Ir-N-O angle, as calculated by DFT (Dr Zhipan Liu).

3.5.1 Experiments and Modelling Review

Upon ultrafast heating with a femtosecond laser pulse, the N-O bond frequency and linewidth change on two time scales, one is fast and similar to an electronic time scale, the second is slower and thermal in nature. The C-O bond frequency and linewidth under similar excitation conditions is observed to only show a thermal response over the longer time scale. For a comparison of the two pump-probe transients see Figure 3.5. It is also observed that the magnitude of the fast changes in the N-O frequency and linewidth depends nonlinearly on fluence, see Figure 3.6. This is in comparison to the purely linear changes observed as a function of fluence for the C-O frequency and linewidth, see Figure 3.8. The time-dependent and fluence-dependent data suggest that adsorbed NO on Ir{111} couples strongly to the metal electrons upon ultrafast heating, whereas CO does not.

The experimental observations have been theoretically modelled using a new

approach, central to this is the ability to model fast transient features in the pump-probe spectra for NO. This theory is based upon the effects of a transient increase in the occupation of the NO $2\pi^*$d orbital by metal hot electrons. For NO the charge transfer from hot electrons to the NO $2\pi^*$d orbital leads to weakening of the internal bond and a bending of the M-N-O bond. The response of the nuclear motion to the hot electron distribution occurs on a time scale of 670 fs. The electronic effect cannot be seen for CO, because the CO $2\pi^*$d orbital is too far above the Fermi level to be efficiently populated by hot electrons at transient temperatures below 2000 K. In addition to the fast changes a slow thermal response was observed for both adsorbates, due to coupling of the molecular stretch with a low frequency mode. This is exactly the same mechanism as that responsible for the static temperature dependence of the SFG peak frequency and linewidth, Figure 3.4.

3.5.2 Previous Approaches to Modelling

Modelling of similar pump-probe spectra has often been based around the two-temperature model of laser heating at metal surfaces, this describes the equilibrium between electron (T_{el}) and phonon temperature (T_{lat}) [45]. The intermolecular bond of the adsorbate is then assumed to couple to a third heat bath, called the adsorbate temperature (T_{ads}). The adsorbate heat bath couples to the electrons and phonons with coupling times of τ_{el} and τ_{lat} respectively. The temporal profile of an adsorbate heat bath that couples to both the electrons and phonons, with coupling times of τ_{el} = 1 ps and τ_{lat} =1 ps is shown in Figure 3.12. The transient frequency change is then assumed to have the same origin as the commonly observed red-shift with increasing surface temperature, except that the adsorbate temperature is used rather than the surface temperature. This has been explained by anharmonic coupling of the high frequency stretch with a low frequency mode, like the

frustrated translation at $\sim 60\ \mathrm{cm}^{-1}$. This approach would work perfectly well for describing the CO transients, where the adsorbate temperature would only couple to the phonon temperature. However, to generate fast changes as seen in the NO

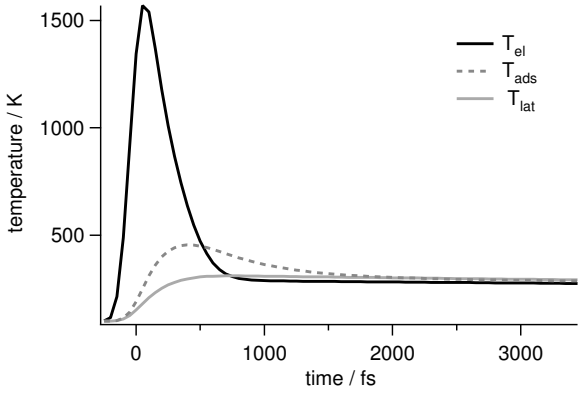

Figure 3.12: Lattice (T_{lat}) and electron temperatures (T_{el}) at an iridium metal surface after excitation with a femtosecond laser pulse. Also included is an adsorbate temperature, which was generated by coupling to the lattice and phonons with a coupling time of 1 ps.

transients, the adsorbate temperature must either be coupled to the hot electrons via the frustrated translation (where $\tau_{el} \sim 1 - 2$ ps), or be coupled to the metal electrons in addition via a second mode, such as the frustrated rotation [25, 28]. An attempt was made to try and model the NO transients using the assumption of a third adsorbate heat bath and the two coupling schemes described above. But regardless of whether the frustrated translation or rotation was used as the coupling mode, it was not possible to fit all the transients well with a *constant* electron coupling time, τ_{el}. In order to force the model to fit the transients, the rate at which the low frequency mode couples to the electron temperature would have to increase nearly ten fold as the higher fluences were reached. While this phenomenological approach does rightfully establish the importance of low-frequency modes, it does not provide a solution that leads to a meaningful physical interpretation of

the experimental results.

3.5.3 Nascent Electronic Effects

The photon energy of the 800 nm pump is 1.55 eV, which is near-resonant with the height of the NO $2\pi^*$d orbital above the Fermi level. It is therefore important to consider if the observed fast transients are due to resonant excitation of metal electrons directly into the NO $2\pi^*$d orbital. These non-thermalised electrons have not equilibrated their energy with other electrons in the metal and are often referred to as nascent electrons, see Figure 3.13.

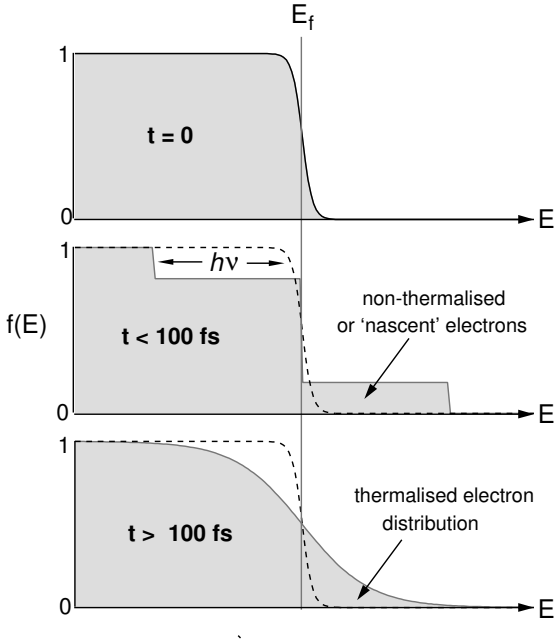

Figure 3.13: A schematic diagram showing the changes to a metal Fermi-Dirac electron distribution after excitation with a femtosecond laser pulse of photon energy $h\nu$. The short lived nascent distribution will undergo thermalisation via electron-electron scattering. At the fluences used in this experiment nascent electrons should equilibrate within 100 fs [90].

There are two reasons to discount any large effects originating from nascent electrons. The first is that no quantitative difference was observed for the transients produced at different pump energies in section 3.3.2. The second reason is that very fast effects, such as direct electronic excitation would give modulations in the pump-probe spectra at negative delays.

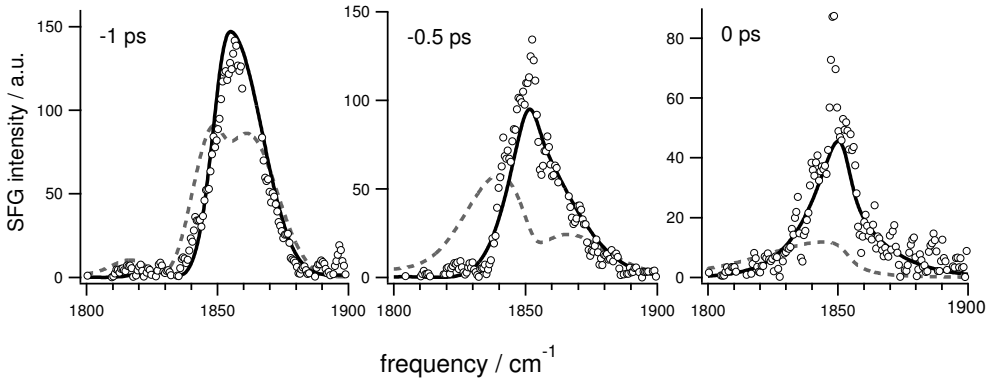

Figure 3.14: Negative time delay distortions and perturbations of free induction decay. Open circles, SF spectra of NO/Ir{111}. Dashed grey curves assume the electron temperature (T_{el}) as input. Black curves are spectra produced using the friction model.

Figure 3.14 shows three NO pump-probe spectra at negative time delays. Each spectrum has two different calculated spectra overlaid. The black curves are calculated using the friction model described in section 3.4, where Γ=0.7 eV, ϵ=1.5 eV and τ_{el}= 670 fs. The grey dashed curves are calculated with an input that corresponds to the frequency shift being directly proportional to the electron temperature, essentially equivalent to an τ_{el} of ~100 fs. It is clear that for very fast changes, strong perturbation of the free induction decay at negative delay times causes modulation of the spectra beyond that observed. The frequency of these modulations is inversely proportional to the pump probe delay ($\Delta\omega = 2\pi/\Delta t$) [34].

The friction model fits the peak height, width and shape very well, while the curves relying upon T_{el} as an input distort the spectra far too much. The spectral analysis at negative delay times and the lack of a pump photon energy dependence, provide good evidence that short lived nascent electrons are not responsible for the observed spectral changes in the pump-probe spectra.

3.5.4 Implications of Experiments and Dynamics

Bonding and Bending

To understand how the hot electron distribution generated from a femtosecond laser pulse can cause bending of the NO relative to the iridium surface, a good understanding of the orbitals responsible for the Ir-NO bond is needed. A schematic of the molecular orbital diagrams for CO and NO adsorption on Ir{111} are given in Figure 3.15. In an unperturbed state, the bonding of NO at an atop site is dominated by the iridium d_{z^2} and NO 5σd orbitals. The iridium d_{z^2} orbital is favoured as it extends furthest from the surface and the $d_{\pi}/2\pi^*$ interaction is weak. On moving to bridge or hollow sites the $d_{\pi}/2\pi^*$ interaction increases and more back donation causes a red-shift in the N-O bond frequency.

Upon population of the NO $2\pi^*$d antibonding orbital by hot electrons, the NO has to react to maximise the overlap between the iridium d_{z^2} and the freshly populated NO $2\pi^*$d. The easiest way for the system to reflect the increased $d_{z^2}/2\pi^*$d character of the Ir-NO bond, is for the NO to bend over relative to the iridium surface. It is this response that has been measured in the NO pump probe experiments to take 670 fs. For the heavy noble elements of Ag, Au, Pd and Pt, the $d_{\pi}/2\pi^*$ interaction is very weak due to the diffuse nature of the d-orbitals. This favours $d_{z^2}/2\pi^*$ hybridisation, giving a bent geometry for both atop and bridge adsorption sites [91].

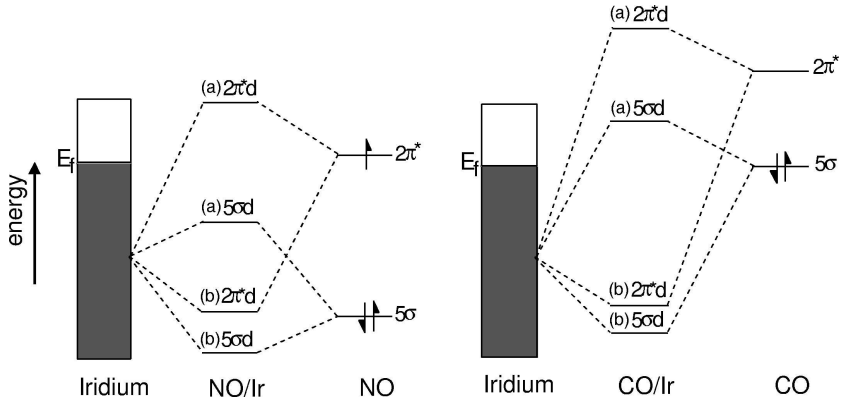

Figure 3.15: Schematic energy diagram of NO and CO interacting with an iridium surface. The NO and CO 5σ and 2π orbitals mix with the d band to form two bonding states (b)5σd and (b)$2\pi^*$d. The corresponding anti-bonding orbitals are the (a)5σd and (a)$2\pi^*$d.

The next question is, how much does the NO bend? A comparison with the DFT calculations presented in section 3.4.1, suggests that just below the desorption threshold of NO on Ir{111}, an Ir-N-O angle of ~20° is likely. As well as the Ir-N-O angle increasing, the nitrogen atom is shifted off the central axis of the iridium atom, causing a lengthening and weakening of the N-O and N-Ir bonds. This rearrangement is similar to the frustrated rotation, as the nitrogen and oxygen atoms move in opposite directions, in a fashion akin to the low frequency mode. The difference between the two is that the frustrated rotation is populated thermally, whereas the bending described above is electronically driven.

Desorption and Dissociation

Differences have been observed in photodesorption experiments of NO and CO from the Pt{111} surface. Experiments have shown that NO leaves the surface with a higher rotational excitation than CO [92]. This qualitatively makes sense, as adding an extra electron into the NO $2\pi^*$d orbital makes it isoelectronic with

O_2, which adsorbs parallel to the Pt{111} surface. The results presented herein for femtosecond excitation of NO/Ir{111} fit well with the observation of rotationally excited photodesorbed NO. Considering the small amounts of charge transfer needed for bending and photodesorption of NO on Ir{111} and the results of a theoretical simulation of laser photodesorption carried out by Saalfrank [93], it would indicate that only a partial transfer of charge is needed to drive NO photodesorption.

The discussion of adsorbates bending over leads naturally onto the topic of dissociation. To dissociate NO or CO on a flat metal surface, bending of the molecule relative to the surface normal is required. As explained previously, this allows transfer of electrons into the $2\pi^*$d orbital, allowing fission of the intermolecular adsorbate bond. Flat lying or severely bent precursors to dissociation have been detected for NO on Rh{100} and Ni{100} [94,95] and for CO on Cr{110} and Fe{100} [96, 97].

The propensity for a metal surface to dissociate either NO or CO depends largely upon its position in the periodic table, as well as other factors like crystal facet and temperature. For CO the dividing line between dissociative and molecular adsorption passes between Fe/Co, Tc/Ru and W/Re. Whereas for NO, things are more complicated and generally shifted to the right of the d-block. NO has a preference for molecular adsorption only on Pd and Pt, while showing a mixture of molecular and dissociative adsorption on Ni and Ir [98].

With respect to dissociation trends across the transition metals, the most important factor is the position of the d-band with respect to the adsorbate $2\pi^*$ orbital. As you move from the LHS to the RHS of the periodic table, the energy of the d-band lowers due to increasing nuclear charge. Hence, the overlap between the metal d-band with the adsorbate $2\pi^*$ decreases and the $2\pi^*$d bonding hybrid orbital is less accessible to metal electrons. Increased population of the

$2\pi^*$d bonding orbital via shifting of the d-band up (at LHS of d-block) strengthens the metal-adsorbate bond, but weakens the intermolecular bond. As the intermolecular bond weakens due to this process, the adsorbate bends over relative to the surface and dissociates due to the larger degree of $d_{z^2}/2\pi^*$d bonding character.

The bending induced via femtosecond laser excitation is different to that displayed naturally across the periodic table for the following reasons. The generation of a hot electron distribution populates the $2\pi^*$d anti-bonding orbital which lies well above the Fermi level. This causes weakening of not only the adsorbate intermolecular bond, but also the metal adsorbate bond. It is for this reason that desorption will nearly always favour dissociation in femtosecond laser experiments, if the $2\pi^*$d antibonding orbital lies close to the Fermi level.

This effect is demonstrated nicely on the iridium surface by the DFT calculations and in experiments. As the NO is bent by ~20°, an additional 0.03 e^- are added into the $2\pi^*$d anti-bonding orbital, this is due to better overlap with the iridium d_{z^2} in a bent geometry . This then leads to weakening of both the Ir-NO and N-O by a total of 0.14 eV. What is surprising from these results is that such a small amount of charge is needed to considerably weaken the Ir-NO and N-O bond. For this reason, alloying iridium might generate a surface that is very sensitive to charge transfer but also facilitate dissociation as well as desorption.

3.6 Conclusions

Pump-probe transients for both CO and NO adsorbed on Ir{111} have been modelled by considering a transient charge transfer from the metal into the $2\pi^*$d antibonding adsorbate orbital. The behaviour of NO/Ir{111} is found to be strongly non-adiabatic, whereas CO is found to behave adiabatically. For NO, the molecular $2\pi^*$ orbital is relatively close to the Fermi level in energy, hence the NO $2\pi^*$d

anti-bonding hybrid orbital is easily populated by hot electrons generated from a femtosecond laser. The response of NO to this transient charge transfer is to bend over on a time scale of 670 fs and ultimately desorb at high fluences. For CO, the molecular $2\pi^*$ orbital is high above the Fermi level, hence a hot electron distribution will not populate the CO $2\pi^*$d anti-bonding orbital. Therefore CO does not bend over and will ultimately desorb over a time scale of several picoseconds at high fluences, due to a thermal mechanism involving coupling to the lattice phonons via low frequency vibrational modes.

Chapter 4

Vibrational Dynamics

4.1 Introduction

On metal surfaces the vibrational decay of high frequency oscillators (eg C-O and N-O) is very fast due to excitation of metal electron-hole pairs. This gives larger linewidths than on semiconductor surfaces, where the only available decay pathways are slower surface phonon channels. For an idealised homogeneous distribution of molecules at a surface at 0 K, the linewidth of the infrared spectra is not infinitely sharp, due to the finite vibrational lifetime T_1 of the excited vibrational state. If the oscillator follows a purely exponential decay, a Lorentzian line shape will be observed in the frequency domain, with a full width half maximum (FWHM) given by $\Gamma = 1/2T_1$.

However, this is observed to be a simplification due to pure dephasing and inhomogeneity. It is found that the population lifetime T_1 is too long to describe the linewidth observed in IR spectra, suggesting a dephasing or T_2 mechanism is needed. This is ascribed to the oscillating dipoles losing their mutual phase relationship by a pure dephasing process T_2^*. This reduces the experimentally observed macroscopic IR polarisation and hence gives rise to an overall dephasing

time T_2 for a homogeneous distribution. The mechanism behind the T_2^* process is the anharmonic coupling of the high frequency adsorbate bond with low frequency modes (eg. frustrated translation), populated thermally via the lattice phonons. The relationship between Γ_{FWHM}, T_1, T_2 and T_2^* is given by the following:

$$\Gamma \propto \frac{1}{T_2} = \frac{1}{2T_1} + \frac{1}{T_2^*} \tag{4.1}$$

It is noted that at very low temperatures, where thermal population of low frequency modes is negligible, $T_2^* \rightarrow \infty$ and the linewidth can be given by $1/2T_1$ [99].

In reality, infrared spectra of surface-adsorbate systems are complicated further by inhomogeneity of the molecules present at the surface. Figure 4.1 depicts the origin of inhomogeneous broadening from disorder and defects on surfaces. This gives a distribution of oscillator frequencies, convoluting the natural Lorentzian lineshape with a Gaussian distribution of frequencies. The difficulty

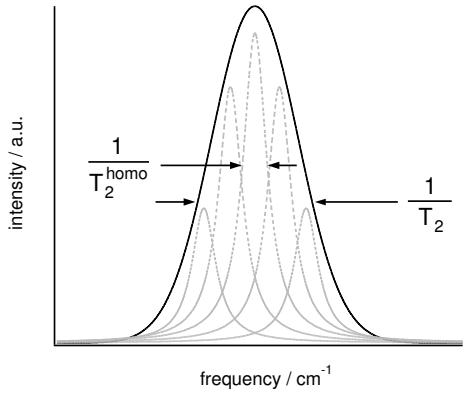

Figure 4.1: Inhomogeneous broadening of a spectral line. The individual Lorentzians (grey dashed lines) represent five different oscillator environments, be they defect sites or near step edges. While the total width ($1/T_2$) is observed in IR and free induction decay, photon echo experiments allow the determination of the homogeneous linewidth, $1/T_2^{\mathrm{homo}}$.

lies in trying to separate the observed spectral linewidth ($1/T_2$) into its inhomogeneous ($\Delta\omega$) and homogeneous ($1/T_2^{homo}$) components. This task is beyond the analysis of standard infrared spectra in the frequency domain, and hence requires direct measurement of the surface polarisation in the time domain. It is for this reason that experimental techniques have been designed using ultrafast lasers to measure these parameters directly. These include Free Induction Decay (FID) and photon echo experiments, as explained herein.

4.1.1 Free Induction Decay

The simplest time domain experiment is a free induction decay (FID) experiment, which measures the dephasing time T_2. In this experiment a coherent vibrational polarisation is induced by a short ($\sim$ 200 fs) resonant infra-red laser pulse. After a given delay τ, the coherence of the polarisation is probed by upconverting it with a femtosecond visible pulse to produce infrared-visible sum frequency light. Figure 4.2 shows the difference in pulses for a linewidth measurement in (a) the frequency domain and (b) the time domain. A frequency resolved SFG probe consists of a femtosecond broadband IR pulse and a narrowband picosecond visible up-conversion pulse. It is the spectral width of the visible pulse that gives the spectral resolution. In the time domain, a femtosecond IR and femtosecond visible up-conversion pulse are used, allowing temporal but not frequency resolution.

The first demonstration of a surface free induction decay experiment was carried out as part of a larger study into the vibrational decay mechanisms for the H-terminated Si{111} surface in 1990 [100]. Since then improved temporal resolution has allowed similar FID experiments for CO/Cu{111} and CO/Ru{10$\bar{1}$0} [34, 101]. Roke *et al.* have since tried to measure the degree of inhomogeneity of CH_3CN/Au with a careful analysis of the free induction decay [102]. This shall

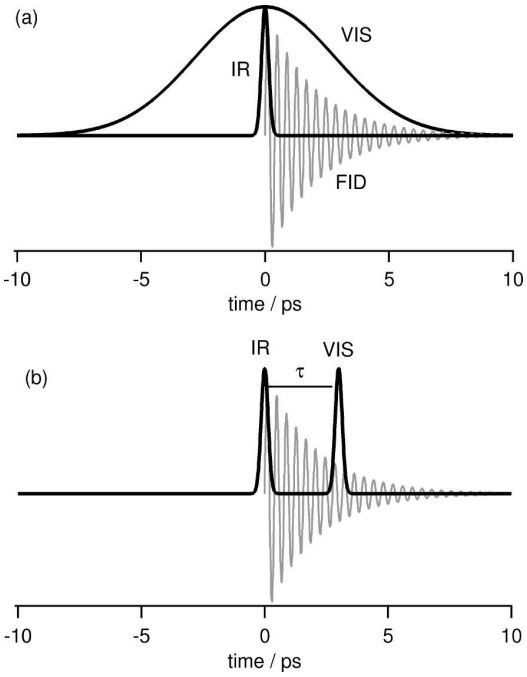

Figure 4.2: (a) Frequency resolved SFG probe consisting of a femtosecond IR pulse and picosecond visible up-conversion pulse. The FID is integrated over the pulse length of the up-conversion pulse. (b) Temporally resolved SFG probe, consisting of a femtosecond IR and visible pulse. The FID is sampled at set delay times by the up-conversion pulse.

be discussed later in section 4.4.

4.1.2 Photon Echoes

Photon echoes provide the only conclusive way to measure the inhomogeneity for an adsorbate system [103]. In an SFG photon echo experiment two infrared pump beams are used with a visible probe. The first infrared beam (IR1) induces a coherent vibrational excitation of the molecular dipoles in an adsorbate layer at $t = 0$. The polarisation generated will then start to decay as in a standard FID and after a delay τ the second infrared beam (IR2) triggers the rephasing of the

molecular dipoles. At a delay 2τ from $t = 0$, the dipoles will all be oscillating in phase and a short pulse of IR light is emitted. The IR echo is detected by upconversion with a visible probe at a time t, where $t > \tau$ in a similar way to a standard SFG experiment. The pulse sequence for a two IR pulse-SFG photon echo experiment is depicted in Figure 4.3.

The rephasing at 2τ removes the effect of inhomogeneous broadening, only leaving the homogeneous linewidth. Importantly, a photon echo experiment can

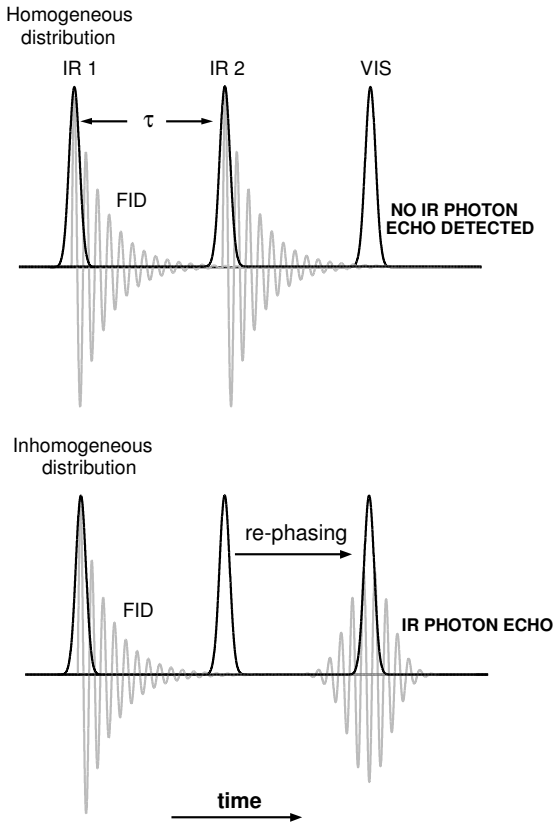

Figure 4.3: Pulse sequence for IR SFG photon echo experiment. For a homogeneous distribution no polarisation can be rephased, so the polarisation maximum is at $t = \tau$. For a dominantly inhomogeneously broadened distribution, the echo maximum is at $t = 2\tau$.

not rephase oscillators that have decayed via a homogeneous T_2^* mechanism, only those with different natural oscillation frequencies. It is for this reason that photon echo experiments allow for the separation of homogeneous and inhomogeneous contributions to the linewidth.

Echoes were first observed for spins using NMR in 1950 by E.L Hahn [104] and latterly for photons in a ruby crystal in 1960 by Kurnit *et al.* [105]. The existence of photon echoes on surfaces was initially predicted by Zhu and Shen in 1990 [106] and later demonstrated by Guyot-Sionnest for a semiconductor surface [100]. An excellent analogy to try and explain how an echo experiment can probe the homogeneous linewidth, even in the presence of large inhomogeneity, is given by Walsh *et al.* [107].

> "...consider the following footrace. Initially, all the runners are lined up a the starting line. At $t = 0$ the starting gun (analogous to the first laser pulse) is fired and the runners take off down the track. After running for some time, the faster runners have pulled out in front and the slower runners are somewhat behind. The runners are no longer in a line because of the inhomogeneity of their speeds. At time τ, the gun is again fired (analogous to the second laser pulse) and everyone turns around and runs back toward the starting line. If each runner maintains a constant speed out and back, then all the runners will cross the starting line exactly in line again. When the second gun was fired, the faster runners were farther away from the starting line than the slower runners, but since they run faster, the differences in distances is exactly made up by for by the differences in speeds. At the starting line the group is rephased; the inhomogeneity in speeds has been nullified. If the runners do not run at exactly constant speeds, but each runner has some fluctuation in speed about his average (homogeneous fluc-

tuations), then the runners will not all cross the starting line exactly in a line; there will not be perfect rephasing. A snapshot of the group as it crosses the starting line will reveal the small fluctuations in the runners' speeds, in spite of the large inhomogeneous distribution of speeds."

4.1.3 IR pump-SF probe Experiments

In conventional IR spectroscopy only the fundamental transition from $v = 1 \leftarrow 0$ is generally investigated, due to the narrow band source of IR light and low field strengths. With femtosecond laser pulses, the large bandwidth and high intensities allow for saturation of the fundamental transition and observation of the hot-band transition from $v = 2 \leftarrow 1$. As the IR energy is increased the fundamental transition ($v = 1 \leftarrow 0$) is saturated and significant population is transferred into the $v = 1$ state. Further absorption of another IR photon from the broadband laser pulse will

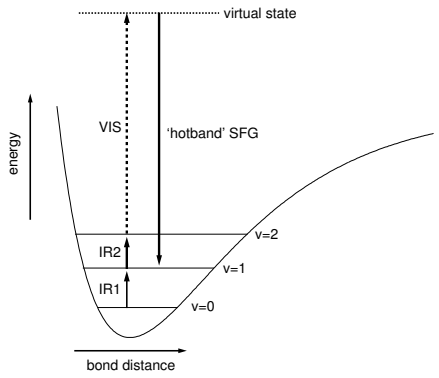

Figure 4.4: Diagram of a vibrational potential energy curve for a diatomic, including excited vibrational states $v = 1$ and $v = 2$. The hotband will be at a lower frequency than the fundamental, due to the anharmonicity of the molecular stretch.

give rise to a transition from $v = 2 \leftarrow 1$, leading to the observation of a hotband in the spectra. The frequency of the hotband is redshifted due to the anharmonicity of the CO bond, see Figure 4.4.

The observation of hotbands for metal adsorbate systems is largely dependent upon the intermolecular coupling between oscillators. For CO adsorbed on metal surfaces, the dominant interaction is dipole-dipole coupling, which sets in at typically a few percent of a monolayer (average distance between molecules around 10 Å) and leads to a blue shift of the frequency of several tens of cm^{-1}, depending on strength [108]. It also leads to line narrowing and a reduction in the IR intensity at higher coverages, due to screening reducing the effective dynamic dipole moment. The strength of dipole-dipole coupling has been traditionally determined by reflection-absorption infrared spectroscopy (RAIRS) using the infinite isotopic dilution technique of Crossley and King [108]. With increasing coverage, the CO overlayer makes a transition from a collection of localised (singleton) oscillators to delocalised phonons. Figure 4.5 shows SFG spectra at low and high IR pulse energy for a low coverage of CO on the Ir{111} surface (0.07 ML).

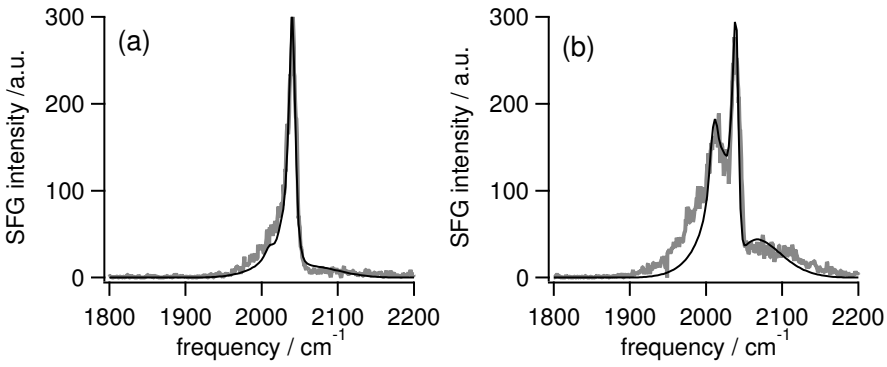

Figure 4.5: SFG spectra for 0.07 ML CO/Ir{111} layer with IR pulse energies of (a) 2.5 μJ and (b) 11 μJ. Part (b) shows the development of the hotband peak at a lower frequency to the fundamental. The black lines are spectra modelled using three level Bloch equations.

Although these static broadband experiments tell us about the nature of the oscillators present on the surface, they tell us relatively little about the temporal dynamics of vibrational excitation and decay mechanisms. For that we need IR pump probe spectroscopy. This involves pumping the system with an intense femtosecond laser pulse and watching how the molecules recover on a sub-picosecond time scale with a weak SF probe. These experiments yield the vibrational lifetime T_1, rather than a dephasing time T_2.

The first T_1 measurement was done on the H-terminated Si{111} surface [109]. Since then T_1 has been measured for CO/Cu{111} , CH_3S/Ag{111} and CO/Pt{111}, using either picosecond time resolved Sum Frequency or time resolved RAIRS [48, 49, 110]. The T_1 measurement presented here uses broadband IR pump-SF probe spectroscopy. This carries with it a significant improvement in temporal and spectral resolution, allowing not only a simple T_1 measurement, but also a more in depth modelling of the spectral changes on a sub-picosecond time scale.

4.1.4 Adsorption of CO on Ir{111}

CO adsorbs molecularly on Ir{111} on atop sites at all temperatures and coverages, giving a single C-O absorption band in RAIRS at frequencies above 2000 cm^{-1} [72]. A ($\sqrt{3} \times \sqrt{3}$)$R30°$ LEED pattern is observed around a surface coverage of 0.33 ML (~ 4 L exposure) and a ($2\sqrt{3} \times 2\sqrt{3}$)$R30°$ pattern at 0.58 ML (~ 20 L), which is found to be the locally accessible saturation coverage [59]. The structure of these overlayers is given in Figure 4.6. At extensive exposures over 20000 L a higher saturation coverage of 0.71 ML is observed from TPDs.

At coverages below 0.33 ML TPDs show a single peak, which is shifted from 570 K at 0.07 ML to 530 K at 0.33 ML. Above 0.33 ML, a low temperature shoulder develops due to increasing repulsive interactions between the molecules above the 0.33 ML coverage, see Figure 4.7.

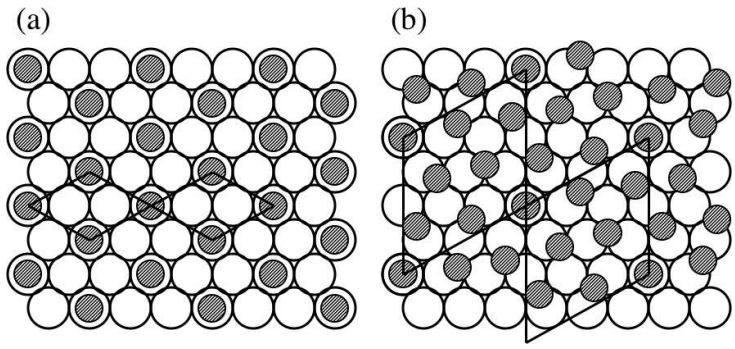

Figure 4.6: Structural models for CO on Ir{111}. (a) 0.3 ML ($\sqrt{3} \times \sqrt{3}$)R30° structure, (b) 0.58 ML ($2\sqrt{3} \times 2\sqrt{3}$)R30° overlayer.

For the $(2\sqrt{3} \times 2\sqrt{3})R30°$ structure it is unlikely that all CO molecules are adsorbed in well defined on-top sites, but at such high coverages the strong dipole-dipole lateral interactions between the CO molecules become similar to the periodic potential of the surface. Hence each molecule feels a similar substrate potential and an essentially similar adsorption site [111]

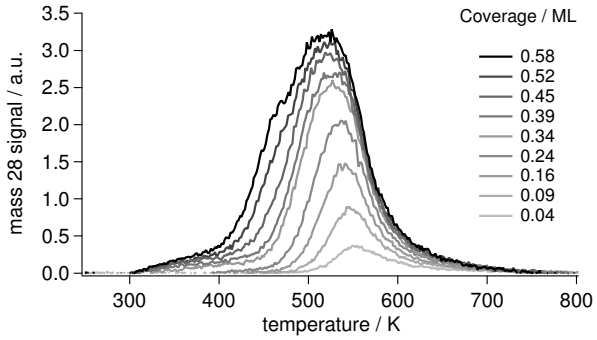

Figure 4.7: CO TPDs for Ir{111} up to 0.58 ML. The low temperature shoulder at high coverages is attributed to the ($2\sqrt{3} \times 2\sqrt{3}$)R30° structure.

4.2 Experimental

A full description of the femtosecond sum-frequency setup was given earlier in Chapter 2. Briefly, a Spectra Physics 10 Hz regeneratively amplified Ti:sapphire system delivers 140 fs pulses at 7 mJ of energy per pulse. Two light Conversion optical parametric amplifier (TOPAS) are each pumped by 2.5 mJ, 800 nm, 150 fs beams to produce mid-infrared pulses IR1 and IR2, with corresponding energies of 3 μJ and 10 μJ at 4800 nm (2083 cm^{-1}). The remaining 800 nm light is used for either broad or narrowband SFG upconversion in either temporal or frequency resolved experiments respectively. All beams are p-polarised. Temporal and spatial overlap of all beams (IR1, IR2 and 800 nm) is optimized and checked *in situ* on a caesium covered iridium surface via five-wave mixing [63].

CO is dosed via background dosing (20 L) to give a saturation CO coverage of 0.58 ML, corresponding to a $(2\sqrt{3}\times 2\sqrt{3})$ structure. This coverage gives a single C-O absorption band in RAIRS at 2080 cm^{-1} [72]. All experiments are carried out at 100 K.

To collect a spectrum and FID, only IR1 and the visible pulses are used. For the spectrum a picosecond narrowband visible pulse is used, whereas for the FID a femtosecond broadband visible pulse is used. After collecting a spectrum in the frequency domain, the slit was removed from the pulse shaper in the visible upconversion path, and a neutral density filter inserted (to maintain similar visible energies and to protect the sample.) For the FID, the time delay (τ) between IR1 and visible pulse is scanned in steps of 66 fs from τ = -1 ps to τ = +4 ps.

The mid-IR photon echo is not easily observed, with a signal size that is two orders of magnitude lower than other five wave mixing processes on the same surface (IIV SFG for example). The main experimental difficulty is the selective collection of only the echo exclusively. This was achieved by careful spatial alignment and an iris on the exit, at expense of the signal. The SF upconverted echo

direction is given by the direction $\mathbf{k}_{\mathrm{SF(echo)}} = 2\mathbf{k}_{\mathrm{IR2}} - \mathbf{k}_{\mathrm{IR1}} + \mathbf{k}_{\mathrm{VIS}}$. Spatial alignment was carried out by calculating the echo signal direction from the relative positions of the IR1 and IR2 IV-SFG signals in a $LiIO_3$ crystal.

For the IR pump-SFG probe experiments, alignment is similar in nature to the photon echo, relying upon a good IIV SFG alignment to ensure spatial and temporal overlap of all three beams on the surface. The stronger infrared pulse IR2 was used as the pump pulse and IR1 as the probe. Both pump and probe OPAs were set to a wavelength of 4700 nm unless specified.

4.3 Results

4.3.1 IR Spectra, Free Induction Decays and Photon Echoes

The IR Spectrum

The first step towards measuring the components that define the vibrational properties of a system, is to measure the linewidth (Γ) of a spectrum in the frequency domain. Figure 4.8 shows the SF spectrum of a saturated 0.58 ML coverage of CO on the Ir{111} surface at 100 K. The resonant signal from the CO and non-resonant contribution from the metal surface are clearly visible. The CO shows a relatively narrow single resonance at 2080 cm^{-1}, which is characteristic of a strongly dipole-dipole coupled adsorbate layer. The spectra can be fitted with the conventional expression for the total second order susceptibility $\chi^{(2)}$ for SFG, given by the sum of a non-resonant contribution $\chi^{(2)}_{NR}$ and the resonant part $\chi^{(2)}_{RES}$:

$$\begin{aligned} \chi^{(2)} &= \chi^{(2)}_{NR} + \chi^{(2)}_{RES} \\ &= A_{NR}e^{i\phi} + \frac{A_{RES}}{\omega_{IR} - \omega_{RES} + i\Gamma_{\mathrm{RES}}}, \end{aligned} \tag{4.2}$$

where A_0 and ϕ are the magnitude and phase of the non-resonant surface contribution and A_{RES}, ω_{RES} and Γ_{RES} are the amplitude, frequency and half-width of the resonance [35]. The measured signal is proportional to $|\chi^{(2)}|^2$. The resonances are actually fitted using a Voigt function, to allow for the spectral width of the visible upconversion pulse. The width of which is taken from a cross-correlation with the femtosecond infrared pulse from a Cs/Ir surface. The linewidth Γ_{FWHM} was measured to be 5.6 ± 0.5 cm^{-1}, which corresponds to a T_2 time of 1.89 ± 0.15 ps, as given by the relationship [112]:

$$\Gamma_{\mathrm{FWHM}} = \frac{10.6\,\mathrm{cm}^{-1}}{T_2/\mathrm{ps}}. \tag{4.3}$$

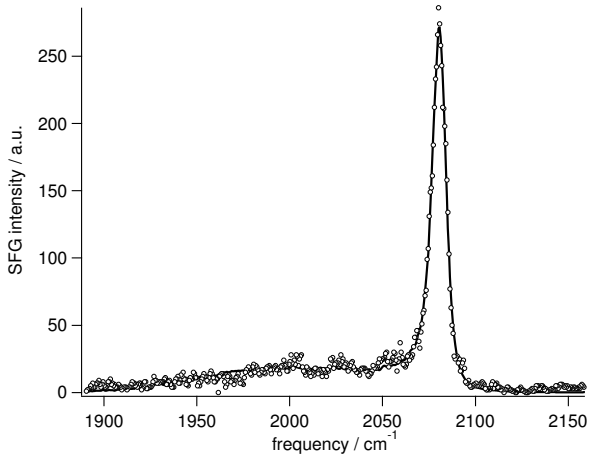

Figure 4.8: SFG spectrum of the C-O stretch on Ir{111} at 2080 cm^{-1}. The dashed line is a fit that incorporates both the non-resonant and resonant contributions of the SF signal according to equation 4.2. The linewidth given by the FWHM is 5.6 ± 0.2 cm^{-1}, corresponding to a T_2 of 1.89 ± 0.15 ps.

Free Induction Decay

Moving from the frequency domain, a free induction decay (FID) experiment was performed to measure T_2 in the time domain. Figure 4.9 shows a FID for a sat-

urated CO layer on the Ir{111} surface at 100 K. The SF intensity is given by the square of the second order polarisation, where the second order susceptibility $\chi^{(2)}_{RES}$ has the temporal form:

$$\chi^{(2)}_{RES}(t) = \exp(-t/T_2). \tag{4.4}$$

The FID is modelled using a program written by J.P.R Symonds, which calculates the sum frequency intensity for a given delay time τ between infrared and visible pulses [14]. The second order polarisation $P^{(2)}$ is given by a convolution of the IR polarisation with the visible upconversion pulse:

$$P^{(2)}(t,\tau) = E_{VIS}(t-\tau)\Big[\alpha \int_{-\infty}^{t} E_{IR}(t')\chi^{(2)}_{RES}(t-t')\,dt' + \beta E_{IR}(t)\Big], \tag{4.5}$$

where α gives the magnitude of the resonant contribution, determined by the size of the infrared transition dipole moment and the Raman polarisability. β gives the magnitude of the corresponding non-resonant contribution, determined by the size of the non-resonant hyperpolarisability. E_{VIS} and E_{IR} are the envelopes of the visible and IR fields respectively. Upon fitting the FID, a T_2 value of 1.93 ± 0.13 ps is obtained. This is in agreement with the relaxation time taken from the SF spectra in Figure 4.8. The inset to Figure 4.9 shows the difficulty in trying to determine inhomogeneity from the shape of a FID. The solid line shows a standard exponential fit of the resonant part of the FID from $\tau = 1 \rightarrow 4$ ps, assuming a homogeneous distribution. The dashed line is fitted using the T_2 time and inhomogeneity determined from the photon echo (Figure 4.10), the details of which shall be discussed later.

The FID is plotted without background subtraction to demonstrate how difficult and subjective analysing FID can be. The results are very much dependent on the magnitude of background subtraction, which can be hard to determine accurately experimentally. The magnitude of the background for the clean surface was measured from a cross-correlation to be 0.4. However, if 0.4 is subtracted from the

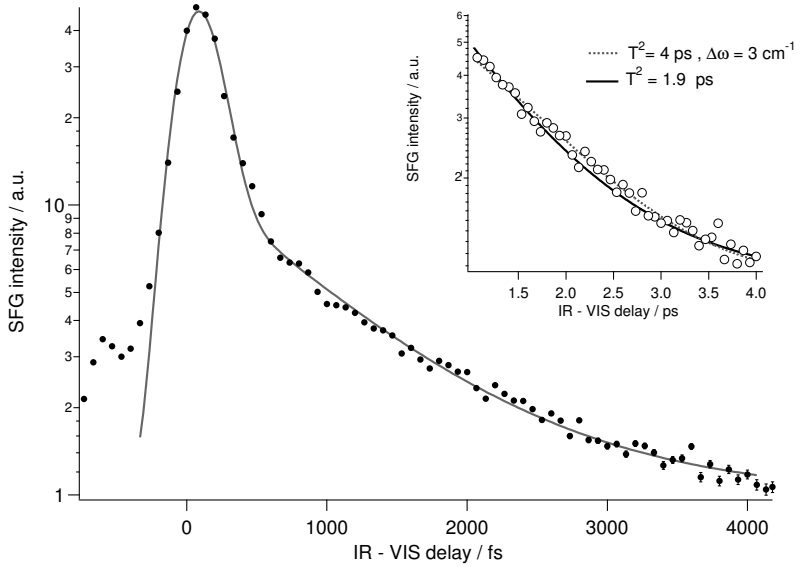

Figure 4.9: Logarithimic plot of SFG FID signal as a function of IR-VIS delay. The inset shows fitting of the resonant section from $\tau = 1 \rightarrow 4$ ps with a purely homogeneous and partially inhomogeneous distribution, as described in the text.

data in Figure 4.9 the FID tail still curves upwards. This suggests that the background measurement for the clean surface is too small for the CO/Ir{111} system. The FID plotted in Figure 4.9 was fitted with an offset of 1.1, which was determined from the fitting routine. For future experiments the background should be measured for the adsorbate covered surface at very long delay times, giving an experimentally determined background for subtraction.

IR Photon Echo

An IR surface photon echo experiment was also carried out for the saturated CO/Ir{111} layer at 100 K. The echo signal is not easily observed and data scatter is observed due to low photon counts. Figure 4.10 is a plot of the unconverted IR surface photon echo signal as a function of IR2-VIS delay time, parts (a), (b) and (c) refer to IR1-IR2 delay times (τ) of 1.0,1.2 and 1.5 ps respectively. The

temporal dependence of the surface vibrational polarisation at time $t > \tau$ is given by [100]:

$$\chi^{(2)}(t, \tau) = \exp(-t/T_2^{homo}) \exp[-2\pi^2 \Delta\omega^2 (t - 2\tau)^2]. \quad (4.6)$$

The first part of this equation gives the irreversible dephasing of the oscillators from the homogeneous T_2^* process. The second part $\exp[-2\pi^2 \Delta\omega^2 (t - 2\tau)^2]$, allows for the rephasing of oscillators at different frequencies, given by a Gaussian distribution of frequencies of width $\Delta\omega$, the inhomogeneity. The echo curves are fitted with a T_2 of 4 ± 0.3 ps and an inhomogeneity of 3 ± 0.1 cm^{-1}. The reduction in signal as τ increases, is due to an increase in the amount of polarisation that cannot be rephased, due to the irreversible T_2^{homo} homogeneous decay mechanism with the lattice phonons.

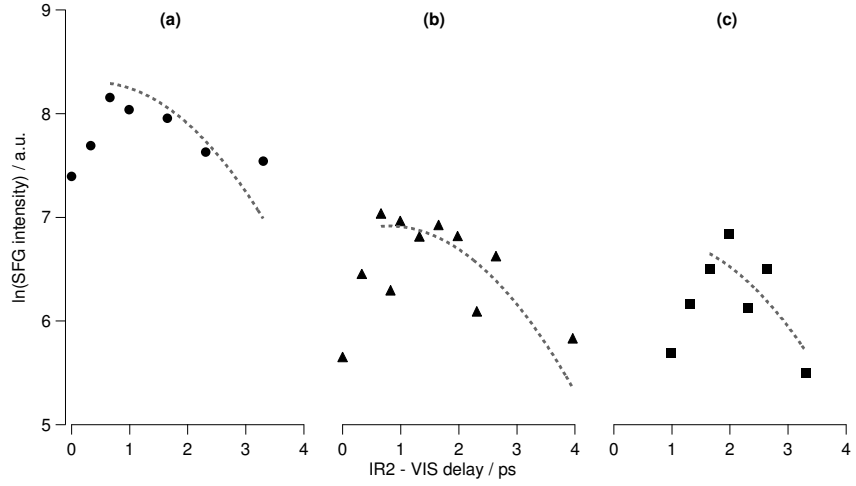

Figure 4.10: Logarithmic plots of the CO/Ir{111} SFG infared photon echo as a function of IR2-VIS delay. Displayed are three IR1-IR2 delay times: (a) 1.0 ps, (b) 1.2 ps and (c) 1.5 ps. The dashed lines are fits to equation 4.6 as described in the text. A T_2^{homo} of 4.0 ps was used and an inhomogeneity of 3.0 cm^{-1}.

4.3.2 Infrared Pump-SFG Probe

The primary aim of the IR pump-probe experiments was to measure the vibrational lifetime T_1 of CO on the Ir{111} surface. This can then be used in conjunction with the T_2 and T_2^{homo} from the FID and photon echo experiments to measure the inhomogeneity and pure dephasing time T_2^*. However, the experiments provided a great deal more information, including the observation of a transient vibrationally excited state.

The data is split into two data sets, one at a low coverage of 0.15 ML and one at a high coverage of 0.58 ML. At low coverage the dipole-dipole coupling is relatively small and the CO molecules behave as near as possible to individual oscillators. At high coverage, the strong dipole-dipole coupling force the oscillators to behave as a dispersed 2D phonon, with very different excited state behaviour.

Low Coverage

At low coverage, pumping CO/Ir{111} with an intense IR femtosecond pump pulse yields a distinctly clear hotband in the SFG spectra and a reduction in intensity of the fundamental. Figure 4.11 shows the spectrum from $t = 0$ pump-probe delay along with a scaled no pump spectrum. The hotband appears around $t = 0$ and is relatively short lived ($\sim$ 2 ps). The separation between hotband and fundamental at this coverage is expected to be 20 cm^{-1}, as determined from static hotband experiments [35]. The observed separation in the pump-probe transients is $\sim$18 cm^{-1}.

The simple approach used previously to calculate T_1 times from picosecond infrared pump-probe experiments ignores coherent effects, and treats the system as a two level system. As the resonant SF polarization is proportional to the population difference between $(n_{(v=1)} - n_{(v=0)})$ the change in SF intensity should give the T_1 lifetime [113, 114]. However, it is clear that this analysis is inappropriate.

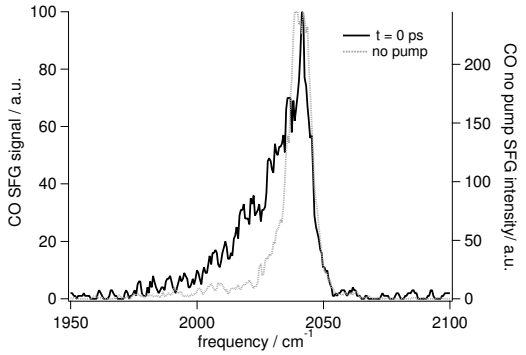

Figure 4.11: IR pump-probe spectrum for delay of $t = 0$ ps and scaled no pump spectrum. The shoulder at lower frequency to the fundamental is a transiently observed hotband. Coverage of CO on Ir{111} is 0.15 ML.

A simple measure of the SFG intensity recovery will not give a good value for the T_1 time for decay of population from $v = 1$ to $v = 0$, because the total SF intensity will contain signal from the hotband transition from $v = 2 \leftarrow 1$. It is for this reason that a reliable calculation of the T_1 time requires modelling with a three level system.

The spectra are modelled with a theoretical approach described by Joffre in [115], the details of which are described in Appendix B. This uses a combination of Green functions and convolutions to solve the Bloch equations. Importantly, it allows for third order density matrix effects, hence the interaction between the two infrared fields and the resulting coherent effects are accounted for.

Figure 4.12 shows three pump-probe spectra from $t = 0$, 2.5 and 8 ps pump-probe delays. The black lines give the result of the modelling and show excellent agreement with the experimentally observed spectra, including the reduction in intensity of the fundamental and the growth of the hotband at lower frequencies. The spectra were modelled with a T_1 time of 2.4 ps for the population decay from $v = 1$ to $v = 0$. The T_2 time for dephasing of the hotband transition $v = 2 \leftarrow 1$ was twice as fast as for the fundamental $v = 1 \leftarrow 0$, where $T_2^{10} = 1.9$ ps and $T_2^{21} = 0.9$ ps. In

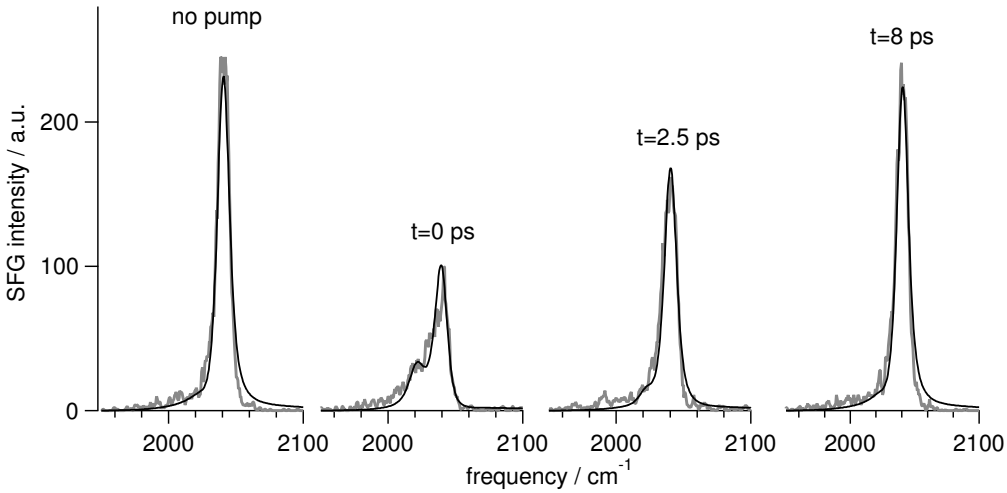

Figure 4.12: IR pump-SFG probe spectra for delay times of t = 0, 2.5 and 8 ps for a low coverage of CO on Ir{111}. The black lines are fits from the model described in the text.

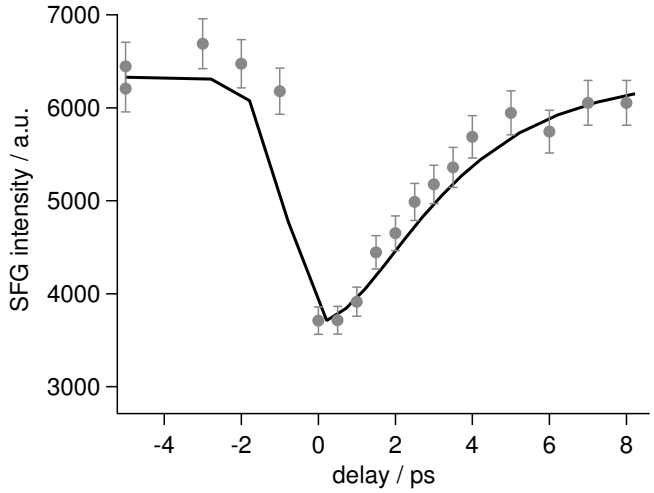

Figure 4.13: Plot of total SF integrated intensity vs IR pump-probe delay for low coverage CO on Ir{111}. The black curve is a fit using the model describe in the text.

Figure 4.13 the total integrated SFG intensity for both hotband and fundamental is plotted against pump-probe delay. Due to the contribution of intensity from the hotband, it can be seen that the recovery of the SF intensity shows a sigmoidal profile, rather than exponential. Once again this recovery is fitted well by the model.

However, an area which does not give such excellent agreement is at very short negative time delays. Figure 4.14 shows the SF spectra from $t = -0.8$ ps pump-probe delay and the modelled trace. The oscillations can be observed in the modelled spectra for the duration of the free induction decay at negative delays. This inconsistency cannot currently be accounted for in the modelling.

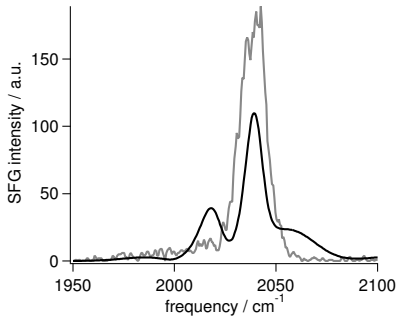

Figure 4.14: SF spectra at $t = -0.8$ ps for low coverage CO IR pump-SF probe experiment and modelled trace. The frequency oscillations are due to perturbation of the free induction decay by the IR pump pulse.

High Coverage

The pump probe transients at high coverage are very different in nature to their low coverage counterparts. The SF spectra for $t = 0$ and 2 ps pump-probe delay are plotted with a scaled no pump spectrum in Figure 4.15. The C-O peak undergoes a large shift to low frequencies and extensive broadening. Also at around $t = 0$ ps a dip can be observed in the centre of the peak.

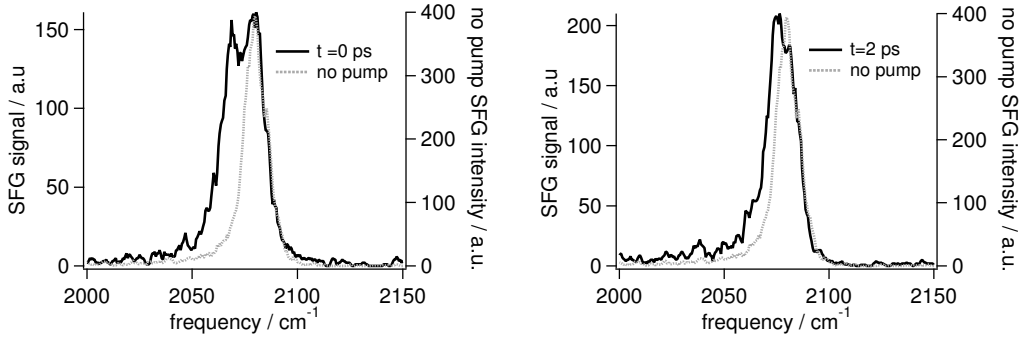

Figure 4.15: IR pump-probe spectra for high coverages of CO on Ir{111}(0.58 ML) at t = 0 and 2 ps delay times, included for comparison are the scaled no pump spectra.

The nature of the spectrum at zero pump-probe delay was examined further by scanning the pump wavelength over the CO frequency. In Figure 4.16 the probe OPA wavelength was kept constant at 4700 nm and the pump OPA wavelength centre scanned from 4500 nm to 4900 nm, which corresponds to a shift of ~180 cm^{-1}. This shows that the dip is at a maximum when the IR fields are overlapped in frequency.

Although the dip makes fitting the spectra difficult, the frequency shift and width at FWHM can be retrieved using a Voigt fit and the SFG intensity measured using a simple integral of the peak. The CO SFG frequency shift, peak width and intensity are plotted as a function of IR pump-SF probe delay in Figure 4.17. The SF intensity recovers linearly with delay, while the frequency shift and width both recover exponentially. The frequency shifts by 4 cm^{-1}, the width increases from 6 to 14 $cm^{-1}$and the SF intensity is reduced by nearly 60%.

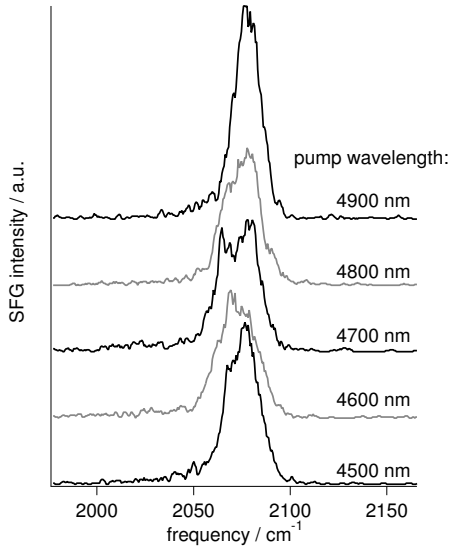

Figure 4.16: SF spectra at $t = 0$ as a function of pump wavelength for 0.58 ML CO/Ir{111} at 100 K. The probe is kept constant at 4700 nm.

4.4 Discussion

The experimental results shall initially be reviewed and then the discussion split into two sections. The first shall look at comparing the results from the IR spectra, free induction decay and photon echo, with the aim of determining the system inhomogeneity. The second shall focus on the results from the infrared pump-probe experiments and the corresponding coverage dependent vibrational dynamics.

4.4.1 Experimental review

The results from the IR spectra, FID, photon echo and IR pump-probe experiments allow for the generation of a complete set of vibrational parameters for the CO/Ir{111} system. An overall T_2 time of 1.9 ps, a lifetime T_1 of 2.4 ps and a homogeneous T_2^{homo} time of 4.0 ps are retrieved. This results in a pure dephasing time T_2^* of 24 ps. Expressed in frequency this gives a total linewidth of 5.6 cm^{-1},

containing a homogeneous contribution of 2.7 cm^{-1} and an inhomogeneous one of 3.0 cm^{-1}.

The IR pump-SF probe spectra for low and high coverages of CO on Ir{111} showed markedly different behaviour, as expected from the development of dipole-dipole coupling as a function of surface coverage. At low coverage where dipole-dipole coupling is relatively low, the CO overlayer acts as individual molecules.

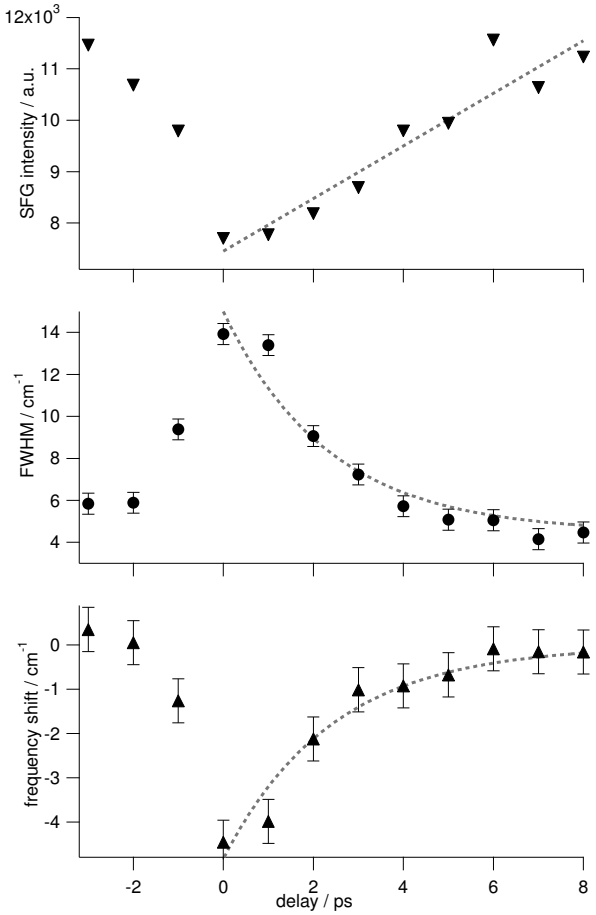

Figure 4.17: SF frequency shift, width and intensity as a function of IR pump-SF probe for 0.58 ML CO on Ir{111}. The intensity is observed to follow a linear recovery, while the width and frequency shift recover exponentially with time constants of 2.3 and 2.4 -0.3/+0.4 ps respectively.

When the pump and probe infrared pulses are overlapped in time at $t = 0$ the IR intensity is at a maximum and a hotband at lower frequency can be observed in the spectra. This is attributed to the pump pulse causing transient population of the $v = 1$ vibrationally excited state. The total SFG intensity shows a sigmoidal recovery at positive decays, rather than an exponential decay as expected for a simple two level system. The shape of the pump-probe spectra at positive delay times and the recovery in SFG intensity is modelled well using Green functions to solve the Bloch equations for a three level system.

At high coverage the CO SFG spectra show no signs of individual molecular anharmonicity. The C-O peak shifts to lower frequency by nearly 4 cm^{-1} and doubles in width. The width increase and frequency shift both recover exponentially with pump delay, with lifetimes of 2.4 ps. However, the SFG intensity recovers linearly with pump-probe delay. At around $t = 0$ ps delay a dip can be observed in the spectra.

4.4.2 Adsorbate Inhomogeneity

Before considering the structural implications and nature of the inhomogeneity at the surface, it is required to clarify why the FID is incapable of assigning the inhomogeneity. It can be seen from the inset to Figure 4.9 that a decay composed of homogeneous and inhomogeneous components (as determined from the photon echo) has very little effect on the FID tail. While this approach has been used previously [102], the associated problems are illustrated clearly in the measurements of Roeterdink *et al.* [116]. The inhomogeneity of 0.5 ML CO/Pt{111} below 170 K is given as 2 ± 2 cm^{-1}, i.e. the measurement cannot even assert the presence of inhomogeneity. The photon echo measurement however, can measure a comparable inhomogeneity to within 0.1 cm^{-1}.

The measured inhomogeneous contribution of 3.0 cm^{-1} does not reflect the

full inhomogeneity of the CO overlayer. Persson and Ryberg [117] have demonstrated that in a strongly dipole-coupled layer high frequency oscillators screen the electric field of low frequency oscillators, which in turn enhance the field at higher frequencies. If the dipole coupling strength is twice as large as the inhomogeneous frequency distribution, line narrowing by dipole coupling is almost complete and the homogeneous width is recovered. The dipole coupling strength for saturation CO/Ir{111} is very large at 35 cm^{-1} [72] and therefore has the potential to mask a relatively large inhomogeneity.

It is possible to switch off dipole coupling whilst preserving the chemical environment by observing the localised mode of a minority CO isotope [118]. The smallest amount of minority $^{12}C^{16}O$ detectable within a saturated layer of $^{13}C^{18}O$ is 15 %, due to a strong drop in SF intensity caused by a chemical change of the Raman tensor as the coverage is increased to saturation. However, it is know from observation of the vibrational hot band that 15 % of saturation coverage can still be well described by localised oscillators [35]. This localised mode has a linewidth that is 5 cm^{-1} larger than a saturated, fully dipole-coupled layer. If this is added to the inhomogeneity value from the photon echo result, an estimate of 8 cm^{-1} for the inhomogeneity of the local environment is obtained.

This value is unlikely to be caused by surface imperfections, as CO on defect sites like step edges has a very different resonance frequency ($\sim$ 20 cm^{-1}). The inhomogeneity is more likely to be caused by the nature of the $(2\sqrt{3}\times 2\sqrt{3})R30^\circ$ CO overlayer. This layer is a coincidence structure, where only a sixth of the molecules sit strictly on atop sites. In such a layer the static lateral interaction between the CO molecules becomes as important as the periodic surface potential. Therefore, the value of 8 cm^{-1} is a measure of the degree to which the CO molecules feel a difference in the surface potential.

Not all of the echo peak shapes are described well by one value for T_2^{homo}.

The echo measured at 1.5 ps IR1-IR2 delay would require a larger inhomogeneity to improve the fit. This is an indication that the frequency fluctuations from the inhomogeneous distribution may contribute to the dephasing on different time scales. The nature of the processes behind this are currently uncertain, but could be explored further by more extensive measurements of the echo peak shape.

The very long pure dephasing time of 24 ps emphasises that coupling to surface phonons via low frequency adsorbate modes [77] is negligible at low temperatures. It is only at room temperature that pure dephasing starts to become a significant relaxation processes.

4.4.3 IR pump-probe

Low coverage

The observation of a transient hotband using IR pump-probe is an experimental first. T_1 and T_2 times for the $v = 1 \leftarrow 0$ transition have been measured previously in the time domain, while T_2 for the $v = 2 \leftarrow 1$ transition has not. This allows theoretical predictions for the dephasing of the excited state to be benchmarked against experiment [119].

The modelling introduced to understand this system has not been applied to surface systems previously and provides an easier approach to solving the Bloch equations. While further iterations of these calculations may improve the results, overall agreement is excellent. The perturbation in the modelling at negative delays is probably due to the unrealistic situation that both pump and probe electric fields overlap perfectly with each other in frequency. A systematic theoretical study into the modelling of this system should enable significant improvements to the spectral fitting at negative time delays.

High coverage

At high coverage, the dipole-dipole coupling is large enough to rob the oscillators of their individual behaviour. The overlayer behaves like a 2D phonon, with the IR excitation not localised on single molecules but shared between all the molecules on the surface. It is for this reason that hotbands ($v = 2 \leftarrow 1$) are not observed at high coverages. This distinction is clearly observed in the low and high coverage pump-probe data.

For a lattice of strongly coupled anharmonic oscillators, the spectra depend on the relative magnitude of the individual oscillator's anharmonicity x_e and the width of the one-phonon bandwidth W [120]. This is given by twice the dipole-dipole frequency shift, which is 35 cm^{-1} for CO/Ir{111} [72].

At low coverages, the anharmonicity is much greater than the phonon bandwidth ($x_e \gg W$) and the system behaves like uncoupled anharmonic oscillators. Saturation of the fundamental and the appearance of a hotband will be observed at high IR excitation intensities. At the other extreme, where $x_e \ll W$, the spectra resemble that of a harmonic lattice, showing no saturation or hotband at high IR excitation intensities.

For the adsorption of CO on Ir{111} the anharmonicity x_e is 13 cm^{-1}, as determined from low coverage hotband studies [35]. Under conditions such as these where $x_e \lesssim W$, Beckerle *et al.* [120] showed that the frequency shift of the fundamental can be given by $\Delta\omega(t) = -4x_eN(t)$, where $N(t)$ is the temporal dependence of the excited vibrational state population. For a plot of frequency shift versus pump-probe delay, a single exponential fit through the data points at positive delays should give a good measure of the T_1 time. This means that the recovery time of 2.4 ps for the frequency shift in Figure 4.17 is the T_1 time for $v = 1$ to $v = 0$ for CO on iridium {111}.

Conversion of the C-O frequency shift into a population change at $t = 0$ is

possible using $\Delta\omega(t) = -4x_eN(t)$. This gives a transient $v = 1$ excited state population of ~8 %. Using the two-level relationship presented by Harris *et al.* [114], $1 - (S_t/S_0)^{1/2} = (\Delta n_{v=1} - \Delta n_{v=0})$, where S_t and S_0 are the spectral intensities at delay time t and no pump, respectively. The intensity reduction at $t = 0$ gives a population change of 7 %. Unfortunately, this analysis takes no account of coherent effects and hence cannot account for the dip around $t = 0$.

The agreement between the two distinct models provides a good prediction for the extent of pump induced vibrational excitation (~7-8 %). However, the spectral intensity recovery as a function of pump-probe delay does not show the expected exponential recovery, as seen in Figure 4.17. This anomaly probably originates from the extensive broadening, which follows the same temporal profile as the frequency shift, and the coherent artefact around $t = 0$, which is observable as a dip in the spectra. The broadening cannot be quantified using the approach described by Beckerle, but was also observed in their study. It is attributed to faster dephasing as a function of population transfer, due to 2D lattice coherence effects not treated in Beckerle's model. The effects of power broadening were considered, but dismissed due to the relatively low population transfer involved (~8 %).

The spectral dip at $t = 0$ is attributed to interference between the pump and probe IR electric fields. Third order density matrix calculations performed elsewhere by Kato and Villaeys *et al.* have predicted the existence of a dip in IR pump-probe spectra [121–124]. Unfortunately slight differences between these calculations and our experiments (narrowband vs broadband probe pulses) make applying this approach non trivial. In their work it was suggested that the width of the dip gives the vibrational lifetime T_1. It is caused by the interference term of the fourth order polarisation, which is out of phase with the second order polarisation. As this interaction is only possible while both pump and probe fields are

overlapped in time, its spectral width is given by the lifetime T_1 rather than the dephasing time T_2. The dip observed experimentally in Figure 4.15 can be fitted with a width of 4.7 cm^{-1}, corresponding to a T_1 time of 2.3 -0.2/+0.8 ps, this is of similar magnitude to the T_1 value determined from the frequency shift.

T_1 comparisons

The first comparison is between the T_1 values for low and high coverages of CO on Ir{111}. The more robust measurement at low coverage (2.4 ps) is in perfect agreement with that at saturation (2.4 ps). This would confirm the common model for vibrational decay on metal surfaces via electron-hole pair creation, rather than intra-molecular or phonon energy decay pathways. As no other femtosecond broadband infrared pump-probe SFG experiments have been carried out, comparison must come from time-resolved RAIRS and picosecond IR pump-SFG probe experiments.

When the T_1 measurement presented herein is compared to other measurements in the literature, good general agreement is observed. The system Beckerle *et al.* studied was CO/Pt{111}, using a picosecond IR laser pump pulse and picosecond IR probe [120]. They observed a similar broadening and shifting of the fundamental C-O stretch and measured a T_1 time of 1.8 ps. The only other T_1 measurement for CO on a metal surface was Morin *et al.* who used picosecond IR pump-SFG probe to study CO/Cu{111}, measuring a T_1 time of 2 ps [49]. Both of these studies can be found lacking in both temporal and frequency resolution for this measurement. This was of course noticed at the time and is why the results of said measurements were generally published with error bars of the order of ± 1 ps.

While the IR pump-probe experiments have fulfilled their role in delivering a T_1 lifetime, it is felt that further theoretical modelling of the IR pump-probe tran-

sients would allow a better understanding of the coverage dependent vibrational dynamics and an improved understanding of the interference effects between IR laser fields at surfaces.

4.5 Conclusions

A full set of coherent and incoherent vibrational relaxation times for the model system of CO adsorbed on the Ir{111} surface at 100 K have been calculated. IR photon echoes have shown that the spectral linewidth (~5 cm^{-1}) in this strongly dipole-coupled system is dominated by lifetime broadening (2.7 cm^{-1}) and inhomogeneity (3.0 cm^{-1}), with only a small contribution from pure homogeneous dephasing due to coupling with low frequency modes. This has an important consequence for the use of adsorbates on metal surfaces in quantum computing [125]; the limiting factor for storing information will not be dephasing but the lifetime of the vibrational excitation, which can be tuned by changing the density of states at the Fermi level [126].

IR pump-probe experiments at low coverage have shown that vibrational ladder climbing processes at surfaces are possible using two femtosecond infrared laser pulses. This opens up the possibility of controlling a reaction via selective excitation of a molecular bond, a central focus for physical chemistry. While experiments such as this have been demonstrated in the gas phase [127], reaching high levels of excitation on a metal surface is harder due to rapid vibrational energy relaxation. An experimental approach that uses two laser pulses delayed in time with respect to each other, should be able to sustain high enough excitation intensities to compete with decay pathways.

Chapter 5

Reaction Dynamics

5.1 Introduction

This chapter brings together the 800 nm femtosecond pump probe experiments of CO and NO adsorbed on Ir{111} and looks at how the ultrafast dynamics change upon co-adsorption. The reactive combination of CO and NO on iridium is of considerable scientific interest, due to the activity of Ir as a catalyst for NO_x reduction in car exhausts [69]. In order to drive the development of commercial catalysts and improve their environmental performance, a sound knowledge of the fundamental reaction dynamics is needed. The surface science approach allows these problems to be dissected and their complicated reaction mechanisms to be unravelled.

5.1.1 NO_x Reduction

A major challenge in automotive catalysis at present is the ability to remove NO_x gases from energy efficient engines, such as diesel and lean burn engines. One of the challenges to producing working catalysts is the strong oxygen rich environment of exhaust emissions and poisoning by elements such as sulphur.

High levels of atmospheric NO_x can lead to increased levels of low level ozone (O_3), via the photo-catalysed oxidation of oxygen (equation 5.1.) Low level ozone has been linked with breathing difficulties and other health issues in cities all over the world [128].

$$NO_x + h\nu \longrightarrow NO_{x-1} + O \tag{5.1}$$

$$O_2 + O \longrightarrow O_3 \tag{5.2}$$

The NO found in exhaust gases is formed at high temperatures by the reaction of atmospheric nitrogen and oxygen and by the oxidation of nitrogen containing fuel additives. The main steps in the formation of NO are thought to involve:

$$N_2 + O \rightleftharpoons NO + N$$

$$N + O_2 \rightleftharpoons NO + O$$

$$N + OH \rightleftharpoons NO + H$$

Recently work has been carried out on the selective reduction of NO in the presence of O_2, over supported noble metal catalysts using either H_2 or CO as a reductant [69]. CO is a more practical reductant than H_2, as it can be easily produced using modern engine control software. Studies carried out by Ogura *et al.* [129] have shown that NO can be reduced by CO over Ir/silicate catalysts. Wang *et al.* [130] studied Pt, Pd, Rh, and Ir/ZSM-5 catalysts, with Ir showing the highest activity for NO reduction by CO in the presence of excess O_2. Work by Haneda *et al.* [131] found that Ir/SiO_2 catalysed NO reduction by CO and also found the reaction resistant to poisoning by SO_2, a feature of great importance for diesel engines. Iridium's reactivity in the form of nano-particles (e.g. 40-60 nm) on supported catalysts is quite surprising, considering that Ir bulk metals are not known for their high catalytic reactivity.

5.1.2 Coadsorption of CO and NO on Ir{111}

The adsorption of CO and NO independently has been discussed in previous chapters. There has been only one study into the coadsorption of CO and NO on the Ir{111} surface. Fujitani *et al.* have studied the adsorption of NO onto clean and CO pre-covered Ir{111}, using X-ray photoelectron spectroscopy (XPS), high resolution electron energy loss spectroscopy (HREELS), infrared refection absorption spectroscopy (RAIRS) and temperature programmed desorption (TPD) [132]. They showed that an initial precoverage of CO around 0.33 ML inhibits NO adsorption on atop sites, leaving the NO to adsorb in a three fold hollow site, inserted between the CO atoms. They also showed using TPD that upon heating the coadsorbed layer, some of the CO and NO reacts to form CO_2. Figure 5.1 shows TPD traces for mass 28, 30 and 44 (CO/N_2, NO, CO_2) for a 0.3 ML CO/NO layer on Ir{111}. This overlayer was formed by initially pre-dosing 0.3 ML of CO and then dosing 20 L of NO to fill the surface layer. This notation shall be used hereafter for CO and NO coadsorbed layers.

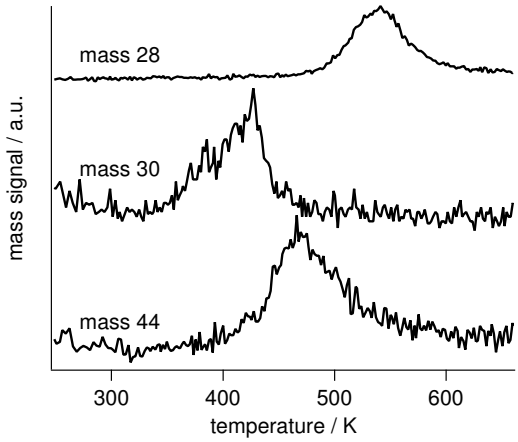

Figure 5.1: Multimass TPD for 0.3 ML CO/NO on Ir{111}. The y-axis does not give absolute magnitude.

5.2 Experimental

The experimental setup is essentially the same as for the separate NO and CO pump probe experiments as described in Chapter 3. An 800 nm pump beam is used to heat the surface, with a fluence between 10-20 Jm^{-2}. The C-O bond frequency is then probed after short delay with a frequency resolved SFG probe pulse pair. The only difference is that the atop CO is coadsorbed with hollow site NO. The other difference to the experiments conducted in Chapter 3, is that the crystal base temperature is 200 K as opposed to 100 K. The temperature was changed as it was observed that the transient effects are more pronounced at an elevated temperature. This is due to an improvement in the temporal resolution as the linewidth increases with temperature.

A pre-coverage of CO was dosed on to the surface and a series of pump probe delays measured. The fluence of the pump beam can then be calculated by following the C-O frequency shift at long pump-probe delays. This is done using the experimentally determined temperature gradient for CO and the lattice temperature calculated from the two-temperature model introduced in Chapter 3. This is based upon the premise that CO/Ir{111} is only heated by the metal lattice and not the electrons, due to the inaccessibility of the CO $2\pi^*$d antibonding orbital to hot metal electrons.

The CO layer is then filled up with a 20 L saturation dose of NO. The largest effects are observed when the CO pre-coverage is small, however this also corresponds to the lowest signals, making experiments difficult. The NO adsorbed in hollow sites cannot be detected by SFG due to its small signal, hence only the C-O frequency is probed as a function of 800 nm pump-SFG delay.

5.3 Results

5.3.1 SFG of CO/NO coadsorption

Figure 5.2(a) shows the effect of adding NO to a pre-adsorbed 0.3 ML ($\sqrt{3} \times \sqrt{3}$) overlayer of CO on the Ir{111} surface. Upon NO co-adsorption with CO, the C-O frequency increases and the SF intensity is dramatically reduced. The origin of the frequency shift and reduction in intensity shall be discussed later in Section 5.4.

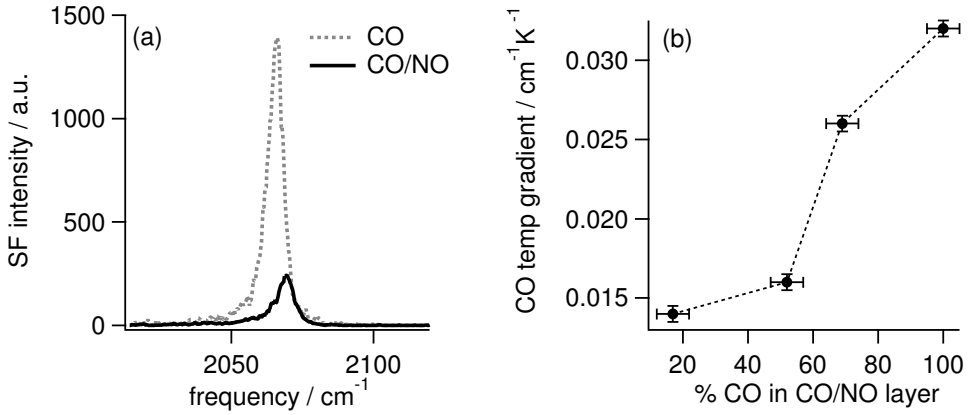

Figure 5.2: (a) CO SF spectra of 0.3 ML CO and mixed 0.3 ML CO/NO layer at 200 K. Upon adsorption of NO the CO SF peak is shifted to higher frequencies by ~4 cm^{-1} and dramatically reduced in intensity. (b) Gradient of CO frequency shift with temperature for different CO/NO mixtures on the surface.

Figure 5.2(b) shows the change in thermal C-O frequency shift gradient as a function of percentage CO in the CO/NO mixed layer. The gradient reduces by a factor two from the saturated CO value of 0.032 to 0.014 cm^{-1}/K^{-1} at 0.1 ML CO/NO overlayer (19% CO in NO). These values compare to a N-O temperature gradient of 0.051 cm^{-1}/K^{-1} for a saturated layer of NO on Ir{111}.

5.3.2 Time Resolved Experiments

Figure 5.3 shows the C-O frequency shift and width for a 0.3 ML CO/NO overlayer, with a pump fluence of 15 Jm^{-2}. Both the frequency shift and width show changes on two time scales, in a similar manner to NO/Ir{111}. A fast change that decays in under 10 ps is observed around $t = 0$, and then a slower phonon like decay is observed out to 60 ps. The frequency shifts by nearly 6 cm^{-1}, compared to a 3 cm^{-1} shift for CO on its own at this fluence. The width nearly doubles, increasing from 5 cm^{-1} to just over 9 cm^{-1}.

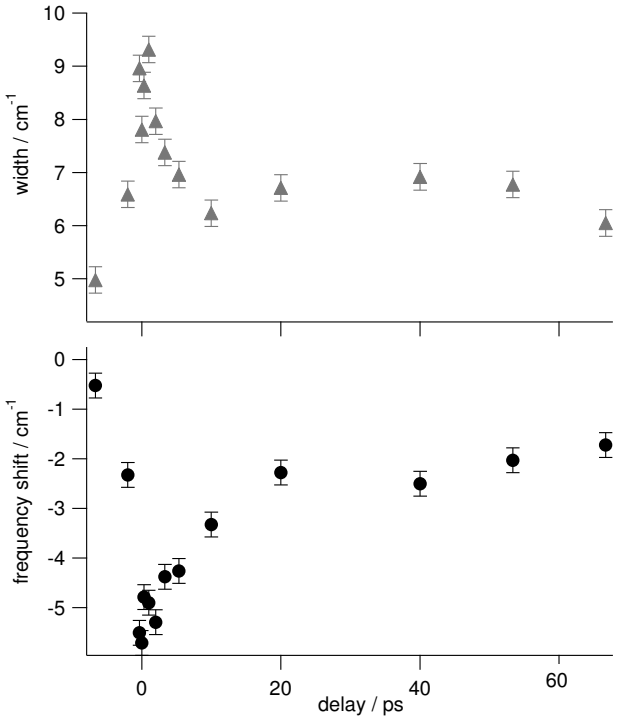

Figure 5.3: Plot of CO frequency shift and width for a 0.3 ML CO/NO mixed layer as a function of 800 nm pump-SFG probe delay at 200 K. Pump fluence is 15 Jm^{-2}.

Temporal Profile

The frequency changes of CO coadsorbed with NO are faster than CO adsorbed on its own, but slower than the frequency changes for NO on its own. The difference in temporal profile between the three types of scaled transients can be seen in Figure 5.4. The CO/NO experimental results are plotted with the modelled transients for CO and NO under similar conditions. Although the CO/NO transient is intermediate in temporal profile with CO and NO, it can be seen in the inset to Figure 5.4 that the NO frequency shift is still much larger in magnitude.

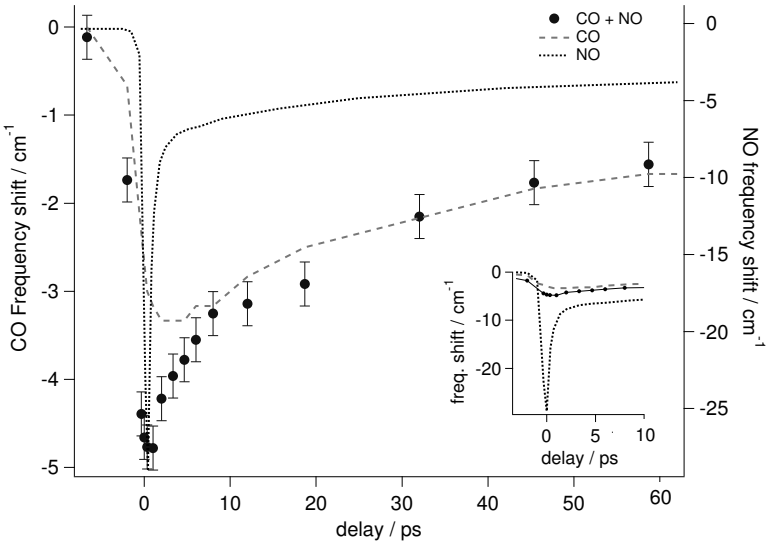

Figure 5.4: Plot of CO frequency shift for 0.4 ML CO/NO mixed layer against 800 nm pump-probe delay at 200 K. Added for temporal comparison are the calculated frequency shifts for individual saturated CO and NO layers at 15 Jm^{-2} absorbed fluence. The frequency shifts for CO/NO and CO are plotted on the left hand axis and NO on the right hand side. The inset shows the relative changes in magnitude for CO, NO and CO/NO.

Coverage Dependence

In a simple static SFG experiment (Figure 5.2(a)), a higher coverage of NO on the surface compared to CO gives a larger C-O frequency shift and a bigger decrease in SF intensity. Experiments are therefore a compromise between observing the largest transient effects and having sufficient signal.

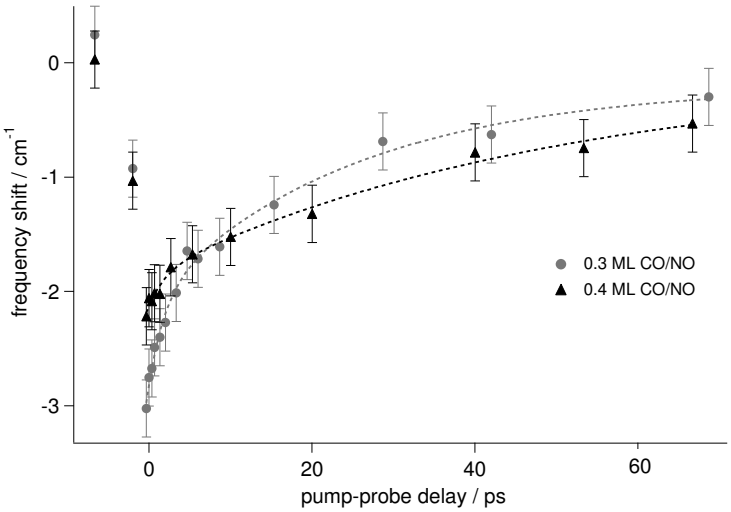

Figure 5.5: CO frequency shift as a function of pump-probe delay, at a constant fluence of 11 Jm^{-2}, but for different ratios of CO and NO on the surface. The dashed lines are to guide the eye.

Figure 5.5 shows the pump probe transients for two coverages of precovered CO/NO. The layer with more NO adsorbed shows a larger C-O frequency shift around $t = 0$ and a quicker temporal decay over a timescale of tens of picoseconds. The larger shift at $t = 0$ is attributed to effects directly related to the coadsorbed NO, the exact nature of this interaction shall be discussed later. The quicker decay is due to the reduction in the thermal frequency shift gradient, as displayed in Figure 5.2(b).

Fluence Dependence

The shape of the transients show a fluence dependence in an analogous fashion to NO/Ir{111}, although not quite as dramatic. Figure 5.6 shows the transients for two fluences at a constant CO/NO coverage. Although the low fluence transient does still have a sharp profile around $t = 0$, this becomes much more obvious at higher fluence.

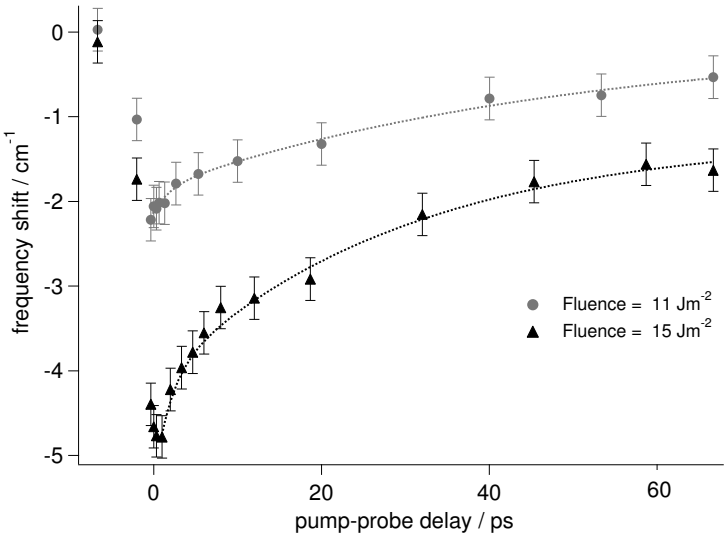

Figure 5.6: C-O frequency shift as a function of 800 nm pump-SF probe delay, for a 0.4 ML CO/NO coadsorbed layer on Ir{111}. The dashed lines are a guide to the eye.

The frequency shift at $t = 0$ and $t = 15$ ps was followed in a similar way to the fluence dependence of CO and NO adsorbed individually in Chapter 3. In Figure 5.7 it can be seen that the C-O frequency shift and width are not linear at $t = 0$, suggesting that the C-O bond perturbation is somehow dependent upon the metal electron temperature.

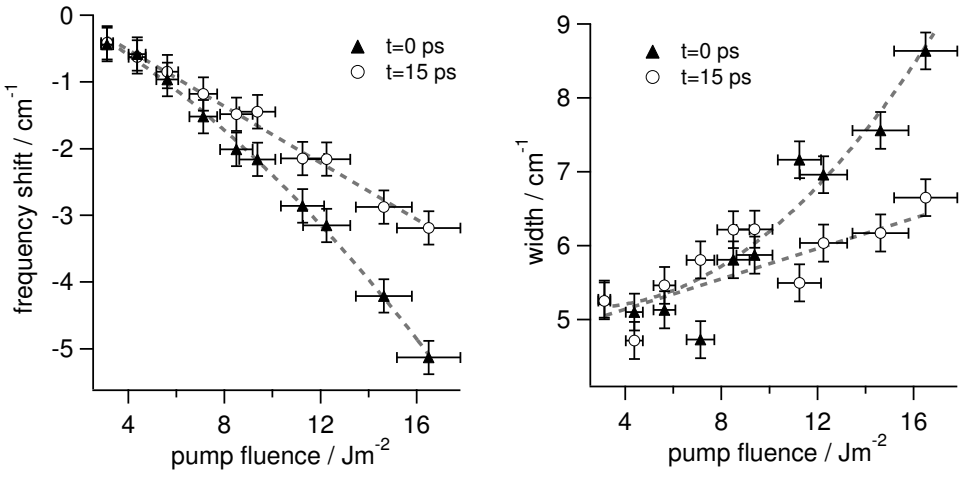

Figure 5.7: C-O frequency shift and width (FWHM) as a function of 800 nm pump fluence, at t = 0 and t = 15 ps pump-probe delay times. For an 0.4 ML CO/NO coadsorbed layer. The dashed lines are to guide the eye.

5.4 Discussion

The following discussion shall be divided up into the following sections. Initially I shall review the SFG experimental results for CO and NO coadsorbed onto the Ir{111} surface and compare them to the results discussed earlier in Chapter 3 for CO and NO adsorbed individually. Then I shall endeavour to explain the origin of the frequency shift and intensity reduction for CO, upon addition of NO to the surface. Finally I shall look at the physical reasoning behind the nature of the pump-probe transients and look at their implications on understanding the dynamics of NO reduction by CO on the Ir{111} surface.

5.4.1 Experimental Review

Upon addition of NO to a CO precovered Ir{111} surface ($\leq$ 0.4 ML), the C-O frequency shifts to higher frequency and the SF intensity is reduced. These effects are most prominent when the ratio of NO to CO on the surface is greatest. When the mixed CO/NO layer is pumped with a femtosecond 800 nm laser pulse the C-O frequency shifts to the red by maximally 6 cm^{-1} and the width nearly doubles. These changes decay over two time scales, the first of which is quicker in nature and finished within 10 ps after the pump pulse, the second timescale is much slower and decays over tens of picoseconds.

This slow "thermal" decay over tens of picoseconds is exactly the same as observed for both CO and NO adsorbed individually on Ir{111} . The faster decay bears no resemblance to either the CO or NO pump-probe transients. It is faster than CO, which decayed slowly over tens of picoseconds, but slower than NO, where the fast change around $t = 0$ was over within $\pm$ 2 ps. The fast change around $t = 0$ for CO/NO also exhibits a non-linear fluence dependence for both the frequency shift and width changes (Figure 5.7). Whereas the longer decay changes linearly with fluence, as observed previously for CO and NO individually at long time delays. The magnitude of the transient changes for CO/NO are also strongly dependent upon the ratio of CO:NO on the surface.

5.4.2 Analysis

Frequency Shift and Intensity Reduction

The frequency shift is attributed to the addition of an electronegative adsorbate to the surface. This withdraws electron density from the metal, reducing available electron density for back-donation to the CO $2\pi^*$ orbital. This weakens the Ir-CO bond and strengthens the C-O bond, thus the C-O bond frequency is increased

upon NO adsorption. Weakening the Ir-CO bond also reduces the frequency of the frustrated translation, hence the gradient of the static temperature frequency shift is also reduced (Figure 5.2(b)).

The reduction in SFG intensity could be due to two factors. The first is that the addition of NO to the CO overlayer leads to steric repulsion between adsorbates, causing the CO to tilt. This reduces the component of the molecular dipole perpendicular to the surface, hence reducing the molecular SF IR cross section at the surface. The second possibility is that the SF Raman cross section has been reduced due to electronic changes induced by NO adsorption. This has been attributed to other cases where the SF intensity has been significantly reduced upon coadsorption.

When CO is adsorbed on Ni{111}, adsorption is initially at bridge sites and a strong SFG signal is observed at 1920 cm^{-1}. Upon further exposure adsorption at atop sites is also observed, and a strong SFG signal develops at 2074 cm^{-1}, at the expense of the low frequency bridge peak. As these species are too far apart for intensity stealing via dipole coupling, suppression of the bridge CO signal was attributed to a reduction of the Raman tensor involved in the SFG process. This was caused by surface electronic changes brought about by coadsorption. These changes are not observed for RAIRS spectra on the same surface, hence a geometry change was ruled out in this case [133].

Temporal Deconvolution

The added complexity of having two adsorbates on the surface makes it difficult to construct a modelling approach that is not purely phenomenological or computationally expensive. One of the problems facing the current analysis is the lack of knowledge about the co-adsorbed NO molecules (not detectable with the SFG probe) and what effect the NO has electronically on the Ir-CO bond.

A feature common to both CO and NO 800 nm pump-probe transients is the slow thermal heating and cooling due to the metal lattice. Independent of the molecule's electronic structure, at temperatures above 0 K the high frequency intermolecular bond will always be perturbed by anharmonic coupling with low frequency modes. These modes, such as the frustrated translation are populated thermally via the lattice phonons. In order to try and isolate the nature of the fast change observed between $t = 0$ and $t = 10$ ps in the CO/NO transients, the thermal background can be subtracted. This can be done as long as the static frequency shift temperature gradient (Figure 5.2(b)) and the fluence are known. The fluence is calculated from the C-O shift at long pump-probe delays, when only CO is adsorbed on the surface.

This background subtraction has been carried out and the result plotted in Figure 5.8. The remaining shift around $t = 0$ is then fitted for positive delay times

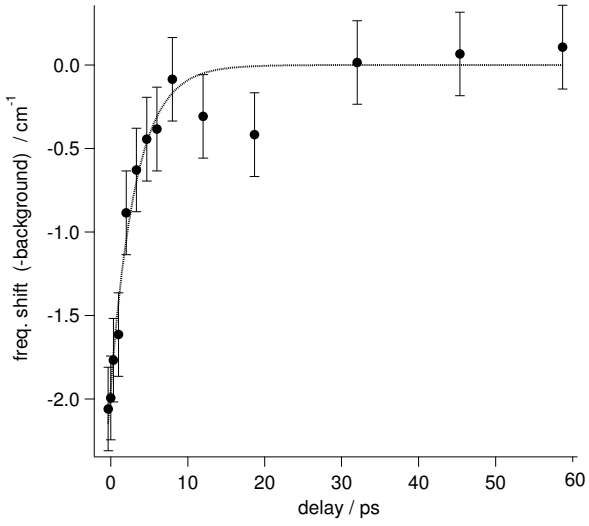

Figure 5.8: CO/NO frequency shift following subtraction of lattice background. The remaining fast change is fitted with an exponential to yield a decay time of 3.3 ± 0.4 ps. A 0.4 ML CO/NO mixture on Ir{111} and absorbed fluence of 15 Jm^{-2}.

with an exponential decay, yielding a lifetime of 3.3 ± 0.4 ps. This timescale is intermediate in nature, when compared to the frequency changes for atop NO in the saturated layer, where the NO reacts to the hot electron distribution within 700 fs.

At this point, it is worth considering the action of the Bloch equations for changes occurring over this sort of time scale. The averaging induced by integrating over the free induction decay will be negligible, as the time scale of the effects are longer than the T_2 time. Hence, although this approach is obviously not as satisfactory as using the Bloch equations to model the transient changes, it does hold a certain degree of substantiality.

While measuring this lifetime alone cannot totally determine the mechanism responsible for the observed spectroscopic transients, it does greatly narrow down the possible explanations. This is because the time scale of many processes on surfaces are either slower or considerably faster than 3 ps.

Reaction Dynamics

Before considering the reaction dynamics of the situation, I shall consider what is known about the participants in the CO/NO system.

From previous spectroscopic studies it is known that when CO occupies atop sites on Ir{111}, NO adsorbs on hollow sites within the CO overlayer (Figure 5.9). When the coadsorbed layer is heated slowly, some of the CO and NO react to form CO_2 (Figure 5.1). For the saturated NO layer, NO is adsorbed at both atop and hollow sites and the hollow site NO is bent, with an Ir-N-O angle of 130° [87].

It has been demonstrated in Chapter 3 that for atop NO in a saturated layer, ultrafast heating with a femtosecond heating pulse causes the NO to interact strongly with the hot metal electrons. Over a time scale of 700 fs this interaction causes the NO to bend over relative to the surface, weakening the Ir-NO and N-O bond. For

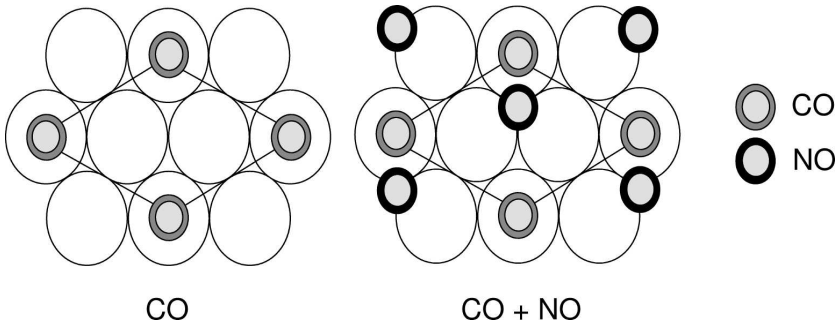

Figure 5.9: Surface structures of 0.33 ML ($\sqrt{3} \times \sqrt{3}$) CO and 0.33 ML CO co-adsorbed with NO. The coverage and adsorption site for NO have been determined from XPS and RAIRS previously [132].

atop CO in a saturated layer ($2\sqrt{3} \times 2\sqrt{3}$), the $2\pi^*$d antibonding orbital is too far above the Fermi level for the hot electrons to reach. Hence, CO is only perturbed by lattice heating via coupling with low frequency modes.

Finally and most importantly, when CO is co-adsorbed with NO, femtosecond heating with an 800 nm pump causes the C-O frequency and width to be perturbed over a time scale of 3 ps. This time scale is intermediate in nature when compared to other surface processes and shows a non-linear fluence dependence, suggesting involvement of the hot metal distribution.

Some possible causes of the CO/NO transient behaviour can now be discarded. In particular the direct excitation of hot metal electrons into a lowered CO $2\pi^*$d orbital is very unlikely, as the response time for CO to this would be more akin to the 700 fs as measured for NO. It is therefore considered that the only way for the C-O bond to be perturbed by the hot metal electrons is via an interaction with the NO. This would require the hollow site NO to behave in an analogous fashion to atop NO when exposed to a hot metal electron distribution. As the NO $2\pi^*$d orbital is transiently populated with hot electrons, the hollow site NO can bend over and interact with the CO, which is in a neighbouring atop site.

At this point a lack of knowledge regarding the starting geometry for the hollow site NO proves to be an issue. Is it bent to start with and if so in which direction? If it were similar to the hollow site NO in the saturated 0.5 ML NO layer, then it would be substantially bent over to start with. However, the differences between the overlayers does demand a cautionary approach into making too quantitative comparisons. If it were the case that the NO was bent over pointing away from the CO, to reduce repulsion between adsorbates, the oxygen from the NO would be too far away from the carbon of the CO. It is therefore more likely that the NO is upright or bent over towards the CO.

It is concluded that the measured lifetime of 3 ps for the transient change in C-O bond character, reflects the lifetime of the hollow site NO bending over and interacting with the CO. The nature of this interaction between N-$\bar{O}$ and $\bar{C}$-O can be identified with their approach on the reaction potential energy surface and the oxygen (δ^-) interacting with the carbon (δ^+) of the CO. The shift in frequency of the C-O to lower frequencies identifies the partial CO_2 character of the C-O bond during the approach to the transition state. The frequency of CO_2 intermediates on other surfaces have been observed using RAIRS at around 1600 cm^{-1} [134].

5.4.3 Future Modelling

With a more advanced modelling approach, the fundamental parameters and lifetimes, as described by transition state theory should be able to be deduced from these experimental results. The way to benchmark these results is to carry out a set of DFT calculations. The first stage in such a calculation would aim to describe the geometry and electronic structure of the CO/NO co-adsorbed structure. These structures could then be compared to the results of a LEED-IV study, to pinpoint the molecular position at equilibrium conditions.

The second part of the DFT calculation would try and look at the geometry

and electronic structure when the system is not in equilibrium. These conditions would reflect the molecular behaviour during the period when metal electrons and lattice are out of thermal equilibrium. Although DFT calculations are usually run at 0 K, it is possible to run the calculations at elevated electron temperatures [135].

5.5 Conclusions

The adsorption of CO and NO onto the Ir{111} surface leads to a coadsorbed structure, which reacts upon static heating to form CO_2. When heated with an 800 nm femtosecond laser pulse, the initial stages of this reaction mechanism can be probed by following the frequency of the C-O bond with pump-probe SF spectroscopy. The NO $2\pi^*$d antibonding orbital is transiently populated by the metal hot electrons. This causes the NO molecule to bend over and the N-O bond to weaken. At this point it is observed that the C-O bond is perturbed by the NO bending. The nature of this perturbation has been attributed to an ultrafast reaction intermediate, with a lifetime of 3 ps. This is an intermediate in the NO reduction reaction to form CO_2, which involves fission of the N-O bond and formation of a C-O bond. This is the first experimental evidence for an ultrafast reaction transition state on a metal surface. The long lifetime of this intermediate demonstrates the attractive nature of the potential energy surface for this reaction.

Chapter 6

Summary and Outlook

6.1 Thesis Review

The work presented here on molecular (Chapters 3 and 5) and vibrational dynamics (Chapter 4) has significantly advanced the drive to study reaction dynamics on metal surfaces. At a relatively basic level this is represented by carrying out pump-SF probe experiments with NO as an adsorbate, as opposed to CO. Although this may sound trivial, the corresponding loss in SF signal makes already difficult experiments very challenging. At a more complex level, the theory introduced in Chapter 3 provides a new way to describe non-adiabatic pump-probe experiments and allows the NO/Ir{111} system to be treated as a model system for non-adiabatic processes at surfaces.

Following the results in Chapter 4, the possibility of driving molecular bond cleavage by vibrational ladder climbing is considered an excellent route for further work. Such population transfer schemes in the gas phase have led to some fascinating results [58] and would completely open up the area of bond selective chemistry at surfaces. It is felt that with a infrared pump-SF probe arrangement and the addition of pulse shaping technology, excitation pathways will be able to

compete with the rapid decay channels on metal surfaces.

An extension of this work would include the use of two colour IR-IR-VIS SFG to study the coupling between identical oscillators on different surface sites, isotope mixtures and oscillators of different chemical identity, e.g. CO and NO. In this 2D experiment, one species is vibrationally excited by one IR pulse, and the amount of vibrational energy transfer to other oscillators and its time scale can be monitored by a time-delayed IR pulse of a different colour. The experimental set-up in Cambridge is ideally suited to such an experiment as both pump and probe infrared pulses can be individually scanned in frequency, using their own respective OPAs. These experiments could be conducted using CO and NO on a range of surfaces, including Ru, Pt, Ag, Au and Ir. On the Ir surface, the study of the NO-CO coupling will be a valuable addition to RAIRS studies on the oscillatory NO-CO reaction. 2D time-resolved IR spectroscopy can provide unique information on molecular interactions for many important coadsorbed systems.

The results presented in Chapter 5 represent the most exciting experiments in surface reaction dynamics of the last decade. Although the level of advancement is still significantly behind that of gas phase studies, a major step forward has been made by observing the courting of CO and NO on the lower slopes of the reaction potential energy surface. This was only made possible by the advances made in experimental approach, as described in Chapters 3 and 4. The extended interpretation of these results will rely upon further DFT calculations, carried out in collaboration with theory groups here in Cambridge and in China.

To progress to the next level, experiments will have to advance even further. The main problems faced in the introduction of SFG probed surface reactions are those of sensitivity, adsorbate uniformity and of refreshing the crystal with new reactants while accumulating spectra. The final point is possibly the most challenging and has been initially addressed using two different approaches in

Cambridge. The first looked at scanning the crystal, to provide a fresh surface for each pump laser pulse and the second involves using a fourth cleaning pulse to desorb any unwanted reaction products. After further consideration it was felt that the second of these approaches was more technically feasible and preparations for trialling the additional cleaning pulse in SFG studies are currently underway. This has involved the addition of another Nd:YAG laser to the experiment and the construction of another beam pathway into an already crowded UHV chamber.

6.2 From Surface Science to Real Life?

Studies of adsorbates at single crystal surfaces in UHV are unparalleled in the degree of experimental control and attainable knowledge of the details of each chemical reaction, leading to a fundamental understanding that can be used to develop catalysts from first principles. While such fundamental understanding is highly desirable, transfer of this knowledge to *real life* situations over the so-called pressure and materials gaps is often difficult, partly hampered by a dearth of suitable techniques to study catalysts under working conditions.

While I have made it clear in the introduction of this thesis that my work makes no attempt to bridge the gap between surface science and real catalytic systems', we have carried out some basic experiments in collaboration with Dr. Frederic Thibault-Starzyk, CNRS, Caen on more complicated systems. This involves triggering a chemical reaction on a supported catalyst with a femtosecond pump pulse and monitoring the progress of the reaction with step-scan FTIR spectroscopy. Initial experiments were conducted in 2004, when Dr. Thibault-Starzyk brought his step scan FTIR spectrometer over from France. The basic set-up was verified and found to work down to a time resolution of 33 ns, in addition laser-induced changes in the reaction of CO + NO on Ag/Al_2O_3 were observed. Further exper-

iments using this system are planned and would enable the ultrafast dynamics of *real* catalyst systems to be studied in Cambridge.

6.3 Conclusions

The results presented in this thesis represent the highest refinement possible for the current experimental set-up. It will therefore require further technical upgrades and the correct choice of chemical system, for further improvements to be made. However, the importance of surface catalytic systems in everyday life and their role in developing our future energy strategy will ensure that this field will continue to evolve and develop strongly.

Appendix A

Modelling VIS-Pump-SFG Probe Spectra

Laser Heating of Metal Surfaces

Modelling of laser-induced surface heating is based upon the two temperature model, which is used extensively in the literature and was initially proposed by Anisimov *et al.* [136]. This involves numerically solving the following coupled differential equations [137]:

$$C_{el}\frac{\partial T_{el}}{\partial t} = \kappa\nabla^2 T_{el} + g\left(T_{ph} - T_{el}\right) + S\left(z,t\right) \tag{6.1}$$

$$C_{ph}\frac{\partial T_{ph}}{\partial t} = -g\left(T_l - T_{el}\right), \tag{6.2}$$

where T_{el} and T_{ph} are the electron and lattice temperatures, κ the thermal conductivity, C_{ph} the lattice heat capacity (equation 6.3), $C_{el} = \gamma T_{el}$ is the electronic heat capacity where γ is the coefficient of the electronic specific heat, g the electron-lattice coupling constant (equation 6.4 [138]) and $S\left(z,t\right)$ is the laser source term (equation 6.5).

$$C_{ph} = 9nk_B\left(\frac{T_{ph}}{\Theta_D}\right)^3 \int_0^{\Theta_D/T_{ph}} \frac{x^4 e^x}{\left(e^x - 1\right)^2}\, dx, \tag{6.3}$$

where Θ_D is the Debye temperature and n the atom density.

$$g = -\frac{3\hbar\gamma}{\pi k_b}\lambda\langle\omega^2\rangle, \tag{6.4}$$

where λ is the electron-phonon coupling constant used in superconductivity theory and $\langle\omega^2\rangle$ the second moment of the phonon spectrum

$$S\left(z,t\right) = 2I\left(t\right)\left(1-R\right)\frac{\exp(-2z/\delta)}{\delta}, \tag{6.5}$$

where $I(t)$ is the laser intensity as a function of time, R is the substrate reflectivity, z is the depth of the substrate and δ is the optical skin depth. A summary of the parameters used to calculate the optical heating of iridium are given in table 6.1.

Coefficient of electron specific heat [139]	γ	0.0031	$JK^{-2}mol^{-1}$
Lattice heat capacity	C_{ph}	0.131	$Jg^{-1}K^{-1}$
Debye temperature	Θ_D	430	K
Second moment of phonon distribution [140]	$<\omega^2>$	342.83	meV^2
Superconductivity e-ph coupling constant [141]	λ	0.45	
Electron-phonon coupling constant	g	$9.43 \cdot 10^{16}$	$Wm^{-3}K^{-1}$
Reflectivity at 800 nm and 62° incidence angle	R	0.51	
Optical skin depth at 800 nm	δ	24.4	nm

Table 6.1: Parameters used for calculating optical heating of Ir{111} with an 800 nm 150 fs laser pulse.

Generating SFG Spectra

The approach used to model SFG spectra in Chapter 3 uses the Density Matrix formalism [11, 12]. While a full explanation of this treatment is beyond the scope of this current work, I shall try to cover the basic principles here.

The density matrix framework provides a way to statistically model the quantum mechanical behaviour of a system and hence calculate the expectation value of any observable quantity. The temporal evolution of the density matrix operator $\hat{\rho}(t)$ can be represented as the Hamiltonian $\hat{H}$ for the time dependent Schrödinger

equation.

$$\begin{aligned} i\hbar\frac{\partial\hat{\rho}}{\partial t} &= \hat{H} \\ i\hbar\frac{\partial\psi_s(\mathbf{r},t)}{\partial t} &= \hat{H}\psi_s(\mathbf{r},t), \end{aligned} \tag{6.6}$$

where $\psi_s(\mathbf{r},t)$ is the wavefunction for a particular quantum mechanical state s as a function of space and time. Upon interaction with an electromagnetic field $\hat{H}$ can be split up into time dependent and independent components:

$$\hat{H} = \hat{H}_0(\mathbf{r}) + \hat{V}(t), \tag{6.7}$$

where $\hat{H}_0$ is the operator for the time independent Schrödinger equation ($\hat{H}_0\psi = E\psi$) and hence represents the energy of the system at rest and $\hat{V}(t)$ represents the energy of the interaction with the electric field. The interaction Hamiltonian $\hat{V}(t)$ is given by the electric dipole approximation:

$$\hat{V}(t) = -\hat{\mu}E(t). \tag{6.8}$$

For a two level system with ground and excited energy levels 0 and 1 respectively, the density matrix operator $\hat{\rho}(t)$ is:

$$\hat{\rho}(t) = \begin{bmatrix} \rho_{00} & \rho_{01} \\ \rho_{10} & \rho_{11} \end{bmatrix} \tag{6.9}$$

The elements of the density matrix $\rho_{00}, \rho_{11}, \rho_{01}$ and ρ_{10} have the following physical interpretation. Diagonal elements are directly related to the population of the resonant levels and the off-diagonal elements give the coherence between these levels. These coherences refer to a superposition of states between the two levels and can be related to an infrared transition between the two levels [12]. The polarisation generated by an infrared field can be given by:

$$\mathrm{P_{IR}}(t) \propto \mathrm{tr}\left[\hat{\rho}(t)\hat{\mu}\right], \tag{6.10}$$

where $\hat{\mu}$ is the electric dipole operator and the the trace of a matrix is given by the sum of the diagonal components [11].

To model the observed SF infrared spectrum $I_{SF}(\nu)$, the surface IR polarisation $P_{IR}(t, \tau)$ is Fourier transformed with the envelope of the picosecond visible field $\bar{E}_{vis}(t)$. This gives the experimental broadening associated with the finite width of the visible upconversion process.

$$I_{SF}(\nu) \propto \left| \int \bar{E}_{vis}(t) \cdot P_{IR}(t, \tau) e^{-2\pi\nu t} dt \right|^2. \tag{6.11}$$

$P_{IR}(t, \tau)$ is calculated using the optical Bloch equations, which describes the temporal evolution of the density matrix. To model pump-probe experiments and take account of coherent effects around $t = 0$, SF spectra need to be calculated at various pump-probe delays. This can be achieved by using the instantaneous frequency ν(t) and linewidth Γ(t) as defined in section 3.4 as an input to the optical Bloch equations. As ν(t) and Γ(t) have been defined as a function of metal lattice (T_{lat}) and electron temperatures (T_{el}), it can be seen from the two-temperature model that they are therefore also related to time. As the IR polarisation P_{IR}(t) is strongly dependent on the time dependent perturbation of the frequency $\nu(t)$ and linewidth $\Gamma(t)$ imposed by the pump, P_{IR}(t) is also a function of the delay τ between pump (E_{pump}) and probe (E_{probe}) pulses.

To describe the time-dependent evolution of the density matrix $\hat{\rho}(t)$, including the temporal profile of ν(t) and Γ(t) and allowing for dephasing. The optical Bloch equations are solved by direct integration using the Runge-Kutta method [27]:

$$\frac{du}{dt} = \bar{\nu}(t-\tau)v - \frac{u}{\Gamma(t-\tau)} \tag{6.12}$$

$$\frac{dv}{dt} = -\bar{\nu}(t-\tau)u - \frac{v}{\Gamma(t-\tau)} + \kappa E_{IR}(t)w \tag{6.13}$$

$$\frac{dw}{dt} = -\frac{f - f_0}{T_1} - \kappa E_{IR}(t)v, \tag{6.14}$$

where the off diagonal density matrix elements are given by $\rho_{10} = u+iv, \rho_{01} = u - iv$

($\rho_{10} = \rho_{01}^*$), and the population difference is $f = \rho_{11} - \rho_{00}$. $\bar{\nu}(t)$ and $\Gamma(t)$ are the instantaneous frequency and linewidth at time t and provide the system dependent input to the Bloch equations. The vibrational decay and dephasing parameters T_1 and T_2 are given by IR pump-probe and free induction decay experiments. κ is the field coupling constant, estimated to be $2D/\hbar$.

Equations 6.12–6.14 are solved for each value of τ, where the initial values are $u_0 = v_0 = 0$ and $f = f_0 = -1$. Given that the on-diagonal elements of $\hat{\mu}$ are zero, and the off-diagonal elements are mutually conjugate, $P_{IR}(t) \propto u(t) - v(t)$.

Appendix B

Modelling IR Pump-Probe Experiments

The modelling used to fit the experimental results for infrared pump-SFG probe experiments follows closely the analysis presented by *Joffre* in Chapter 9 of [115]. Rather than trying to solve the temporal evolution of the density matrix with a numeric approach (such as the Runge-Kutta method), it is possible to use Green functions. This greatly simplifies modelling and allows for the inclusion of multiple infrared interactions by the system. Using this approach the density matrix operator is given by:

$$\rho_{nm}(t) = G_{nm}(t) \otimes \left(E(t) \sum_{l} [\mu_{nl}\rho_{lm} - \rho_{nl}\mu_{lm}] \right), \tag{6.15}$$

where $G_{nm}(t)$ is a Green function, which is given by:

$$G_{nm}(t) = \frac{i}{h}\Theta(t) exp(-i\omega_{nm}t - \Gamma_{nm}t), \tag{6.16}$$

where Θ is the Heavside function and Γ_{nm} allows for relaxation. Γ_{nm} is a dephasing rate when $n \neq m$ and population decay when $n = m$. According to *Joffre* [115], the Green function can be physically interpreted as the impulsive response function of the material, where the density operator is simply the convolution product of this response function and a source term. The Green functions for the diagonal matrix elements give the population and non-diagonal the coherences.
For a two level system the coherence are connected to the population by:

$$\rho_{10}(t) = \mu_{10} G_{10}(t) \otimes \left\{ E(t)[\rho_{00}(t) - \rho_{11}(t)] \right\}, \tag{6.17}$$

and the popultaion terms to the coherences by:

$$\rho_{11}(t) = G_{11}(t) \otimes \Big\{E(t)[\mu_{10}\rho_{01}(t) - \rho_{10}(t)\mu_{01}]\Big\}. \tag{6.18}$$

Hence, when starting with the system at equilibrium ($\rho_{00}^{(0)} = 1$), the first order density matrix coherence $\rho_{10}^{(1)}(t)$ (one IR photon interaction), second order population $\rho_{11}^{(2)}(t)$ (two photons) and the third order coherence terms $\rho_{10}^{(3)}(t)$ (three photons) are:

$$\rho_{10}^{(1)}(t) = \mu_{10}G_{10}(t) \otimes E(t) \tag{6.19}$$

$$\rho_{11}^{(2)}(t) = -|\mu_{10}|^2 G_{11}(t) \otimes \Big\{E(t)[\{G_{10}(t) + G_{01}(t)\} \otimes E(t)]\Big\} \tag{6.20}$$

$$\begin{aligned}\rho_{10}^{(3)}(t) = 2\mu_{10}^2\mu_{01}G_{10}(t) \otimes \Big\{E(t)\Big[G_{11}(t) \otimes \Big(E(t) \\ \{[G_{10}(t) + G_{01}(t)] \otimes E(t)\}\Big)\Big]\Big\},\end{aligned} \tag{6.21}$$

where $\rho_{10}^{(1)}(t) = -\rho_{01}^{(1)}(t)$, $\mu_{10} = -\mu_{01}$ and the second order population difference is given by $\rho_{00}^{(2)} - \rho_{01}^{(2)} = -2\rho_{11}^{(2)}$.

In an IR pump-SFG probe experiments there are now two sources of infrared photons. The two pulses pump and probe shall now be referred to as pump $E_P(t)$ and test $E_T(t)$ pulses in the following equations, for easier nomenclature. Only the SFG generated down the test path is detected. Hence any signal observed will correspond to either a single interaction with the test pulse or two with the pump and one with the test, such that $\mathbf{k}_{SFG} = \mathbf{k}_T + \mathbf{k}_P - \mathbf{k}_P$. This interaction can be given when the total electric field is:

$$\mathbf{E}(t) = E_T(t) + E_P(t) + E_P^*(t).$$

This gives three contributions to the third order density matrix, named sequential [TPP], interference [PTP] and perturbed FID [PPT]. The sequential term corresponds to the classical interpretation of pump-probe experiments (read in reverse order). This involves the pump pulse changing the population of the system (requiring two photons) and the probe pulse probing the remaining population in

$v = 0$. The pump pulse must interact with the system twice to create a population change, before the probe pulse interacts.

$$\rho_{10}^{(3)}[\mathrm{TPP}](t) = \frac{\mu_{10}}{2} \underbrace{G_{10}(t) \otimes \Big\{E_T(t)}_{\text{probe photon}} \underbrace{\Big[\rho_{00}^{(2)PP}(t) - \rho_{11}^{(2)PP}(t)\Big]}_{\text{two pump photons}} \Big\}$$

$$= \frac{\mu_{10}^2 \mu_{01}}{4} G_{10}(t) \otimes \Big\{E_T(t)\Big(G_{11}(t) \otimes \{E_P^*(t)$$

$$[G_{10}(t) \otimes E_P(t)] - E_P(t)[G_{10}^*(t) \otimes E_P^*(t)]\}\Big)\Big\}. \tag{6.22}$$

The interference term [PTP] is commonly related to the observation of a *coherent artefact* in frequency domain spectra. It involves an interaction with pump $E_P^*(t)$, probe $E_T(t)$ and finally pump $E_P(t)$ again. As the interaction with the pump pulse must occur before and after the probe interaction, this limits the observation of the interference term to when the pump and probe pulses are overlapped in time... remember to work backwards!

$$\rho_{10}^{(3)}[\mathrm{PTP}](t) = \frac{\mu_{10}}{2} \underbrace{G_{10}(t) \otimes \Big\{E_P(t)}_{\text{pump photon}} \underbrace{\Big[\rho_{00}^{(2)TP}(t) - \rho_{11}^{(2)TP}(t)\Big]}_{\text{pump then probe photons}} \Big\}$$

$$= \frac{\mu_{10}^2 \mu_{01}}{4} G_{10}(t) \otimes \Big\{E_P(t)\Big(G_{11}(t)$$

$$\otimes\{E_T(t)[G_{10}^*(t) \otimes E_P^*(t)]\}\Big)\Big\}. \tag{6.23}$$

The final term corresponds to the two pump interactions occuring after the probe and perturbing the Free Induction Decay [PPT]. As observed with optical Bloch calculations in section 3 this perturbation will cause oscillations in the frequency domain spectra when the [PPT] term is Fourier transformed.

$$\rho_{10}^{(3)}[\mathrm{PPT}](t) = \frac{\mu_{10}^2 \mu_{01}}{4} \cdot \underbrace{G_{10}(t) \otimes \Big\{E_P(t)}_{\text{pump photon}}$$

$$\underbrace{\Big[G_{11}(t) \otimes \{E_P^*(t)}_{\text{pump photon}} \underbrace{[G_{10}(t) \otimes E_T(t)]\Big]}_{\text{probe photon}} \Big\}. \tag{6.24}$$

The total first and third order density matrix contributions are then added up and Fourier transformed to give the IR spectra in the frequency domain.

The approach so far has only been for a two level system and be summed up as follows. The Green functions always follow the order $G_{10} \leftarrow G_{11} \leftarrow G_{10}$, corresponding to a coherence, population transfer and then a final coherence. The part that changes for the three terms [TPP], [PTP] and [PPT] is whether the pump or probe field interacts with each Green function. Hence using a notation that neglects the convolutions and complex conjugates and focuses on the interactions between the electric fields and the Green functions, the three terms can be summarised as:

$$[\text{PPT}] = G_{10}(E_T) \leftarrow G_{11}(E_P) \leftarrow G_{10}(E_P)$$
$$[\text{PTP}] = G_{10}(E_P) \leftarrow G_{11}(E_T) \leftarrow G_{10}(E_P)$$
$$[\text{TPP}] = G_{10}(E_T) \leftarrow G_{11}(E_P) \leftarrow G_{10}(E_P).$$

It now becomes easier to see how the two level equations can be altered for a three level system. The Green function for the coherence between $v = 0$ and $v = 1$ is:

$$G_{01}(t) = \frac{i}{h}\Theta(t)exp(-i\omega_{01}t - \Gamma_{01}t), \tag{6.25}$$

hence the Green function for the coherence between $v = 1$ and $v = 2$ can be simply given as:

$$G_{21}(t) = \frac{i}{h}\Theta(t)exp(-i\omega_{21}t - \Gamma_{21}t). \tag{6.26}$$

It can now be seen that there are three more contributions to the total polarisation for a three level system. These will give the hotband in the pump-probe transients:

$$[\text{PPT}]^{21} = G_{21}(E_T) \leftarrow G_{11}(E_P) \leftarrow G_{10}(E_P)$$
$$[\text{PTP}]^{21} = G_{21}(E_P) \leftarrow G_{11}(E_T) \leftarrow G_{10}(E_P)$$
$$[\text{TPP}]^{21} = G_{21}(E_T) \leftarrow G_{11}(E_P) \leftarrow G_{10}(E_P).$$

The total three-level polarisation for an IR pump-probe experiment is then given by adding all six contributions to the third order density matrix to the first order density matrix contribution (from a single IR pulse SFG transition). Before this is Fourier transformed to give the spectra in the frequency domain, it is convoluted with the temporal width of the visible up-conversion pulse. The approach of consecutive convolution products proves to be considerably more efficient than trying to integrate the Bloch equations using numerical methods in the time domain. For a more robust explanation and further details, see [115].

Bibliography

[1] G. Attard and C. Barnes. *Surfaces*. Oxford Science Publications, 2003.

[2] Zewail A H. Femtochemistry: Past, Present and Future. *Pure Applied Chemistry*, 72(12):2219–2231, 2000.

[3] P. M. Paul, E. S. Toma, P. Breger, G. Mullot, F. Auge, P. Balcou, H. G. Muller, and P. Agostini. Observation of a train of attosecond pulses from high harmonic generation. *Science*, 292(5522):1689–1692, 2001.

[4] Library of Congress Prints and Photographs Division, http://hdl.loc.gov/loc.pnp/cph.3a45870.

[5] J. S. Baskin and A. H. Zewail. Freezing atoms in motion: Principles of femtochemistry and demonstration by laser stroboscopy. *Journal of Chemical Education*, 78(6):737–751, 2001.

[6] www.nobel.se/chemistry/laureates/1999/press.html.

[7] Zewail A H. Femtochemistry: Recent progress in studies of dynamics and control of reactions and their transition states. *Journal of Physical Chemistry*, 100(31):12701–12724, 1996.

[8] A. H. Zewail. 4D ultrafast electron diffraction, crystallography, and microscopy. *Annual Review of Physical Chemistry*, 57:65–103, 2006.

[9] T. Greber. Charge-transfer induced particle emission in gas surface reactions. *Surface Science Reports*, 28(1-2):3–64, 1997.

[10] J. D. White, J. Chen, D. Matsiev, D. J. Auerbach, and A. M. Wodtke. Conversion of large-amplitude vibration to electron excitation at a metal surface. *Nature*, 433(7025):503–505, 2005.

[11] Shen Y R. *The Principles of Nonlinear Optics*. John Wiley and Sons, New York, 1984.

[12] Robert W. Boyd. *Nonlinear Optics*. Academic Press, San Diego, 2nd edition, 2003.

[13] P. A. Franken, A. E. Hill, C. W. Peters, and G. Weinreich. Generation of Optical Harmonics. *Phys. Rev. Lett.*, 7(4):118–119, 1961.

[14] J. P. R. Symonds. *Femtosecond Sum-Frequency Spectroscopy of Metal-Adsorbate Systems*. PhD thesis, Cambridge University, 2003.

[15] Alex Lambert. *Resonantly enhanced sum frequency spectroscopy of adsorption on hydrophilic mica substrates.* PhD thesis, University of Cambridge, 2001.

[16] P. Galletto, H. Unterhalt, and G. Rupprechter. The molecular orientation of CO on Pd{111}: a polarization-dependent SFG study. *Chemical Physics Letters*, 367:785–790, 2003.

[17] Eugene Hecht. *Optics*. Addison Wesley, 4th edition, 2002.

[18] K. Stepan, J. Güdde, and U. Höfer. Time-Resolved Measurement of Surface Diffusion Induced by Femtosecond Laser Pulses. *Physical Review Letters*, 94(23):236103, 2005.

[19] J. Güdde and U. Höfer. Dynamics of femtosecond-laser-induced lateral motion of an adsorbate: O on vicinal Pt{111}. *Journal of Physics-Condensed Matter*, 18(30):S1409–S1424, 2006.

[20] R. Cotes. *Philosophical Transactions*, 29:32, 1714.

[21] A. Tadjeddine and A. Le Rille. Adsorption of cyanide on gold single crystal investigated by in situ visible-infrared difference frequency generation. *Electrochimica Acta*, 45(4-5):601–609, 1999.

[22] Roke S. *New light on hidden surfaces*. PhD thesis, Universiteit Leiden, 2004.

[23] L. T. Richter, T. P. Petralli-Mallow, and J. C. Stephenson. Vibrationally resolved sum-frequency generation with broad- bandwidth infrared pulses. *Optics Letters*, 23(20):1594–1596, 1998.

[24] K. C. Chou, S. Westerberg, Y. R. Shen, P. N. Ross, and G. A. Somorjai. Probing the charge-transfer state of CO on Pt{111} by two-dimensional infrared-visible sum frequency generation spectroscopy. *Physical Review B*, 69(15), 2004.

[25] E. H. G. Backus, A. Eichler, A. W. Kleyn, and M. Bonn. Real-time observation of molecular motion on a surface. *Science*, 310(5755):1790–1793, 2005.

[26] M. Bonn, C. Hess, S. Funk, J. H. Miners, B. N. J. Persson, M. Wolf, and G. Ertl. Femtosecond surface vibrational spectroscopy of CO adsorbed on Ru{001} during desorption. *Physical Review Letters*, 84(20):4653–4656, 2000.

[27] J. P. R. Symonds, H. Arnolds, and D. A. King. Femtosecond pump/probe spectroscopy of CO on Ru$\{10\bar{1}0\}$ from experimental and theoretical perspectives. *Journal of Physical Chemistry B*, 108(38):14311–14315, 2004.

[28] F. Fournier, W. Q. Zheng, S. Carrez, H. Dubost, and B. Bourguignon. Vibrational dynamics of adsorbed molecules under conditions of photodesorption: Pump-probe SFG spectra of CO/Pt{111}. *Journal of Chemical Physics*, 121(10):4839–4847, 2004.

[29] J. H. Hunt, P. Guyot-Sionnest, and Y. R. Shen. Observation of C-H Stretch Vibrations of Monolayers of Molecules: Optical Sum-Frequency Generation. *Chemical Physics Letters*, 133(3):189–192, 1987.

[30] A. Tadjeddine, A. Le Rille, O. Pluchery, F. Vidal, W. Q. Zheng, and A. Peremans. Sum and difference frequency generation at the electrochemical interface. *Physica Status Solidi A — Applied Research*, 175(1):89–107, 1999.

[31] H. Arnolds, C. Rehbein, G. Roberts, R. J. Levis, and D. A. King. Femtosecond near-infrared laser desorption of multilayer benzene on Pt{111}: A molecular Newton's cradle? *Journal of Physical Chemistry B*, 104(14):3375–3382, 2000.

[32] H. Arnolds, C. E. M. Rehbein, G. Roberts, R. J. Levis, and D. A. King. Femtosecond near-infrared laser desorption of multilayer benzene on Pt{111}: spatial origin of hyperthermal desorption. *Chemical Physics Letters*, 314(5-6):389–395, 1999.

[33] Arnolds H. Femtosecond laser-induced reactions with O_2 on Pt(111). *Surface Science*, 548:151–156, 2004.

[34] J. P. R. Symonds, H. Arnolds, V. L. Zhang, K. Fukutani, and D. A. King. Broadband femtosecond sum-frequency spectroscopy of CO on

Ru{10$\bar{1}$0} in the frequency and time domains. *Journal of Chemical Physics*, 120(15):7158–7164, 2004.

[35] V. L. Zhang, H. Arnolds, and D. A. King. Hot band excitation of CO/Ir{111} studied by broadband sum frequency generation. *Surface Science*, 587:102–109, 2005.

[36] V. L. Zhang, D. A. King, and H. Arnolds. The fractal growth of Au on Ir{111} and its influence on vibrational spectroscopy. to be submitted.

[37] C. Frischkorn and M. Wolf. Femtochemistry at Metal Surfaces: Nonadiabatic Reaction Dynamics. *Chemical Reviews*, 106(10):4207–4233, 2006.

[38] Y. Matsumoto and K. Watanabe. Coherent vibrations of adsorbates induced by femtosecond laser excitation. *Chemical Reviews*, 106(10):4234–4260, 2006.

[39] F. J. Kao, D. G. Busch, D. G. Dacosta, and W. Ho. Femtosecond Versus Nanosecond Surface Photochemistry - O_2+CO on Pt(111) at 80-K. *Physical Review Letters*, 70(26):4098–4101, 1993.

[40] D. N. Denzler, C. Frischkorn, C. Hess, M. Wolf, and G. Ertl. Electronic excitation and dynamic promotion of a surface reaction. *Physical Review Letters*, 91(22), 2003.

[41] H. Petek, M. J. Weida, H. Nagano, and S. Ogawa. Real-time observation of adsorbate atom motion above a metal surface. *Science*, 288(5470):1402–1404, 2000.

[42] K. Watanabe, N. Takagi, and Y. Matsumoto. Direct time-domain observation of ultrafast dephasing in adsorbate-substrate vibration under the in-

fluence of a hot electron bath: Cs adatoms on Pt(111). *Physical Review Letters*, 92(5), 2004.

[43] Y. Matsumoto, K. Watanabe, and N. Takagi. Excitation mechanism and ultrafast vibrational wavepacket dynamics of alkali-metal atoms on Pt{111}. *Surface Science*, 593(1-3):110–115, 2005.

[44] M. Bauer. Femtosecond ultraviolet photoelectron spectroscopy of ultra-fast surface processes. *Journal of Physics D-Applied Physics*, 38(16):R253–R267, 2005.

[45] T. A. Germer, J. C. Stephenson, E. J. Heilweil, and R. R. Cavanagh. Picosecond Measurement of Substrate-to-Adsorbate Energy- Transfer - the Frustrated Translation of CO/Pt{111}. *Journal of Chemical Physics*, 98(12):9986–9994, 1993.

[46] T. A. Germer, J. C. Stephenson, E. J. Heilweil, and R. R. Cavanagh. Hot-Carrier Excitation of Adlayers - Time-Resolved Measurement of Adsorbate-Lattice Coupling. *Physical Review Letters*, 71(20):3327–3330, 1993.

[47] J. P. Culver, M. Li, L. G. Jahn, R. M. Hochstrasser, and A. G. Yodh. Vibrational Response of Surface Adsorbates to Femtosecond Substrate Heating. *Chemical Physics Letters*, 214(5):431–437, 1993.

[48] J. D. Beckerle, R. R. Cavanagh, M. P. Casassa, E. J. Heilweil, and J. C. Stephenson. Subpicosecond Transient Infrared-Spectroscopy of Adsorbates - Vibrational Dynamics of CO/Pt{111}. *Journal of Chemical Physics*, 95(7):5403–5418, 1991.

[49] M. Morin, N. J. Levinos, and A. L. Harris. Vibrational-Energy Transfer of CO/Cu{100} - Nonadiabatic Vibration Electron Coupling. *Journal of Chemical Physics*, 96(5):3950–3956, 1992.

[50] A. L. Harris, L. Rothberg, L. H. Dubois, N. J. Levinos, and L. Dhar. Molecular Vibrational-Energy Relaxation at a Metal-Surface - Methyl Thiolate on Ag{111}. *Physical Review Letters*, 64(17):2086–2089, 1990.

[51] J. Kubota, A. Wada, S. Kano, and K. Domen. Time Resolved study of D_2O ice crytal on CO/Pt{111} by ultrashort NIR laser pumping: melting and recrystallization without desorption. *Chemical Physical letters*, 377:217–222, 2003.

[52] A. Bandara, S. S. Kano, K. Onda, S. Katano, J. Kubota, K. Domen, C. Hirose, and A. Wada. SFG spectroscopy of CO/Ni{111}: UV pumping and the transient hot band transition of adsorbed CO. *Bulletin of the Chemical Society of Japan*, 75(5):1125–1132, 2002.

[53] C. Hirose, A. Bandara, S. Katano, J. Kubota, A. Wada, and K. Domen. Sum-frequency generation study of reacting species at surfaces. *Applied Physics B-Lasers and Optics*, 68(3):559–565, 1999.

[54] S. Roke, J. Schins, M. Muller, and M. Bonn. Vibrational spectroscopic investigation of the phase diagram of a biomimetic lipid monolayer. *Physical Review Letters*, 90(12), 2003.

[55] M. Bonn, S. Roke, O. Berg, L. B. F. Juurlink, A. Stamouli, and M. Muller. A molecular view of cholesterol-induced condensation in a lipid monolayer. *Journal of Physical Chemistry B*, 108(50):19083–19085, 2004.

[56] X. Y. Chen, M. L. Clarke, J. Wang, and Z. Chen. Sum frequency generation vibrational spectroscopy studies on molecular conformation and orienta-

tion of biological molecules at interfaces. *International Journal of Modern Physics B*, 19(4):691–713, 2005.

[57] G.D. Reid and K. Wynne. *Encylopedia of Analytical Chemistry*, pages 13644–13670. John Wiley & Sons Ltd., 2000.

[58] R. E. Carley, E. Heesel, and H. H. Fielding. Femtosecond lasers in gas phase chemistry. *Chemical Society Reviews*, 34(11):949–969, 2005.

[59] C. M. Comrie and W. H. Weinberg. The Chemisorption of Carbon-Monoxide on the Iridium{111} Surface. *Journal of Chemical Physics*, 64(1):250–259, 1976.

[60] P. A. Zhdan, G. K. Boreskov, A. I. Baronin, W. F. Egelhoff, and W. H. Weinberg. XPS and UPS Investigation of Chemisorption of CO on Ir{111}. *Chemical Physics Letters*, 44(3):528–532, 1976.

[61] T. S. Marinova and K. L. Kostov. Interaction of Oxygen with a Clean Ir{111} Surface. *Surface Science*, 185(1-2):203–212, 1987.

[62] Rick Trebino. *Frequency Resolved Optical Gating: The Measurement of Ultrashort Laser Pulses*. Kluwer Academic Publishers, Norwell, MA, 2000.

[63] H. Arnolds, J. P. R. Symonds, V. L. Zhang, and D. A. King. *In situ* characterization of ultrafast laser pulses for sum frequency surface studies. *Review of Scientific Instruments*, 74(9):3943–3946, 2003.

[64] C. Y. Ruan, F. Vigliotti, V. A. Lobastov, S. Y. Chen, and A. H. Zewail. Ultrafast electron crystallography: Transient structures of molecules, surfaces, and phase transitions. *Proceedings of the National Academy of Sciences of the United States of America*, 101(5):1123–1128, 2004.

[65] S. Funk, M. Bonn, D. N. Denzler, C. Hess, M. Wolf, and G. Ertl. Desorption of CO from Ru{001} induced by near-infrared femtosecond laser pulses. *Journal of Chemical Physics*, 112(22):9888–9897, 2000.

[66] M. Brandbyge, P. Hedegard, T. F. Heinz, J. A. Misewich, and D. M. Newns. Electronically Driven Adsorbate Excitation Mechanism in Femtosecond-Pulse Laser-Desorption. *Physical Review B*, 52(8):6042–6056, 1995.

[67] E. H. G. Backus. *Driving and probing surfaces with light*. PhD thesis, Universiteit Leiden, 2005.

[68] M. Head-Gordon and J. C. Tully. Molecular-Orbital Calculations of the Lifetimes of the Vibrational-Modes of CO on Cu{(100}. *Physical Review B*, 46(3):1853–1856, 1992.

[69] Z. P. Liu, S. J. Jenkins, and D. A. King. Car exhaust catalysis from first principles: Selective NO reduction under excess O_2 conditions on Ir. *Journal of the American Chemical Society*, 126(34):10746–10756, 2004.

[70] Z. P. Liu, S. J. Jenkins, and D. A. King. Step-enhanced selectivity of NO reduction on platinum-group metals. *Journal of the American Chemical Society*, 125(48):14660–14661, 2003.

[71] W. A. Brown and D. A. King. NO chemisorption and reactions on metal surfaces: A new perspective. *Journal of Physical Chemistry B*, 104(47):2578–2595, 2000.

[72] J. Lauterbach, R. W. Boyle, M. Schick, W. J. Mitchell, B. Meng, and W. H. Weinberg. The adsorption of CO on Ir{111} investigated with FT-IRAS. *Surface Science*, 350(1-3):32–44, 1996.

[73] J.C.L. Cornish and N.R. Avery. Adsorption of N_2, O_2, N_2O and NO on Ir{111} by EELS and TPD. *Surface Science*, 235:209–216, 1990.

[74] J. E. Davis, S. G. Karseboom, P. D. Nolan, and C. B. Mullins. Kinetics and dynamics of the initial adsorption of nitric oxide on Ir{111}. *Journal of Chemical Physics*, 105(18):8362–8375, 1996.

[75] R.J. Hamers, P.L. Houston, and R.P. Merrill. Competition between direct-inelastic and trapping desorption channels in the scattering of NO (v = 0, J) from Ir{111}. *Journal of Chemical Physics*, 88:6548–6555, 1988.

[76] M. Morkel, H. Unterhalt, T. Kluner, G. Rupprechter, and H. J. Freund. Interpreting intensities in vibrational sum frequency generation (SFG) spectroscopy: CO adsorption on Pd surfaces. *Surface Science*, 586(1-3):146–156, 2005.

[77] B. N. J. Persson, F. M. Hoffmann, and R. Ryberg. Influence of Exciton Motion on the Shape of Optical-Absorption Lines - Applications to Vibrations at Surfaces. *Physical Review B*, 34(4):2266–2283, 1986.

[78] G. Witte. Low-energy dynamics of CO and NO chemisorbed on Rh{111}. *Journal of Chemical Physics*, 115(6):2757–2767, 2001.

[79] M. Bonn, D. N. Denzler, S. Funk, M. Wolf, S. S. Wellershoff, and J. Hohlfeld. Ultrafast electron dynamics at metal surfaces: Competition between electron-phonon coupling and hot-electron transport. *Physical Review B*, 61(2):1101–1105, 2000.

[80] S. Baldelli, N. Markovic, P. Ross, Y. R. Shen, and G. Somorjai. Sum frequency generation of CO on Pt{111} and polycrystalline platinum electrode surfaces: Evidence for SFG invisible surface CO. *Journal of Physical Chemistry B*, 103(42):8920–8925, 1999.

[81] W. Evans and J.I. Zink. Linear to Bent Geometry Changes in Gas- and Solution-Phase Photochemistry of Tricarbonylnitrosylcobalt. *Journal of the American Chemical Society*, 103:2635–2640, 1981.

[82] R.F. Fenske and R.L. DeKock. Intramolecular environmental effects on the bonding in transition metal-pentacyanonitrosyl complexes. *Inorganic Chemistry*, 11(3):437–444, 1972.

[83] J.H. Enemark and R.D. Feltham. Principles of structure, bonding, and reactivity for metal nitrosyl complexes. *Coordination Chemistry Reviews*, 13:339–406, 1974.

[84] I. Kinoshita, A. Misu, and T. Munakata. Electronic Excited-State of NO Adsorbed on Cu{111} - a 2-Photon Photoemission-Study. *Journal of Chemical Physics*, 102(7):2970–2976, 1995.

[85] P. D. Johnson and S. L. Hulbert. Inverse-Photoemission Studies of Adsorbed Diatomic-Molecules. *Physical Review B*, 35(18):9427–9436, 1987.

[86] V. Dose. Momentum-resolved inverse photoemission. *Surface Science Reports*, 5:337–378, 1985.

[87] DFT calculations performed by Dr Zhipan Liu. Shanghai Key Laboratory of Molecular Catalysis and Innovative Materials, Department of Chemistry, Fudan University, Shanghai, 200433, People's Republic of China.

[88] J. Noffke and L. Fritsche. Band-Structure Calculation and Photoemission Analysis of Iridium. *Journal of Physics F-Metal Physics*, 12(5):921–933, 1982.

[89] S. Roke, A. W. Kleyn, and M. Bonn. Ultrafast surface dynamics studied with femtosecond sum frequency generation. *Journal of Physical Chemistry A*, 105(10):1683–1686, 2001.

[90] M. Lisowski, P. A. Loukakos, U. Bovensiepen, J. Stahler, C. Gahl, and M. Wolf. Ultra-fast dynamics of electron thermalization, cooling and transport effects in Ru{001}. *Applied Physics a-Materials Science & Processing*, 78(2):165–176, 2004.

[91] M. Gajdos, J. Hafner, and A. Eichler. *Ab initio* density-functional study of NO on close-packed transition and noble metal surfaces: I. Molecular adsorption. *Journal of Physics-Condensed Matter*, 18(1):13–40, 2006.

[92] T. Yamanaka, A. Hellman, S. W. Gao, and W. Ho. State-resolved femtosecond two-pulse correlation measurements of NO photodesorption from Pt{111}. *Surface Science*, 514(1-3):404–408, 2002.

[93] P. Saalfrank, G. Boendgen, K. Finger, and L. Pesce. Photodesorption of NO from a metal surface: quantum dynamical implications of a two-mode model. *Chemical Physics*, 251(1-3):51–69, 2000.

[94] J. S. Villarrubia and W. Ho. Nitric-Oxide Adsorption, Decomposition, and Desorption on Rh{100}. *Journal of Chemical Physics*, 87(1):750–764, 1987.

[95] A. Sandell, A. Nilsson, and N. Martensson. Lying Down NO on Ni{100}. *Surface Science*, 241(1-2):L1–L5, 1991.

[96] N. D. Shinn and T. E. Madey. CO Chemisorption on Cr{110} - Evidence for a Precursor to Dissociation. *Journal of Chemical Physics*, 83(11):5928–5944, 1985.

[97] D. W. Moon, S. Cameron, F. Zaera, W. Eberhardt, R. Carr, S. L. Bernasek, J. L. Gland, and D. J. Dwyer. A Tilted Precursor for CO Dissociation on the Fe{100} Surface. *Surface Science*, 180(1):L123–L128, 1987.

[98] M. Gajdos, J. Hafner, and A. Eichler. *Ab initio* density-functional study of NO adsorption on close-packed transition and noble metal surfaces: II. Dissociative adsorption. *Journal of Physics-Condensed Matter*, 18(1):41–54, 2005.

[99] H. Ueba. Vibrational relaxation and pump-probe spectroscopies of adsorbates on solid surfaces. *Progress in Surface Science*, 55(2):115–179, 1997.

[100] P. Guyot-Sionnest. Coherent Processes at Surfaces - Free-Induction Decay and Photon-Echo of the Si-H Stretching Vibration for H/Si{111}. *Physical Review Letters*, 66(11):1489–1492, 1991.

[101] J. C. Owrutsky, J. P. Culver, M. Li, Y. R. Kim, M. J. Sarisky, M. S. Yeganeh, A. G. Yodh, and R. M. Hochstrasser. Femtosecond Coherent Transient Infrared-Spectroscopy of CO on Cu{111}. *Journal of Chemical Physics*, 97(6):4421–4427, 1992.

[102] S. Roke, A. W. Kleyn, and M. Bonn. Femtosecond sum frequency generation at the metal-liquid interface. *Surface Science*, 593(1-3):79–88, 2005.

[103] L. Allen and J.H. Eberly. *Optical Resonance and Two-Level Atoms*. Dover, New York, 1987.

[104] E.L. Hahn. Spin Echoes. *Physical Review*, 80:580–594, 1950.

[105] N. A. Kurnit, I. D. Abella, and S. R. Hartman. Observation of a Photon Echo. *Physical Review Letters*, 13(19):567–569, 1967.

[106] X. D. Zhu and Y. R. Shen. Surface Photon Echoes in the Infrared Range. *Applied Physics B*, 50:535–539, 1990.

[107] C.A. Walsh, M. Berg, L.R. Narashimham, and M. D. Fayer. Probing Intermolecular Interactions with Picosecond Photon Echo Experiments. *Accounts of Chemical Research*, 20:120, 1987.

[108] A. Crossley and D.A. King. Infrared spectra for CO isotopes chemisorbed on Pt{111}: Evidence for strong adsorbate coupling interactions. *Surface Science*, 68:528–538, 1977.

[109] P. Guyot-Sionnest, P. Dumas, and Y. J. Chabal. Lifetime of an Adsorbate-Substrate Vibration Measured by Sum Frequency Generation-H on Si{111}. *Journal of Electron Spectroscopy and Related Phenomena*, 54:27–38, 1990.

[110] A. L. Harris, L. Rothberg, L. Dhar, N. J. Levinos, and L. H. Dubois. Vibrational-Energy Relaxation of a Polyatomic Adsorbate on a Metal-Surface - Methyl Thiolate (CH_3S) on Ag{111}. *Journal of Chemical Physics*, 94(4):2438–2448, 1991.

[111] H. Pfnür, D. Menzel, F.M. Hoffmann, A. Ortega, and A. M. Bradshaw. High Resolution Vibrational Spectroscopy of CO on Ru(001): The Importance of Lateral Interactions. *Surface Science*, 93:431–452, 1980.

[112] P. Atkins and J. de Paula. *Atkins' Physical Chemistry*. Oxford University Press, seventh edition, 2002.

[113] A. L. Harris, N. J. Levinos, L. Rothberg, L. H. Dubois, L. Dhar, S. F. Shane, and M. Morin. Vibrational-Energy Transfer to Metal-Surfaces Probed by Sum Frequency Generation - CO/Cu{100} and CH_3S/Ag{111}. *Journal of Electron Spectroscopy and Related Phenomena*, 54:5–16, 1990.

[114] A.L. Harris and L. Rothberg. Surface vibrational energy relaxation by sum frequency generation: Five-wave mixing and coherent transients. *Journal of Chemical Physics*, 94(4):2449, 1991.

[115] M. Joffre. *Femtosecond Laser Pulses-Principles and Experiments*, chapter 9. Coherent Effects in Femtosecond Spectroscopy: A Simple Picture using the Bloch Equations, pages 283–308. Springer, 2003.

[116] W. G. Roeterdink, O. Berg, and M. Bonn. Frequency- and time-domain femtosecond vibrational sum frequency generation from CO adsorbed on Pt{111}. *Journal of Chemical Physics*, 121(20):10174–10180, 2004.

[117] B. N. J. Persson and R. Ryberg. Dipole-coupling-induced line narrowing in adsorbate vibrational spectroscopy. *Chemical Physics Letters*, 174(5):443–448, 1990.

[118] P. Jakob and B. N. J. Persson. Dephasing of localized and delocalized vibrational modes: CO adsorbed on Ru{001}. *Physical Review B*, 56(16):10644–10650, 1997.

[119] P. Jakob and B. N. J. Persson. Infrared spectroscopy of overtones and combination bands. *Journal of Chemical Physics*, 109(19):8641–8651, 1998.

[120] J. D. Beckerle. *Laser spectroscopy and photochemistry on metal surfaces Part 1*, chapter 12, pages 459–497. World Scientific, 1995.

[121] T. Kato, M. Hayashi, A. A. Villaeys, and S. H. Lin. Theoretical study on surface vibrational infrared-visible sum-frequency generation spectroscopy applied to adsorbed molecules. *Physical Review A*, 56(1):980–993, 1997.

[122] A. A. Villaeys and F. P. Lohner. Time-dependent description of dephasing processes in adsorbate bonding by pumped sum-frequency generation spectroscopy. *Physical Review A*, 6301(1), 2001.

[123] A. A. Villaeys, Y. J. Dappe, M. Zouari, and H. Bouchriha. Time-delayed infrared-visible probe pulses in five-wave mixing spectroscopy. *Chemical Physics Letters*, 358(1-2):130–138, 2002.

[124] A. A. Villaeys and F. P. Lohner. Influence of the pure vibrational dephasing processes on the dip structure in pumped sum-frequency generation spectroscopy. *Physical Review A*, 59(5):3926–3940, 1999.

[125] S. Beyvers, Y. Ohtsuki, and P. Saalfrank. Optimal control in a dissipative system: Vibrational excitation of CO/Cu{100} by IR pulses. *Journal of Chemical Physics*, 124(23):234706, 2006.

[126] M. E. Schmidt and P. Guyot-Sionnest. Electrochemical tuning of the lifetime of the CO stretching vibration for CO/Pt{111}. *Journal of Chemical Physics*, 104(6):2438–2445, 1996.

[127] Windhorn L, Yeston J S, Witte T, Fuss W, Motzkus M, Proch D, Kompa K L, and Moore C B. Getting ahead of IVR: A demonstration of mid-infrared induced molecular dissociation on a sub-statistical time scale. *Journal of Chemical Physics*, 119(2):641–645, 2003.

[128] E. W. Triche, J. F. Gent, T. R. Holford, K. Belanger, M. B. Bracken, W. S. Beckett, L. Naeher, J. E. McSharry, and B. P. Leaderer. Low-level ozone exposure and respiratory symptoms in infants. *Environmental Health Perspectives*, 114(6):911–916, 2006.

[129] M. Ogura, A. Kawamura, M. Matsukata, and E. Kikuchi. Catalytic activity of Ir for NO-CO reaction in the presence of SO_2 and excess oxygen. *Chemistry Letters*, (2):146–147, 2000.

[130] A. Q. Wang, L. Ma, Y. Cong, T. Zhang, and D. B. Liang. Unique properties of Ir/ZSM-5 catalyst for NO reduction with CO in the presence of excess oxygen. *Applied Catalysis B-Environmental*, 40(4):319–329, 2003.

[131] M. Haneda, H. Kudo, Y. Nagao, T. Fujitani, and H. Hamada. Enhanced activity of Ba-doped Ir/SiO_2 catalyst for NO reduction with CO in the presence of O_2 and SO_2. *Catalysis Communications*, 7(7):423–426, 2006.

[132] T. Fujitani, I. Nakamura, Y. Kobayashi, A. Takahashi, M. Haneda, and H. Hamada. Adsorption and reactions of NO on clean and CO-precovered Ir{111}. *Journal of Physical Chemistry B*, 109(37):17603–17607, 2005.

[133] S. Katano, A. Bandara, J. Kubota, K. Onda, A. Wada, K. Domen, and C. Hirose. Screening of SFG signals from bridged CO on Ni{111} by the coexistence of linear CO. *Surface Science*, 428:337–342, 1999.

[134] J. H. Miners, P. Gardner, A. M. Bradshaw, and D. P. Woodruff. A CO_2 surface molecular precursor during CO oxidation over Pt{100}. *Journal of Physical Chemistry B*, 108(38):14270–14275, 2004.

[135] C. J. Zhang, P. Hu, and A. Alavi. Insight into electron-mediated reaction mechanisms: Catalytic CO oxidation on a ruthenium surface. *Journal of Chemical Physics*, 114(18):8113–8118, 2001.

[136] S.I. Anisimov, B.L. Kapeliovich, and T.L. Perel'man. Electron emission from surface of metals induced by ultrafasr laser pulses. *Soviet Physics JETP*, 39:375, 1974.

[137] NAG Fortran library routine D03PF Mark 18.

[138] S. D. Brorson, A. Kazeroonian, J. S. Moodera, D. W. Face, T. K. Cheng, E. P. Ippen, M. S. Dresselhaus, and G. Dresselhaus. Femtosecond Room-Temperature Measurement of the Electron-Phonon Coupling Constant-Lambda in Metallic Superconductors. *Physical Review Letters*, 64(18):2172–2175, 1990.

[139] C. Kittel. *Solid State Physics*. Wiley, 1995.

[140] J. K. Baria and A. R. Jani. Comprehensive study of lattice mechanical properties of some FCC transition metals. *Physica B-Condensed Matter*, 328(3-4):317–335, 2003.

[141] P. B. Allen. Empirical Electron-Phonon-Gamma Values from Resistivity of Cubic Metallic Elements. *Physical Review B*, 36(5):2920–2923, 1987.